HAL
open science

Kondo physics in side coupled quantum dots

Yannick David Baines

To cite this version:

Yannick David Baines. Kondo physics in side coupled quantum dots. Condensed Matter [cond-mat]. Université Joseph-Fourier - Grenoble I, 2010. English. NNT : . tel-00558577

HAL Id: tel-00558577

https://theses.hal.science/tel-00558577

Submitted on 22 Jan 2011

HAL is a multi-disciplinary open access archive for the deposit and dissemination of scientific research documents, whether they are published or not. The documents may come from teaching and research institutions in France or abroad, or from public or private research centers.

L'archive ouverte pluridisciplinaire **HAL**, est destinée au dépôt et à la diffusion de documents scientifiques de niveau recherche, publiés ou non, émanant des établissements d'enseignement et de recherche français ou étrangers, des laboratoires publics ou privés.

UNIVERSITÉ DE GRENOBLE

THESIS

To obtain the grade of

DOCTEUR DE L'UNIVERSITE DE GRENOBLE
Spécialité **Physique**

BAINES David Yann

13 Décembre 2010

KONDO PHYSICS IN SIDE COUPLED QUANTUM DOTS

Thesis supervised by **SAMINADAYAR Laurent** and **MEUNIER Tristan**

JURY

- ULLMO Denis	**- DR 2, LPTMS**	**- Referee**
- KONTOS Takis	**- CR1, LPA**	**- Referee**
- FEINBERG Denis	**- DR1, IN**	**- Examiner**
- MAILLY Dominique	**- DR1, LPN**	**- Examiner**
- MEUNIER Tristan	**- CR2, IN**	**- Examiner**
- SAMINADAYAR Laurent	**- PR2, IN**	**- Examiner**

Thesis prepared in the **Institut Néel** in the **Ecole Doctorale de Physique Grenoble**

Contents

Introduction **1**

1 Two dimensional electron gases and quantum dots **1**
1.1 Gallium arsenide heterostructures 1
1.1.1 Composition and growth 2
1.1.2 Conduction band structure 3
1.2 Nanofabrication methods 5
1.2.1 Electronic lithography 5
1.2.2 Ohmic contacts diffusion 6
1.2.3 Mesa etching 8
1.2.4 Lateral gates deposition 9
1.3 Quantum dot geometries 11

2 Elements of theory **15**
2.1 Landauer-Büttiker formalism 15
2.2 Quantum point contacts 16
2.3 Transport through a quantum dot 18
2.3.1 Quantization of the energy levels 18
2.3.2 Electron-electron interactions 19
2.3.3 The electrochemical potential 21
2.3.4 Coulomb blockade 22
2.3.5 Stability diagrams 26
2.4 Transport through double quantum dots 31
2.4.1 Semi classical model 31
2.4.2 Stability diagrams 33
2.4.3 Tunnel coupling 40
2.5 Cotunnelling 43
2.6 Kondo effect 45
2.6.1 Anderson Hamiltonian 46
2.6.2 Link between the Anderson and the Kondo Hamiltonians 47
2.6.3 Notes on perturbation theory 49
2.6.4 Kondo temperature 51
2.6.5 Kondo resonance 53

3 Experimental setup **59**
3.1 Dilution refrigerator 59
3.1.1 Principle 59
3.1.2 Coaxial lines and filtering 61
3.2 Electronics 64
3.2.1 Digital-to-analog converters 64
3.2.2 Current-to-voltage converter 67
3.2.3 Acquisition chain 71

4 Experiments and interpretations **73**
4.1 Interplay between inter-dot tunnelling and temperature . . . 76
4.1.1 Low temperature and high temperature limits 76
4.1.2 inter-dot tunnel coupling : limiting cases 80
4.1.3 Effect of cross talk 85
4.1.4 Multi level system approach 87
4.1.5 Numerical simulations 89
4.1.6 Cross talk between the plunger gates 93
4.1.7 Effect of hybridisation with the leads 94
4.2 Kondo effect on an orbital degeneracy point 94
4.2.1 Low temperature stability diagram 94
4.2.2 Kondo signatures 97
4.2.3 Two level system approach 104
4.2.4 Boosting the Kondo temperature 108
4.2.5 Evolution of the Kondo resonance 110
4.2.6 Profile of the orbital degeneracy ridge 117
4.2.7 Addition of the second electron 118
4.2.8 Interplay between Kondo and exchange 122

Conclusion and perspectives **129**

A Multi level interacting quantum dots **131**

B Singlet binding energy **133**

Bibliography **134**

Introduction

Thanks to the discovery of the transistor effect and the invention of the first point contact transistor during the early 1950s by John Bardeen, Walter House Brattain and William Shockley at Bell Laboratories, the field of microelectronic devices was born [1] [2]. Based on a semiconducting crystal of germanium this transistor enabled the fabrication of scalable and low power consuming switches and amplifiers. About ten years later, still at Bell Laboratories, the Metal Oxide Semiconductor Field Effect Transistor (MOSFET) was invented by John Atalla and Dawon Kahng [3] [4]. This particular family of FETs, nowadays commonly based on silicon, has become the most popular transistor mainly because of its low cost and excellent scalability. Computers, cellular phones, and other digital appliances, now inextricable parts of the structure of modern societies, were made possible by integrating large numbers of these small transistors onto single electronic chips.
The race for miniaturisation is still an actual challenge. To give an order of magnitude, today's microprocessors hold billions of transistor with a typical size of 50 nm that equip our everyday personal computer and new generations even smaller are becoming available on the market. Nonetheless the atomic scale, typically below the nanometer, fixes the fundamental limitation. Interestingly on this scale, objects obey the laws of quantum mechanics which raise even larger challenges for tomorrow's nanolectronics.
Nanoelectronics is at the research stage today and appears to be a very rich and dynamical topic from the point of view of future applications as mentioned, but also of fundamental physics. A great illustration of these two aspects of nanoelectronics is the quantum dot. In simple terms, a quantum dot is a small region in space where electrons are confined, as in an atom. Various materials are now used to build quantum dots, such as semiconductors, carbon nanotubes or molecules. The important enthusiasm quantum dots encounter comes from their potential to implement quantum bits [5] opening the road of quantum computing, and from the opportunities they offer to study in situ important problems of condensed matter physics.
Some of the most intriguing problems in solid state physics arise when the motion of one electron dramatically affects the motion of surrounding electrons. Such highly correlated electron systems have been studied mainly in materials with complex transition metal chemistry. A hallmark of these

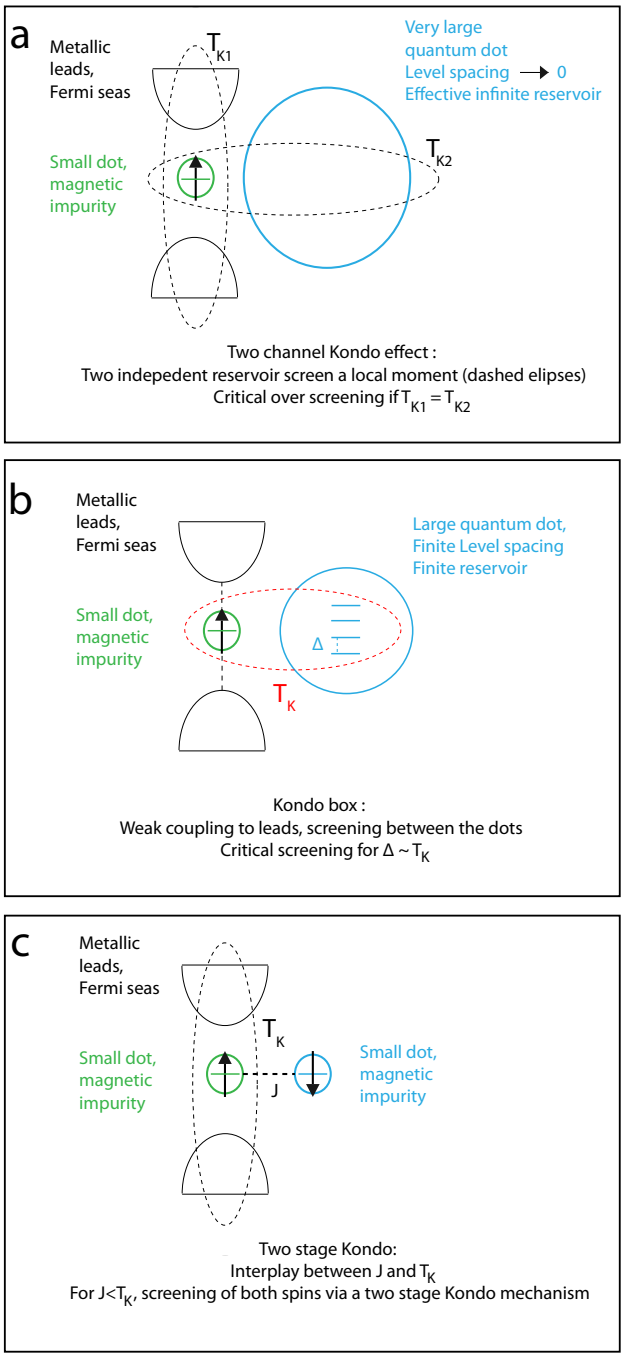

Figure 1: a) Two channel Kondo problem. b) Kondo box problem. c) Two stage Kondo problem

fundamental problems is know as the Kondo effect, a subtle many electron effect in which conduction electrons in the vicinity of a spin impurity screen the spin to form a collective entangled ground state at low temperatures. Originally observed in metals containing magnetic impurities it was proved theoretically and experimentally that a quantum dot can undergo the Kondo effect [6]. The connection between Kondo physics and a quantum dot is made when an odd number of electrons confined within the dot act as a single spin coupled to electron reservoirs. In the frame of the Kondo effect quantum dots appears to be very powerful tools enabling the study of a single magnetic impurity in the Kondo regime. It is worth noticing that from the theoretical point of view, treating the Kondo effect is a hard task due the non perturbative nature of the coupling of the system (spin) to the environment (reservoirs). Experimentally, even though the physics of quantum dots in the weak coupling regime has been extensively studied, the strong coupling limit still suffers from a lack of investigations and knowledge as we will see from our experiments.
The integration of multiple quantum dots, such as double quantum dots, offers the possibility to study richer physics such as the charge Kondo effect where the degree of freedom being quenched at low temperature is no longer a spin but a charge [7], the two channel Kondo effect where a single magnetic impurity is screened by two independent electron reservoirs (leads+large quantum) leading to a over screening regime [8] (Fig 1, a) or the two stage Kondo effect where the Kondo mechanism enters in competition with the exchange interaction in order to screen two local moments tunnel coupled, leading to two consecutive Kondo processes quenching both spins at low temperature [9] (Fig 1, c).

This thesis project sits at the interface of the two channel Kondo effect and the two stage Kondo effect. A connection between both effects can be made through the scale of the second quantum dot that acts as a reservoir in the first case or a local moment in the second case. For an intermediate size, a finite size reservoir interacts with the magnetic impurity, a problem known in literature as the Kondo box problem [10] [11]. The central point of this problem is the discretisation of the energy levels of the larger dot on an energy scale being the Kondo temperature. When the ratio $T_K/\Delta_{finite\ \ reservoir}$ gets of the order of one, a critical inter dot Kondo regime is expected with a loss of universality. Note that universality is one of the strong signatures of the standard Kondo effect (Fig 1, b).

The outline of this thesis is the following:

- We will first present the base material from which our double quantum dots are made, that is to say a semiconductor heterostructure of aluminium gallium arsenide. The different nanofabrication steps used

to engineer these heterostructures and build lateral quantum dots will be introduced.

- In a second part we will draw up a non exhaustive list of theoretical elements required to understand transport through quantum dots, and in particular in the Kondo regime.

- Then a short part will be devoted to the cryogenic techniques used to perform transport measurements at sub-Kelvin temperatures. The necessity of low noise electronics encouraged us to design and interface the major part of the electronic instruments. Their specification and confirmations via bench measurements will be exposed.

- Finally, the experimental data and interpretations will be presented.
  In a first part we will focus on the importance of hybridisation between two quantum dots strongly coupled. An particular interest will be given to the strength of the inter dot tunnel coupling compared to the intrinsic energy scales of the dots. Beyond a certain threshold, above which the tunnelling matrix element becomes larger than the level spacing of one dot, we will show the importance of considering the hybridisation of multiple energy levels. As a result a complex molecular addition spectrum will characterize the double dot system which will lead to unusual transport properties at low temperature where irregular filling of each dot will be displayed in the stability diagram. The question of the evolution of the system with temperature will be addressed. Interestingly, for temperatures above the tunnelling energy scale, regular transport properties will be recovered. A multi-level interacting quantum dots model will enable to capture the low and high temperature limits via numerical simulations that will be confronted to the experimental data.
  In a second part, we will expose a study of a pronounced Kondo effect occurring when both dots are degenerated in energy. In the framework of the molecular eigenstates formed between the dots, we will show that a spin Kondo effect boosted near the degeneracy point of the dots can explain our observations. The first part of our analysis will be done in the framework of a two level system. From our observation, the question of the interplay between the inter dot exchange interaction and the Kondo temperature will naturally arise. Evidence of an important inter dot tunnel coupling will push us to consider the nature of the exchange interaction in a multi-level system. Interestingly we will show that the hybridisation of more than two energy levels tends to reduce the effective exchange interaction, which in our case enables the system to undergo the Kondo effect.

Chapter 1

Two dimensional electron gases and quantum dots

The availability of two dimensional electron gases (2DEG) to fundamental research comes from the great success of modern electronics and the use of semiconducting materials since the last fifty years.
The base material used during this project is a semiconducting heterostructure made of gallium arsenide (AsGa) and aluminium gallium arsenide (AlGaAs) with high mobility and low electron density. It has the particularity to contain an embedded 2DEG and we usually refer to it as a High Electron Mobility Transistor (HEMT) or Metal Semiconductor Field Effect Transistor (MESFET).
As we will see in the following, thanks to the microfabrication methods nowadays widely used in the microelectronics industry we will be able to contact and shape these HEMT to reach specific geometries. These techniques will also enable us to define fine metallic gates on the surface of the structures with which quantum dots will be electrostatically created and controlled. Lateral quantum dots are very powerful tools used in the field of mesoscopic physics to study spin based quantum information and correlated electron systems. Thanks to their high tunability they happen to be very well suited to study Kondo physics.
We will first detail the structure of AlGaAs/GaAs wafers and understand how a two dimensional gas forms in them by analysing their band structure. Then we will expose the methods used to nanofabricate lateral quantum dots and present the specific designs chosen to study Kondo physics.

1.1 Gallium arsenide heterostructures

In the frame of this Phd the GaAs/AlGaAs growth was made in *Lehrstuhlfür Angewandte Festkörperphysik* in Bochum (Germany) in collaboration with D. Reuter and Andreas D. Wieck [12]. Since we did not participate to

the elaboration of the heterostructures we will only address briefly their composition and growth process in the following.

1.1.1 Composition and growth

The gallium arsenide heterostructure is a semiconductor made of different semiconducting layers of gallium arsenide and aluminium gallium arsenide stacked on top of each other. The specific sequence of stacking, leads to a particular band structure which gives rise to the formation of a 2DEG in the structure as we will see later. Figure 1.1 shows the succession of these different layers.

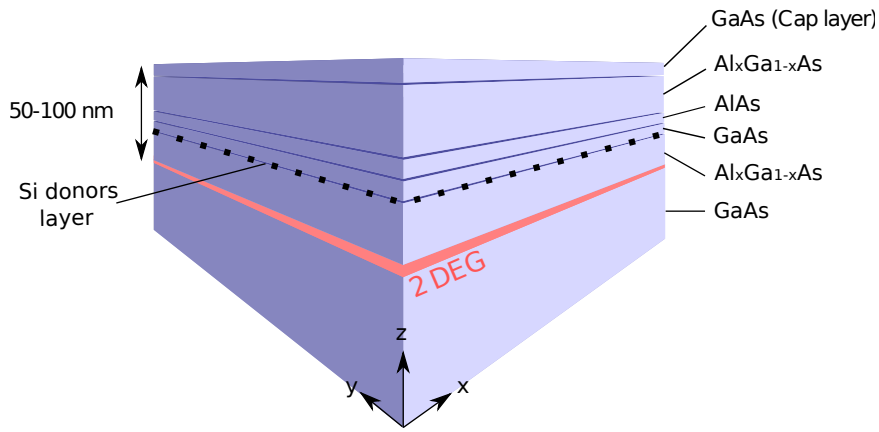

Figure 1.1: Gallium arsenide heterostructure containing a two dimensional electron gas at the GaAs and AlGaAs interface. The electrons present at that interface come from the doping layer, in our case silicon donors. For a very thin doping layer we talk about *δ-doping*. Z axis corresponds to the growth direction

The different layers of GaAs and AlGaAs are realized using a Molecular Beam Epitaxy (MBE) method where one or several molecular beams are sent towards a chosen substrate under a controlled atmosphere with a residual pressure less than 10^{-8}Pa. This method enables to grow nanostuctured samples of several cm^2 with a speed of approximatively one atomic layer per second. MBE produces very high crystal purity (less than 10^{14} impurities per cm^3) and offers the opportunity to implant dopants during the growth process.
In the case of the GaAs heterostructure, the base substrate is a GaAs wafer (100). A thick layer of GaAs (>100μm) is grown on top of it. Growth continues with a AlGaAs alloy with an almost perfect lattice-matched to the GaAs crystal. Atomically sharp interfaces between these materials can be realized without introducing structural defects. A lattice plan remote from the GaAs/AlGaAs interface is doped with sillicon atoms incorporated

mainly on the gallium lattice sites (n-type δ-doping Fig. 1.1). The layer sequence is completed by encapsulating the doping plane with AlGaAs and protecting the surface from oxidation with a thin layer of GaAs.

1.1.2 Conduction band structure

GaAs presents an energy bandgap ΔE_{g1} equal to 1.42 eV. By substituting a fraction of gallium atoms by aluminium atoms, that is to say by changing the chemical composition of GaAs to $Al_xGa_{1-x}As$ (AlGaAs) it is possible to increase this energy bandgap. Usually a fraction x=0.3 is substituted leading to an increase of 0.39eV of the energy bandgap. Therefore there is a very sharp energy bandgap difference at the interface of these two chemical compounds is the GaAs heterostructure.
When Si-dopants are implanted in the AlGaAs donor region (n type AlGaAs layer), at the GaAs/AlGaAs heterojunction the conduction band profile exhibits a triangular well (Fig. 1.2) giving rise to single occupied quantum states in the confining direction. Free electrons of the n-type AlGaAs layer then accumulate at the heterojunction, in the quantum well. Because of the confining potential these electrons are only allowed to move in the plane of the interface where they form the so called two dimensional electron gas. The 2DEG is usually separated about 20 nm from the AlGaAs donor region

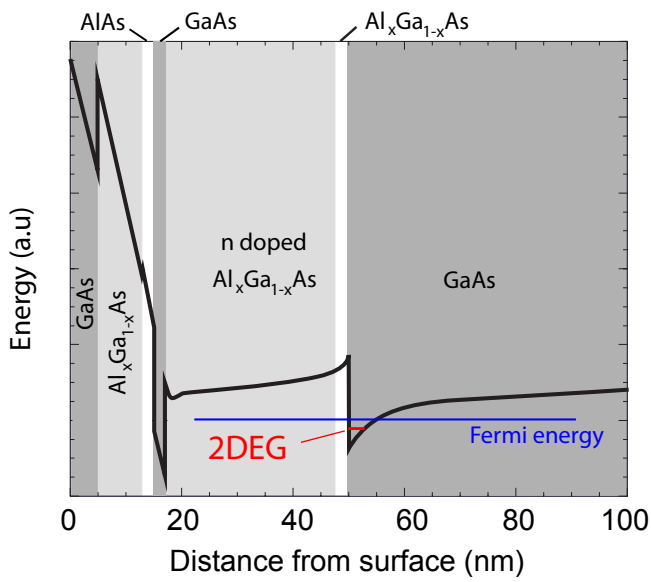

Figure 1.2: Conduction band profile in the GaAs/AlGaAs heterostructure showing the 2DEG formed in a triangular well potential formed at the GaAs/AlGaAs interface.

by an undoped spacer layer. This separation allows for extremely high mo-

bility of the electrons in the 2DEG, because scattering with the Si donors is strongly reduced. At liquid helium temperature, i.e 4.2 K, the typical electron mobility and electron density are 10^5-10^6 $cm^2.V^{-1}.s^{-1}$ and 10^{15} m^{-2} respectively. The relatively low electron density results in a large Fermi wavelength, $\sim$ 40 nm, and a large screening length, which allows to locally deplete the 2DEG with an electric field.
Electric fields can be created by applying voltages to metal gate electrodes fabricated on top of the heterostructure as in a MOSFET. The Schottky barrier formed at the metal-semiconductor junction ensures that no charges leak into the heterostructure. The coupling between the gate and the electron gas is then purely capacitive. To first order this will be true at low temperature though as we will see in the experimental data some tunnelling events from the metal gate to the 2DEG exist and create undesirable charge offsets. Note that experimental techniques have been developed to reduce these events [13] [14].
In the case of quantum dots, in order to confine electrons of the 2DEG in small closed regions, one needs to apply negative voltages on the metal gates to locally deplete the gas. Figure 1.3 shows the typical profile of the electrical field penetrating the structure and shows how a conducting channel of electrons can be created for a certain set of metallic gates. It is now straightforward to understand how an isolated island of electrons can be electrostatically defined and controlled with a specific set of electrodes. We

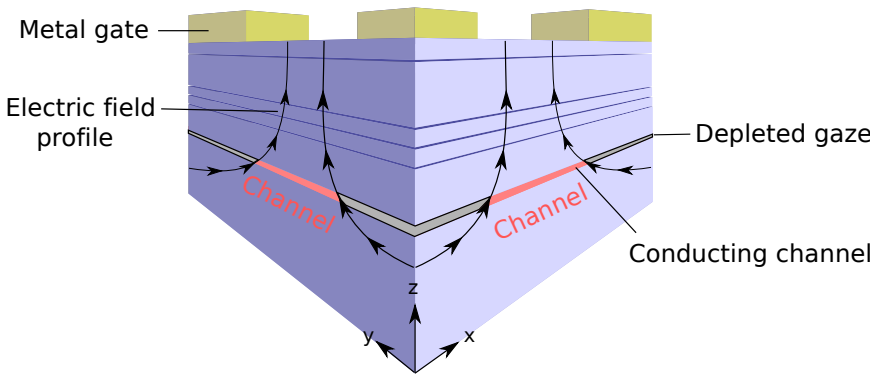

Figure 1.3: By applying voltages on the metal electrodes on the surface of the heterostructure, the density of electrons in the gas can be changed. For negative voltages the 2DEG can be locally depleted enabling the user to confine electrons in one or zero dimension for a given geometry of the metallic gates. In other words, quantum dots can be formed in the electron gas using a specific set of gates.

will show in the next section how it is possible by using microlithographic methods to engineer the heterostructure. Three main goals will thereby be achieved : first we will contact the gas with ohmic pads, then we will etch

the gas to shape it at a microscopic scale and finally metal electrodes will be patterned on top of the structure following a specific geometry.

1.2 Nanofabrication methods

In order to fabricate quantum dots that we will probe via transport measurements we need to engineer the AlGaAs heterostructure by means of nanofabrication methods. We will expose the electronic beam lithography technique that enables to write fine patterns in electro-sensitive resists previously pasted on the surface of the wafer. The written patterns will serve as masks to deposit metals on top of the heterostructure. Different metals will be used in order to create ohmic contacts connecting electrically the 2DEG, metal masks to etch and shape the wafer and metallic gates used to deplete the electron gas (Fig. 1.3) and confine electrons thereby forming quantum dots.
All the different nanofabrication steps and methods exposed in the next sections are performed in the *Laboratoire de Photonique et Nanostructures* (LPN/CNRS) in Marcoussis. The major part of the samples nanofabrication was done by Dominique Mailly [15].

1.2.1 Electronic lithography

Borrowed from the modern electronics industry, the electron beam lithography is a powerful technique to create extremely fine patterns. Derived from scanning electron microscopes, the technique mainly consists of scanning a beam of electrons on a surface pasted with a resist which will be sensitive to the energy deposited by the beam. We will not go into the detail of how such a beam is realized, for more informations we refer the reader to [16]. With today's electron optics, electron beam widths can routinely go down to a few nanometers. However, the feature resolution limit is determined not by the beam size but by the forward scattering (effective beam broadening) in the resist. In practice this technique will allow us to make high resolution patterns ($\sim$20 nm) and work with a wide variety of materials and patterns. To start, the substrate is covered with an e-beam resist. In the case of our samples the surface of the heterostructure is spin coated with a widely used positive resist which is polymethyl methacrylate (PMMA). The resist is baked at 200°C for 15 to 30 minutes usually, before lithographic exposure.
An e-beam writer then scans the resist following a specific pattern. The electron irradiation breaks polymer backbone bonds at the exposed areas, leaving fragments of lower molecular weight. The beam energy and the irradiation time are crucial parameters to be able to create good quality patterns. Bad control over these parameters can lead to weak exposure of the resist resulting in a low contrasted pattern or can lead to over exposure

resulting in an effective broadening of the beam due to strong forward scattering as mentioned above.
A solvent developer, such as MIBK:IPA, is used to wash away the lower molecular weight fragments, thus forming a positive tone pattern. This positive tone pattern is then fully recovered with metal by evaporation.
The metal evaporation involves two basic processes : a hot metallic source evaporates and condenses on the heterostructure surface. Different methods exist to heat the source and in our case the so called resistive evaporation is used. The idea is to pass a large current through a metallic wire or foil containing the material to be deposited. To take place, the procedure has to be performed in a high vacuum to ensure that the evaporated particles can travel directly to the deposition target without colliding with the background gas. At a typical pressure of 10^{-4}Pa, an 0.4 nm particle has a mean free path of 60 m. In a single evaporation run, many materials can be deposited on the substrate assuming the vacuum can be guaranteed during the hole time and that the different sources can be changed automatically. The deposition process is controlled via a crystal of quartz present in the evaporator. Quartz is a piezoelectrical solid used in electronics and is equivalent to an RLC circuit with a very precise resonance frequency. This frequency depends on different parameters but the one of interest is its mass. During the evaporation the effective mass of the quartz changes. By measuring the shift of the resonance one can derive the quantity of metal deposited. That way it is possible to control the thickness of the metal layer deposited with a precision better than the nanometer.
Finally, in order to reveal the metallic pattern a chemical solvent removes the remaining resist parts. This last step is called the lift-off and is done by using a solution of acetone or trichloroethylene. This is achieved by spraying directly the surface of the substrate or by leaving it a few minutes to several hours in the solution. Figure 1.4 illustrates these different microfabrication steps.
This microfabrication process is very general and widely used in the context of micro or nanoengineering. The three main steps presented in the next sections take advantage of the electronic lithography technique.

1.2.2 Ohmic contacts diffusion

To be able to perform transport experiments in the 2DEG one has to contact it first. Remember the gas is embedded in the heterostructure and no contact to the outer world exists a priori. This is why we need ohmic contacts through which we can bias the electron gas and detect the outcoming currents. The idea is to diffuse a metal alloy through the structure to define an electrical contact between the 2DEG and the surface.
To realize good electric contacts the technique used with GaAs HEMT is the rapid thermal annealing (RTA). Using this technique surface electrodes,

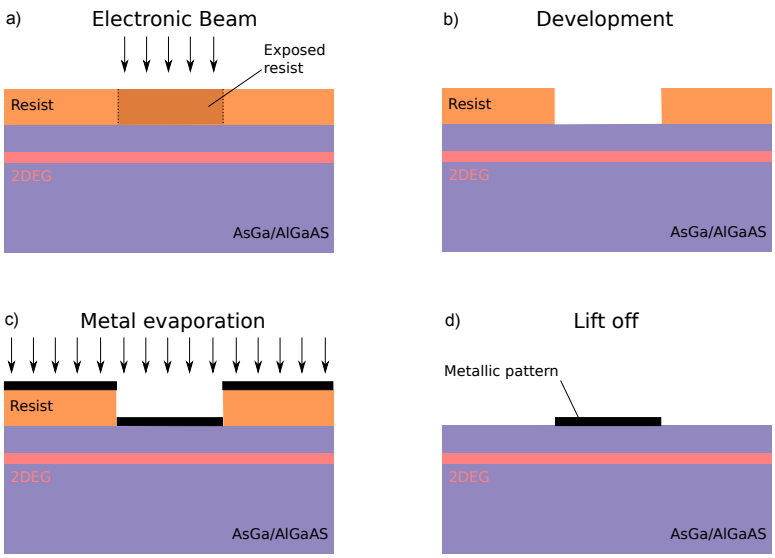

Figure 1.4: E-beam lithography basic process. a) An electron beam scans the resist following a chosen pattern. b) A positive tone pattern is revealed using a chemical developer such as MIBK:IPA. c) Metal is evaporated on the hole surface. d) The final metallic pattern is revealed by a lift-off procedure using a chemical solvent such as acetone or trichloroethylene.

with typical sizes 200μm by 200μm, are annealed on top of the wafer.
In the RTA process a stacked structure of Ni/Ge/Au/Ni/Au (10/60/120/20/200 nm), deposited using the procedure described in section 1.2.1 (see Fig. 1.4), is quickly heated from 20°C to 400°C and is kept at this temperature for a minute. The process takes place in a controlled hydrogen (H_2)/nitrogen (N_2) atmosphere to prevent oxidation. During the RTA, the metallic electrodes melt and diffuse into the heterostructure and form a ohmic contact to the 2DEG [17].
First of all the incorporation of germanium atoms plays two crucial roles in this case. On the one hand the association of gold and germanium forms a eutectic system with a melting point near 360°C. This temperature is much lower than the melting points of Au (1064°C) and Ge (937). At such high melting temperatures, Ga atoms would sublimate from the GaAs crystal, with a sublimation point at 490°C. The GaAs wafer would be destroyed before reaching the melting points of the pure metals. On the other hand germanium atoms provide dopants in the GaAs region near the metal interface reducing thereby the heterostructure diffusion barrier formed between the metals and the semiconductor. This is why the metal pads can diffuse into the semiconducting wafer and reach the electron gas.
Finally the nickel layer improves the uniformity of the contacts and enhances the adhesion of the electrodes to the GaAs substrate, facilitating the wire

bonding process on the ohmic pads.
The resultant resistance of 200μm by 200 μm contact after this treatment is typically of 10 kΩ at room temperature and 1kΩ at liquid helium temperature 4.2 K which means that several conduction modes exist at low temperature. This aspect will be discussed in the next chapter.

1.2.3 Mesa etching

Before going into the details of the etching of the heterostructure lets emphasize first that on a single piece of wafer tens of samples are fabricated during the complete process. All these different chips are all connected through the 2DEG. Therefore to separate them electrically the electron gas has to be etched. Another reason comes from the fact that each bonding pad connecting one sample to the measuring lines is made of a ohmic pad. This is obvious for the ohmic contacts but it is also the case for the metal gates as you will see in the next section. Without etching the 2DEG all these bonding pads would be shorted via the gas. The electrical isolation is guaranteed when all the Si donors in the AlGaAs layer are removed during the etching process, since they provide the electrons to form the 2DEG. The remaining unaffected regions by the etching form a conduction area called the "mesa".
Different methods can be used to etch a mesa. One can use wet etching where an acid solution attacks the surface of the wafer or dry etching where the surface is sputtered with an accelerated ion beam.
The ion beam etching (dry etching) method is used in our fabrication process. It consists essentially on a momentum-transfer sputtering process where the kinetic energy of the incoming ions is transferred to the surface atoms, ejecting them from the surface.. Lack of chemical component to the etch means that all materials etch at similar rates, depending only on their relative bond strength and atomic mass. A heavy inert gas such as argon is typically employed. In the case of a GaAs surface the ion beam energy should not exceed 40 keV which corresponds to the atomic displacement energy threshold for GaAs. Above this threshold an important disruption of the near-surface lattice is caused.
When shaping the heterostructure surface by dry etching, there are two established procedures. One is to etch completely down to the 2DEG and is known as deep etching. Another possibility called shallow etching is to stop the process in the layer which contains the dopants (20 nm from the surface). In that case, the lateral structure is defined by the periodic electrostatic potential given by the ionised donors. This last method produces smooth edges and is very well suited for narrow mesa patterns. Though our goal is not to make thin mesa structures the shallow etching method is used to etch the samples.
In order to selectively expose different areas of the surface of the heterostruc-

Drude conductivity σ	$\sigma = \frac{1}{R_{xx}}\frac{L}{W} = 0.034$ S
Electron density n_e	$n_e = \frac{B}{eR_{xy}} = 2.32 \times 10^{11}$ cm^{-2}
Fermi velocity v_F	$v_F = \frac{\hbar\sqrt{2\pi n_e}}{m^*} = 2.09 \times 10^5$ m.s^{-1}
Elastic scattering time τ_e	$\tau_e = \frac{m^*\sigma}{e^2 n_e} = 3.49 \times 10^{-11}$ s
Elastic mean free path l_e	$l_e = v_F\tau_e = \frac{h\sigma}{e^2\sqrt{2\pi n_e}} = 7.31 \times 10^{-6}$ m
Diffusion coefficient D	$D = \frac{1}{2}v_F l_e = \frac{\pi\hbar^2\sigma}{e^2 m^*} = 7628$ cm^2.s^{-1}
Electron mobility μ_e	$\mu_e = \frac{e\tau_e}{m^*} = \frac{\sigma}{n_e e} = 921000$ cm^2.V^{-1}.s^{-1}

Table 1.1: Electronic parameters of a high mobility heterostructure of AlGaAs extracted from quantum Hall measurements performed at 4 K. The different formulas relating these parameters have been specified.

ture, metal masks are used to protect the parts of the wafer that need to be kept unaffected. We utilize two different metal masks. One consists of the ohmic layer already deposited before the etching step. The second mask is an aluminium mask with a thickness of 60 nm deposited after the ohmic layer and again using the process described in figure 1.4. This mask enables to define specific shapes of the 2DEG such as wires, rings, hall bars or more complicated designs, which will then connect to the ohmic pads. In our case the 2DEG is given a hall bar shape. This choice is motivated by the fact that measuring the quantum Hall effect enables us to characterize the electronic parameters of our samples at liquid helium temperature. These parameters are listed in table 1.1.
Once the etching procedure finished, the aluminium mask is removed using a chemical solution of NaOH with a concentration of 0.1 mol.L^{-1}. The fabrication sequence can then end with the metal gates deposition.

1.2.4 Lateral gates deposition

In order to the define quantum dots, metal electrodes called lateral gates are necessary. These gates, deposited on top of the heterostructure, enable us to create electrical fields in the structure that deplete the electron gaz and gives the opportunity to confine electrons as mentioned in section 1.1.2 and depicted in figure 1.3. The electrical fields controlled via voltages applied on the metal gates will enable us to create tunnel barriers in the 2DEG, that as will see later are the basic requirement to form lateral quantum dots.
We now focus on the fabrication process of the lateral gates. It is important to note that the metal gates are the finest structures in our samples. The smallest parts which actually define the quantum dots, mainly quantum point contacts, can be of the order of the lithographic technique resolution we use, that is to say 20 nm wide. Obviously these fine gates have to be connected to the measurement cables through bonding wires and big bonding pads will be required as in the case of the ohmic contacts. An

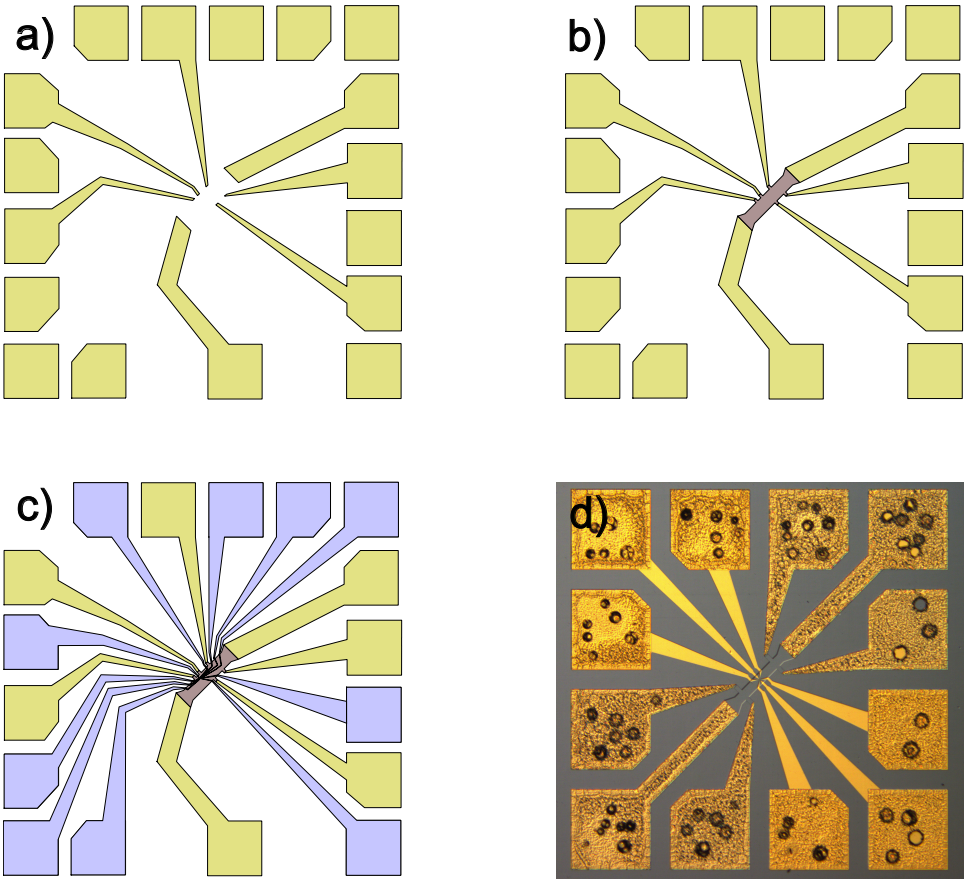

Figure 1.5: a) Deposition and RTA of the ohmic pads (yellow pattern). b) Shallow etching of the mesa defined by the ohmic layer and the brown area being the Hall bar. c) Deposition of the metallic gates (blue pattern). d) Microscope picture of quantum dot chip. The dark grey part is the etched surface. A brighter grey area is present in the middle of the sample and corresponds to the Hall bar. The Gold coloured and black spotted regions are the ohmics. Finally the gold shiny parts are the gates, the finer parts are not visible on this picture.

important point not mentioned before is the fact that during the ohmic step, ohmic pads are fabricated at the positions of the metal gates pads. The reason is simple : robust pads in order to microbond without damaging the metallic layer are required. Indeed ohmic pads are very suited for this task.
Given the range of sizes needed to define the gates, two different patterns are used : a fine gate pattern and a large gate pattern which will merge near

the mesa edge.
Again following the process shown in section 1.2.1 (Fig. 1.4) we first define the fine and large gate positive tone patterns in a single ebeam lithographic run on PMMA resist coated on the surface. Different exposure times under the beam and beam sizes are used to define these two patterns. Then a fine layer of titanium of 10 nm thickness and a thick gold layer of 100 nm are deposited on the surface. The evaporation of the two metals are done within a single step and in the same evaporator. The Ti layer simply ensures the gold layer to stick properly on the surface. Finally we reveal the metal gate pattern during the lift-off step.
Great care has to be taken concerning the lift-off of the metal gates since the very small sizes of the fine parts makes it a critical step. There are mainly two signatures of a bad lift-off. It can happen that some fine parts are missing, that is to say too much metal comes off. Second, connections between surface electrodes can occur, that is to say not enough metal comes off. Usually the evaporated samples are left several hours in the lift-off solution and subsequently, spraying this chemical solution onto the surface from different directions completes the lift-off.
Figure 1.5 summarizes briefly the complete fabrication process of a double quantum dot chip.

1.3 Quantum dot geometries

Thanks to nanoengineering, very few restrictions concerning the possible geometries and sizes for our quantum dots exist. In order to choose a specific geometry one has to take into account different parameters though. First of all the depletion length coming from the electrical field profile in the structure (Fig 1.3) reduces the effective size of the quantum dot and has to be taken into account in the lithographic patterns. As we will see in the next chapter the size of a quantum dot is directly related to its energy spectrum. The choice of the size has therefore to be taken carefully. Working with multiple quantum dots coupled to each others forces one to select their arrangement with caution : dots connected in series, in parallel or side coupled. Finally the widths and shapes of the different metallic gates defining the quantum wells are also crucial parameters to reach specific quantum regimes. A great example of these choices is the geometry of double quantum dots used in the few electron regimes to build spin based quantum bits [18].
To study Kondo physics our choice was to use two quantum dots coupled to each other. Though one quantum dot is sufficient to observe the Kondo effect [6], connecting a second one offers the possibility to probe much richer physics in this regime with a larger control. Exotic Kondo effects such as the two channel spin Kondo effect [8], the two channel orbital Kondo effect [19],

the SU(4) Kondo effect [20], or the Kondo box problem [10] [11] to name a few, are predicted by theory in such quantum dots.
The exact setup consists of two asymmetric quantum dots coupled to each other via a tunnel barrier controlled electrostatically. One of the quantum dots has a typical size of 400 nm +/- 100 nm which means large level spacing and charging energies. This small quantum dot can be addressed as an artificial atom or impurity. The second quantum dot has a much larger size going from 1μm to 2.5μm leading to reduced charging energies and vanishing level spacing. This large quantum dot is at the limit of being a continuum of quantum states and can be addressed as a reservoir with controllable number of electrons. The next chapter will introduce the formalism used to described quantum dots and explain the physical meaning of these different energy scales and their importance.
Each of these quantum dots is also connected to two metallic leads formed by the surrounding mesa. These leads enable to probe the system. Each transport experiment gives the conductance map through the device from which the quantum processes contributing to the current can be identified. The described geometry is quite versatile and enables us in theory to monitor all the currents coming out of the structure in response to one or several excitations. The choice of this particular geometry was motivated by recent theoretical proposals investigating the Kondo box problem in double quantum dots arranged in a T-shape geometry [10] [11], a problem where due to the finite size of the reservoir screening the local moment, the system undergoes a critical Kondo regime. Note that the T shape (Fig. 1.6, b), that can be achieved in a parallel quantum dots by tuning properly the device as we will show later on, was earlier used by Goldhaber-Gordon et al. [8] in order to study the two channel Kondo effect. In such a regime, a single impurity (small dot) is screened by two independent channels (reservoirs+large quantum dot) and a critical over-screening point is reached when the Kondo temperatures defined for each channel are equal. During this project, we chose to probe the system through the small quantum dot as proposed in [10], which was motivated by an early collaboration with the authors of the paper, Pascal Simon and Denis Feinberg.
Figure 1.6 shows a SEM picture of a double quantum dot chip used during this PhD (a) and a schematic representation of the T shape geometry (b). A scheme of the embedded quantum dots formed via the surface electrodes for this specific design is shown for clarity (c).

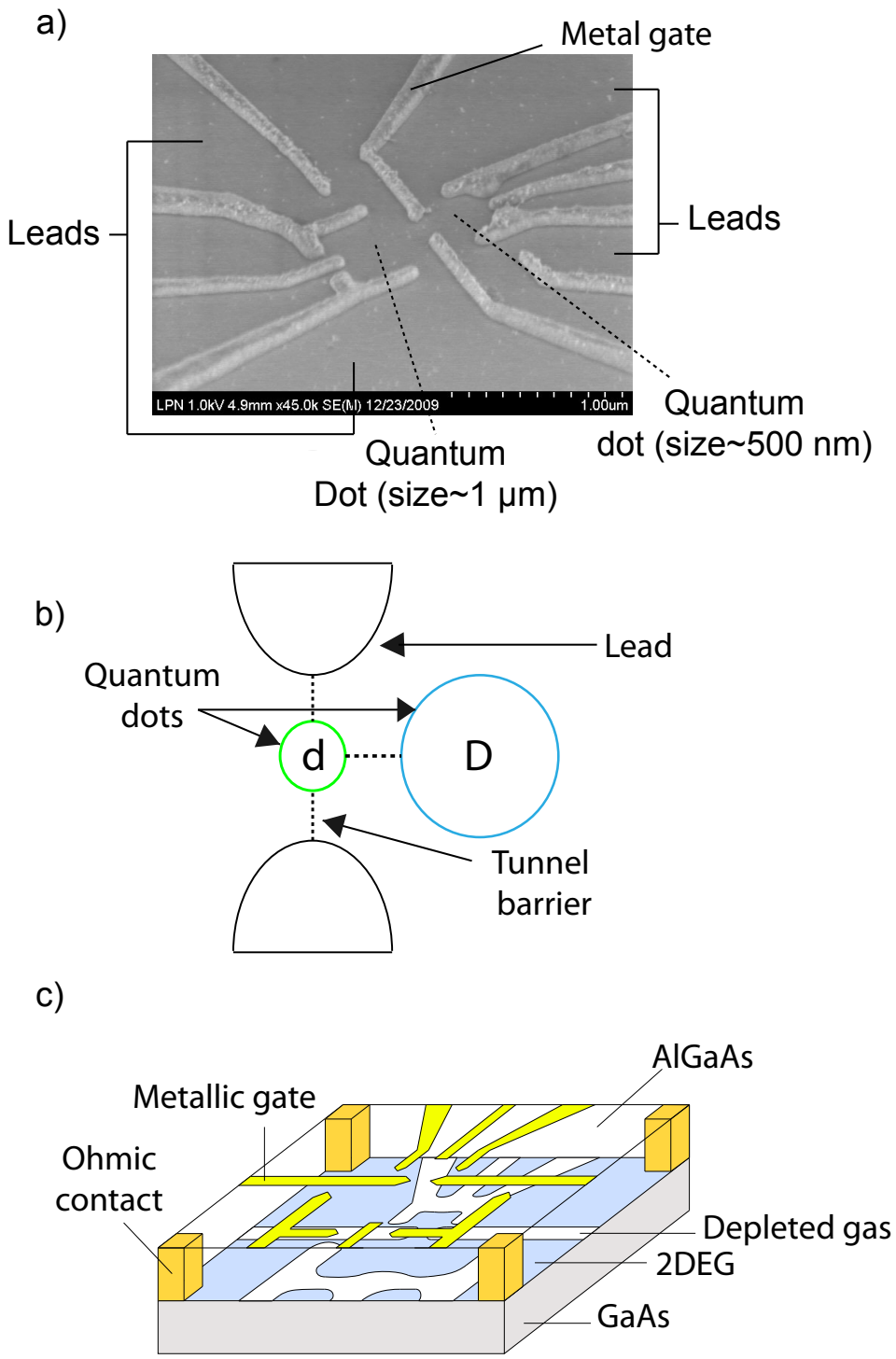

Figure 1.6: a) SEM picture of double quantum dots coupled in parallel. b) Schematic representation of the double dots arranged in a T shape. c) Schematic representation of the electrostatically defined quantum dots coupled in parallel.

Chapter 2

Elements of theory

This chapter is dedicated to the understanding of transport through quantum dots. First we will introduce the Landauer Büttiker formalism necessary to apprehend coherent conductors. This will enable us to describe a basic component of a lateral quantum dot : the quantum point contact. By combining this formalism with a semiclassical approach we will derive a simple model to describe transport process in a quantum dot and introduce the Coulomb blockade phenomenon. Extending the model to a double quantum dot we will be able to extract its stability diagram, the so called honeycomb diagram. We will interest ourselves to the influence of the coupling between the dots on the honeycomb diagrams. Finally we will go beyond the Coulomb blockade process and introduce the cotunneling events. The chapter will be closed on the relation between cotunneling and the Kondo effect in the framework of the Anderson model.
For each section experimental data acquired within the frame of this thesis project will be confronted to theory. This choice is motivated by the fact that lateral quantum dots physics started in the group with this project. Thereby the observation of these different processes where key steps in our understanding of transport through quantum dots and occupied an important part of this PhD.

2.1 Landauer-Büttiker formalism

When the size of a conductor is made smaller and smaller the importance of quantum effects no more allows a classical description of the electron. One has now to take into account the undulatory nature of matter and coherence. This quantum nature has to be considered as soon as the typical size of the conductor is of the order or smaller than the phase coherence length (L_ϕ) of the electron. This physical observable is the length on which an electron travels in the conductor with a well defined phase associated to its wave

function[1]. To give an idea, weak localisation experiments were performed in the group on quasi 1D wires etched in GaAs heterostructures [21]. These measurements extracted a L_ϕ greater than 10 μm at 30 mK! In this frame the Ohm's law does not stand anymore and a new formalism is required to understand transport. A first step was realised by Landauer who proposed that conduction in a coherent 1D system could be viewed as a transmission problem [22]. Later Büttiker extended this formalism to a multiterminal geometry [23]. The idea is to model the coherent electron propagation with conduction modes, as in the case of light propagation in an optical wave guide. In that case the formula giving the conductance stands as:

$$G = \frac{e^2}{h} \sum_{k,\sigma} T_{k,\sigma} \tag{2.1}$$

where $\frac{e^2}{h}$ is the quantum of conductance and $T_{k,\sigma}$ represent the transmission probabilities of each conduction mode. The k and σ indexes identify the wave vector and spin of each mode. They depend on the conductor under consideration. For a 1D system with a single conduction mode and in the absence of magnetic field, the conductance can reach $\frac{2e^2}{h}$ for perfect transmission. The quantification of the conductance as introduced by Landauer and Büttiker will be illustrated in the next section by studying quantum point contacts (QPC) which are the basic ingredients required to define lateral quantum dots.
Moreover, we can take advantage of this formalism to describe conduction through a quantum dot. However this more delicate situation where electron-electron interactions play an important role cannot be simply addressed through a set of transmissions coefficients and this formula has to be adapted to get a suitable description.

2.2 Quantum point contacts

A quantum point contact is basically a constriction in a conductor forcing all the conduction electrons to flow through a narrow gap. This constriction is realised electrostatically by depleting the 2DEG with a set of gates that we refer to as split gates [24] [25]. It consists of two gates facing each other and separated usually by 200 nm (Fig. 2.1, left panel). The depleted region formed between the gates is controlled continuously via the voltages applied on them.
In a conductor, we know that electrons contributing to the current have a certain momentum/wavelength called Fermi momentum/wavelength. The

[1]The coupling of the electron to the environment, such as a phonon bath, leads to inelastic collisions which limit the phase coherence length. On length scales smaller than L_ϕ, interference effects have to be taken into account

transverse confinement in the quantum point contact results in a quantisation of the transverse motion. The electron wave can only pass through the constriction if it interferes constructively, in other word if its wave length satisfies the boundary conditions defined by the transverse confinement through the QPC. For a given size of constriction, this only happens for a certain number of modes N. The current carried by such a quantum state is the product of the velocity times the electron density. These two quantities by themselves differ from one mode to the other, but their product is mode independent. As a consequence, each state contributes the same amount, $\frac{e^2}{h}$ per spin direction (perfect transmission) in agreement with the Landauer-Büttiker formalism. The different conduction modes can be closed one by one by changing the gate voltages which affects the width of the constriction.

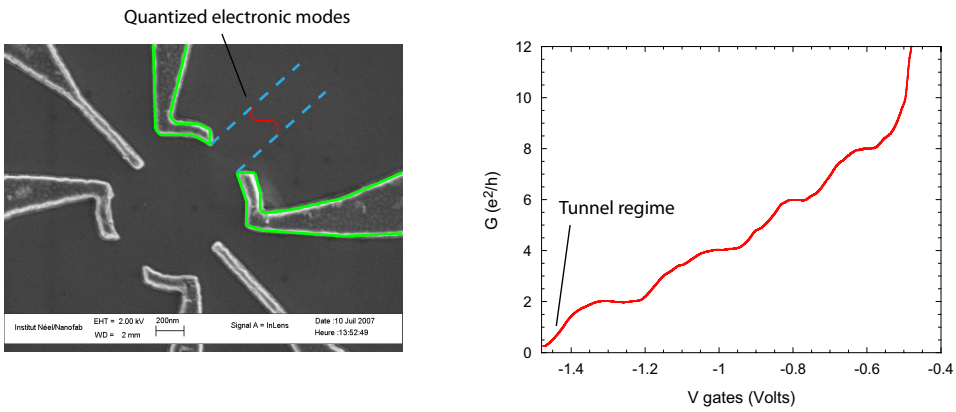

Figure 2.1: Left panel : SEM picture of a quantum dot formed with a set of quantum point contacts. The green lines delimit a single quantum point contact. Quantized electronic modes have been represented near the QPC. Right panel : Conductance measured through the QPC marked with green lines when the voltages on the gates are swept. A staircase in multiples of $\frac{2e^2}{h}$ appears showing the different conduction modes reflected by the QPC one by one. After the last mode has been close we enter the tunnelling regime.

This is shown in figure 2.1, where the evolution of the conductance through a break junction is plotted versus the surface electrodes voltages. The staircase in units of $\frac{e^2}{h}$ illustrates the validity of the Landauer-Büttiker formalism, the factor two coming from the spin degeneracy. It is worth noticing that the conductance plateaus are not perfectly defined. Beyond thermal broadening, this effect can be attributed to the specific design of the QPC we used. In the limit where the width of the constriction varies very slowly, the so called adiabatic limit, exponentially sharp conductance steps are expected [26]. However, from our SEM picture (Fig. 2.1) we see that we are

far from this limit. In our case, parasitic transmission due to longitudinal resonances along the constriction tend to deviate the conductance behaviour from the perfect staircase picture [27] [28].
After the last mode has been closed, conduction occurs only through tunnelling events. In this regime the QPC forms a tunnel barrier. The threshold after which the conductance drops to zero is called the pinch off. Using a specific set of QPCs one can surround a small area of the 2DEG with tunnel barriers and form a quantum dot. This particular point will be discussed in section 2.3.2.

2.3 Transport through a quantum dot

As we will see in the following, quantum dots have a discrete addition energy spectrum due to they small size. In other words, a finite energy will have to be paid in order to add/remove electrons from the quantum dot. It will be shown that the origin of the finite addition energy comes from the confinement potential and the electron-electron interactions.
We will take advantage of the discreteness of the addition energy spectrum by considering the electrochemical potential of a dot that is related to fluctuations of the number of particles confined. Since we are interested in transport measurements, this quantity will lead us to a natural description of conductance through the device. A simple formula giving the electrochemical potential of a quantum dot can be derived by combining the one particle energies of the dot and a constant interaction term describing the electron-electron interactions in the dot.

2.3.1 Quantization of the energy levels

When electrons are confined in a region of space comparable to their wavelength, in our case the Fermi wavelength, quantum effects become extremely important, in particular the discrete nature of their energy spectrum. For simplicity we will not consider the effect of electron-electron interactions for the moment. This will be done in the next section and we only focus here on the one particle energy spectrum of an electron in a quantum well. To illustrate the quantization of the energy we consider the quantum harmonic oscillator problem, i.e. the quantum mechanical analogue of the classical harmonic oscillator. This model is of great importance in quantum mechanics since an arbitrary potential can be approximated as a harmonic potential at the vicinity of the stable equilibrium point. We then make the assumption that the electrons of the 2DEG confined electrostatically are subject to a parabolic potential (i.e. harmonic). Following Landau's work who was the first to address this problem in an other context [29], one finds the expression

of the energy levels in 1D harmonic oscillator :

$$E_n = \hbar\omega(n + 1/2), \qquad \omega = \sqrt{\frac{k}{m*}} \tag{2.2}$$

where ω is the characteristic angular frequency of the oscillator depending on the strength of the potential. ω is a function of the force or spring constant k and the effective electron mass m^* equal to 0.067 m_e in AlGaAs/GaAS. n represents the quantum number labelling each quantum state in the well. We see that the energy spectrum is quantized and can only take half integer multiple values of $\hbar\omega$. To transfer an electron from the n quantum state to the $n + 1$ there is a finite cost to pay.

$$\Delta E_{n\rightarrow n+1} = \hbar\omega \tag{2.3}$$

We refer to this energy scale of the dot as the level spacing. Since ω is proportional to $1/x^2$, x being the displacement of the electron in the well, we notice this energy will grow rapidly when the size of the quantum dot is made smaller. All the formulas derived in this section are only valid in a 1D problem. We know that lateral quantum dots are defined in a two dimensional space. It should be noted that a generalization to a 2D harmonic oscillator can be done and leads to the Fock-Darwin states which exhibits a discrete energy spectrum parametrized by an angular frequency ω proportional to $1/r^2$, a radial quantum number n and in addition an angular momentum quantum number l [30]. Note that our aim is not to address the exact one particle energy spectrum of a quantum dot. The main point of importance here is to note that the confinement potential leads to a discrete one particle energy spectrum (no interactions).
For a quantum dot with a typical size of 500 nm (pattern) the measured level spacing is $\Delta E_n \simeq 150\mu eV$. If we convert this electron-volts energy scale to Kelvins, $eV = k_B T$, we find $\Delta E_n \simeq 1.5K$. To be able to resolve experimentally the level spacing of such a quantum dot, low temperature measurements are required, typically 100 mK or better.
For a complete description of a quantum dot, one needs to take into account the interactions between electrons. This will introduce a new energy scale, the charging energy.

2.3.2 Electron-electron interactions

The electron-electron interaction is actually a complicated problem in itself, particularly when dealing with multiple particles. However a simple way to take into account these interactions in a quantum dot is to describe it as a capacitor [31]. To pass current through the structure it is obvious that the number of electrons in it should fluctuate. The idea is to think of this process as an equivalent of the charging and discharging process of a capacitor. That

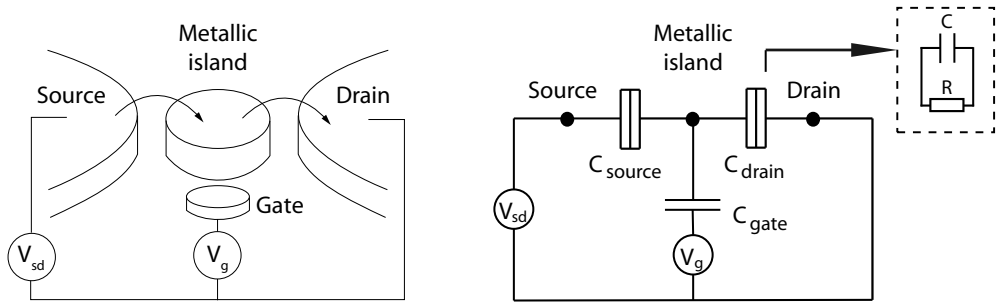

Figure 2.2: Schematic representation of a quantum dot connected to two metallic reservoirs and a back gate controlling the electronic density. The equivalent circuit is shown of the right side of the figure. The symbol developed on the top inset corresponds to a tunnel barrier symbol modelled with a capacitor in parallel with a resistance.

way the Coulomb interactions will be absorbed in a geometrical factor being the capacitance of the metallic island. For simplicity we ignore the level spacing here and work in a classical framework. The circuit we use at this point to describe the quantum dot is a transistor. Therefore we consider a metallic island connected through tunnel barriers to two electronic reservoirs called source and drain from which the current is driven. A back gate or plunger gate is capacitively coupled to the island and controls the electronic density in it. A schematic representation of such a device and the equivalent circuit are given in figure 2.2. The minimal energy required to charge the metallic island stands as :

$$E_C = \frac{e^2}{C_\Sigma}, \qquad C_\Sigma = C_{source} + C_{drain} + C_{gate} \tag{2.4}$$

where C_Σ is the total capacitance of the island. This energy represents the energy to bring a single electron from the non interacting leads to the dot. The smaller the capacitor, the smaller the dot is and the larger the charging energy is. From experiments performed on quantum dots of a few hundred of nanometers of diameter, the measured charging energy is of the order of the meV. This is a huge energy scale, almost 10 Kelvins ! Assuming this simple circuit is cooled down at a temperature much lower than E_C and that the bias voltage across the island is also smaller than E_C, this model suggests that the charge on the island is fixed and discrete.
However a purely capacitive model is not realistic. As depicted in figure 2.2 the coupling of the dot to the leads is a tunnel coupling. A correct treatment of such a coupling is complex and has to be done in the frame of quantum mechanics. For simplicity we just refine the model by adding a resistor in parallel to the capacitor to describe the coupling to the reservoir. This will enable a semiclassical description to test the range of validity of the previous

model. To do so we use the Heisenberg incertitude principle. According to this principle a quantum system undergoes energy fluctuations within a related time window:

$$\Delta E \Delta t \geq \frac{\hbar}{2} \tag{2.5}$$

Translating this in terms of charge fluctuations in a simple form:

$$\frac{e^2}{C} \times RC \geq \frac{\hbar}{2} \Longleftrightarrow G \leq \frac{2e^2}{\hbar} \tag{2.6}$$

The intrinsic charge fluctuations of the dot will develop on a time scale actually related to the resistance that couples it to the electronic reservoirs. To avoid the dot to fluctuate on small time scales we end up with the fact that the barriers forming the dot have to be in the tunnel regime, see section 2.2. In other words, in the tunnelling regime, the charging energy protects the system from charge fluctuations and defines the number of electrons in the dot.
We now have to combine the charging energy and the level spacing in a single formalism to derive the conditions required to pass current through a quantum dot.

2.3.3 The electrochemical potential

In transport experiments, a suitable quantity to focus on is the electrochemical potential that combines the concepts of energy stored in the form of chemical and electrostatic potentials. This quantity relates the change in energy with the change of the number of particles in the system.
Before starting we make two main assumptions in order to take advantage of the energy scales derived earlier. First the interactions among electrons in the dot and also between electrons in the dot and those present in the local environment, are parametrized by a constant capacitance C. Second the discrete energy spectrum can be described independent of the number of electrons is the dot. This model is known as the constant interaction model.
We consider the transistor set-up depicted in figure 2.2 and write down the total energy of the dot as the sum of the electrostatic energy and the single particle states [32]. At zero temperature this energy reads:

$$U(N) = \frac{[-|e|(N - N_0) + C_g V_g + C_L V_L + C_R V_R]^2}{2C} + \sum_{n=1}^{N} E_n \tag{2.7}$$

The first term corresponds to the electrostatic part. The dot contains N electrons at a set V_g, V_L, V_R of voltages applied on the plunger gate, the source and the drain leads respectively. N_0 is the number of electrons on the dot when no voltage is applied on these gates and which compensates the positive background charge originating from the donors in the heterostructure ($N < N_0$). The terms $C_g V_g$, $C_L V_L$ and $C_R V_R$, represent the continuous

charge induced on the dot by the voltages applied on the gate and leads. The last term corresponds to the single particle states.
The minimum energy for adding the Nth electron to the system is by definition the electrochemical potential:

$$\mu_{dot}(N) = U(N) - U(N-1) \tag{2.8}$$

For vanishing source and drain voltages this yields:

$$\mu_{dot}(N) = \frac{e^2}{C}(N - \frac{1}{2}) - e\alpha_g V_g + E_N \tag{2.9}$$

where we defined α_g as $\frac{C_g}{C}$ with C is the total capacitance of the dot (Eq. 2.4). The alpha factor represents the lever arm of the plunger gate. When, at fixed gate voltage, the number of electrons in the dot is changed by one, the electrochemical potential is changed by :

$$\mu_{dot}(N+1) - \mu_{dot}(N) = \frac{e^2}{C} + (E_{N+1} - E_N) = E_{add} \tag{2.10}$$

This energy change is called the addition energy [33]. The conclusion, as sensed in the previous sections, is that there is finite energy cost to add a single electron to the system. A complete description of the dot and its environment indicates that this cost is the sum of the electrostatic contribution to charge the dot and the orbital contribution to occupy a given orbital state $(E_{N+1} - E_N)$. This simple statement has important consequences on the transport through a quantum dot as we are going to see.

2.3.4 Coulomb blockade

Intuitively if E_{add} is larger than any other energy scale such as temperature or bias across the dot, we can perceive that this high energy cost can block the transport through the dot. To illustrate this statement, we make use of the potential landscape forming the quantum dot as shown in figure 2.3a. We represented the electrochemical potentials in the dot for $N+1$, N and $N-1$ electrons confined. The $(N+1)^{th}$ electron cannot tunnel in the dot because the electrochemical potential $\mu_{dot}(N+1)$ is larger than the potentials of the reservoirs. The Nth electron cannot tunnel out off the dot since all states in the reservoirs at an energy $\mu_{dot}(N)$ are occupied. In this situation the number of electrons on the dot is fixed, no current can flow through the system. This important phenomenon is called the Coulomb blockade [34].
Starting from a completely blocked system, different options exist to lift the Coulomb blockade. One is to change the potential of the dot by means of the plunger gate. By applying a negative voltage on this gate, the potential of the dot is reduced. In the situation depicted in figure 2.3b, an electron can now tunnel from the source (left lead) to the dot since $\mu_L > \mu_{dot}(N+1)$.

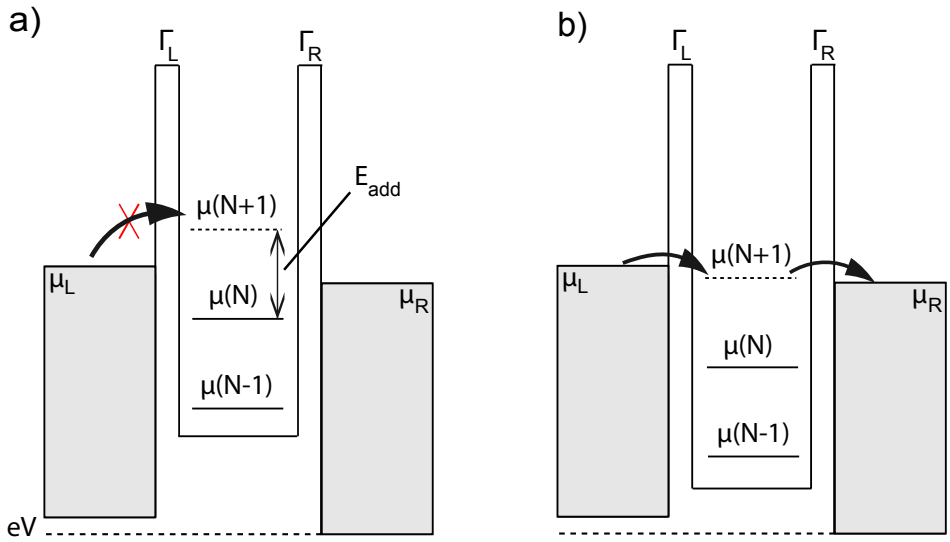

Figure 2.3: Potential landscape of a quantum dot induced by the gates at zero temperature. The states in the reservoirs are continuously filled up to the electrochemical potentials μ_L and μ_R. We assume to be in the linear transport regime, $eV \ll \Delta E, \frac{e^2}{C}$. The discrete states in the dot are filled with N electrons up to $\mu_{dot}(N)$. The addition of one electron in the dot would raise the electrochemical potential to $\mu_{dot}(N+1)$. In the energetic configuration depicted in (a), the addition is blocked. By lowering the potential of the dot with a plunger gate, one can align $\mu_{dot}(N+1)$ in the bias window (b). Transport can now take place. The total charge on the dot oscillates between N and $N+1$.

This causes the electrochemical potential μ_{dot} to shift by $\Delta E + \frac{e^2}{C}$. Now $\mu_{dot}(N+1) > \mu_R$, one electron can tunnel out off the dot to the drain reservoir (right lead), thereby causing the electrochemical potential to drop back to μ_{dot}. Once the sequence finished, a new electron can repeat the cycle $N \longrightarrow N+1 \longrightarrow N$. This particular operating mode is called a charge degeneracy point, where actually two charge configurations minimize at the same time the total energy of the dot. The number of electrons fluctuates between the two configurations leading to a current as mentioned. Note that only one electron is involved in the tunnelling sequence. This process where current is carried by a succession of discrete charging and discharging of the dot is known as single electron tunnelling [35].
By sweeping the plunger gate voltage, the electrochemical potential of the dot is shifted continuously. The conductance through the device then oscillates from zero, corresponding to the Coulomb blockade regions, to finite values, where single electron tunnelling occurs [36]. In the Coulomb valleys the number N of electrons in the dot is fixed. On a Coulomb peak the num-

ber of electrons in the dot fluctuates between N and N+1. Quantum dots are often referred to as Single Electron Transistors (SET) because of this "on/off" behaviour. The voltage separating two consecutive peaks is related to the addition energy. The period ΔV_g of the oscillations can be obtained from equation 2.9 under the condition $\mu_{dot}(N, V_g) = \mu_{dot}(N+1, V_g + \Delta V_g)$:

$$\Delta V_g = \frac{1}{e\alpha_g}\left(\frac{e^2}{C} + \Delta E\right) \tag{2.11}$$

In the case of spin degenerate states, two periods should be observed. One period corresponds to the Nth and $(N+1)^{th}$ electrons having opposite spins and occupying the same orbital state. The other is related to the $(N+1)^{th}$ and $(N+2)^{th}$ electrons being in different orbitals.

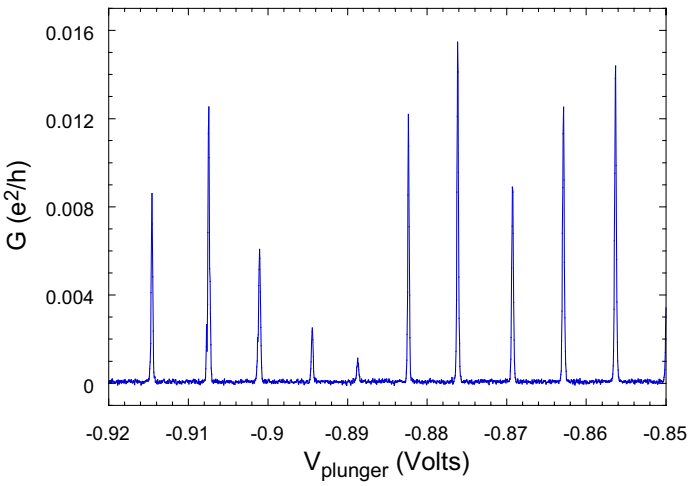

Figure 2.4: Typical measurement of Coulomb blockade oscillations performed on a single dot at a temperature of 20 mK. The random variation of the peaks amplitude can be attributed to the random coupling between each discrete state and the reservoirs.

Figure 2.4 shows a typical measurement of Coulomb blockade through a quantum dot in the linear transport regime, i.e. $eV \ll \Delta E, \frac{e^2}{C}$, and at a temperature of 20 mK. The dot has a diameter of 1500 nm with a charging energy of $E_C = 300\mu eV$ and a level spacing $\Delta E = 20\mu eV$. These energy scales were not extracted from the conductance plot. According to equation 2.11, the α factor has to be known to be able to do so. To access the arm lever value, a non linear spectroscopy experiment is necessary. This will be the purpose of the next section. However we do see that the conductance exhibits sharp oscillations separated by large regions where transport

through the dot is completely suppressed, emphasizing the dramatic influence of the Coulomb blockade on transport. Notice that the spacing between the peaks appears to be very regular in this experiment. Due to the large ratio $E_C/\Delta E$ in this quantum dot, the charging energy dominates transport. This explains the fact that the Coulomb blockade oscillations seem ti have a single period here.

So far we did not mention the effect of temperature. Actually the line shape of the Coulomb peaks depends strongly on temperature. Three temperature limits can be distinguished, assuming the coupling between the dot and the reservoirs is negligible [37]:

- The low temperature or quantum limit: $\Gamma_{dot-leads} < k_BT < \Delta E < E_C$.
- The classical limit : $\Gamma_{dot-leads} < \Delta E < k_BT < E_C$
- The high temperature limit : $\Gamma_{dot-leads} < \Delta E < E_C < k_BT$

The strong coupling limit of none negligible $\Gamma_{dot-leads}$ will be addressed later.
We only discuss here about the low temperature limit, that is to say when $\Gamma_{dot-leads} < k_BT < \Delta E, E_C$. In this limit, the quantum states are resolved. Tunnelling events only involve single discrete energy states. The line shape of the Coulomb peak can be approximated by [37]:

$$G = G_{max}\, cosh^{-2}\left(\frac{\alpha_g(V_g^{res} - V_g)}{2k_BT}\right), \qquad G_{max} = \frac{e^2}{4k_BT}\frac{\Gamma_L\Gamma_R}{\Gamma_L + \Gamma_R} \quad (2.12)$$

V_g^{res} is the position of the resonance peak on the gate voltage axis. The tunnel rates Γ_L and Γ_R entering the contrast factor, actually depend on the state under consideration. Strictly speaking there is no reason that all the orbitals of the dot couple exactly the same way to the leads. In practice, one expects that for each orbital the spatial distribution of the electron is unique, yet differs weakly from the others. From the spatial distribution one can access the overlap of the wave function of an electron in the dot, and the wave function of an electron in the leads (plane waves). The conclusion is that one can label each orbital with a unique effective tunnel rate. In the quantum limit, transport through the dot is sensitive to this unicity . The random variation in the peaks amplitude of figure 2.4 illustrates this fact. It is worth noting that beyond the constant interaction model, adding an electron to a finite interacting region actually perturbates the other electrons. Despite the variation of the charging energy (expected to be weak for large dots holding an important number of electrons), the nature itself of the confining potential will be affected, thereby affecting the wave functions within the dot and there overlap with the quasi particles plane waves in the

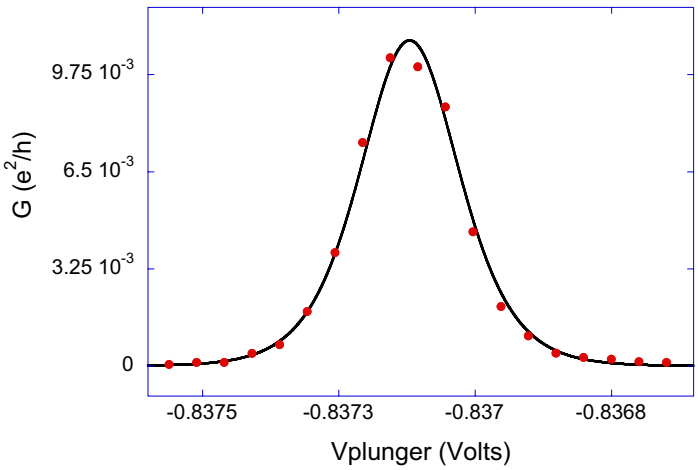

Figure 2.5: Single Coulomb peak fitted using equation 2.12. The red points corresponds to the experimental data. The black line corresponds to the fit. The effective electronic temperature extracted is 40 mK.

metallic leads. This effect is know as scrambling [38].
A fit to equation 2.12 on one of the peaks present in the measurement, enables us to extract the effective electron temperature in our device at the base temperature of our dilution refrigerator (20mK). The electronic temperature extracted from the fit performed in figure 2.5 is 40 mK. Resistance measurements versus temperature done earlier on identical AlGaAs/GaAs wafers, have extracted a saturation temperature of 30 mK for the electrons. From these measurements we estimate the electronic temperature in our samples to be of the order of 30-40 mK which is slightly above the base temperature of our dilution refrigerator[2]. We believe that the saturation temperature of the Coulomb peaks width is not related to Γ broadening but comes from a lack of filtering a high frequency[3]. We will discuss this point later when dealing with electronics and noise in the experimental setup.

2.3.5 Stability diagrams

So far we only worked in the linear transport regime. We are going to focus now on the non linear transport regime, i.e. when $eV > k_BT, \Delta E, E_C$, in order to get a complete spectroscopy of the energy spectrum of the dot. To match the experimental setup we use in practice, we assume the right lead

[2]Measurements performed at 10 mK give the same electronic temperature in both experiments.

[3]At frequencies around 500 MHz, the low frequency filters and high frequency filters we use do not recover properly and could therefore explain the difficulties we have to cool down electrons below 30 mK.

is grounded, so $V_R = 0$[4]. The bias voltage will be applied on the left lead, $V_L = V_{bias}$. Equation 2.9 reads now :

$$\mu_{dot}(N) = \frac{e^2}{C}(N - \frac{1}{2}) - e\alpha_g V_g - e\alpha_L V_L + E_N \tag{2.13}$$

where $\alpha_L = C_L/C$ (see section 2.3.3, $alpha_g$). The minimum condition for a tunnelling event to occur through the ground state of the dot, is that its electrochemical potential aligns with at least one of the electrochemical potentials of the leads. This defines the following conditions :

$$\mu_{dot}(N) = \mu_R = 0 \tag{2.14}$$
$$\mu_{dot}(N) = \mu_L = -eV_L \tag{2.15}$$

This corresponds to lines in the (V_g, V_{bias}) diagram that form domains enclosing the blockade regions. The equations of these lines given by the previous conditions stand as :

$$V_L \propto -\frac{C_g}{C_L} \times V_g + \text{constant} \tag{2.16}$$
$$V_L \propto \frac{C_g}{C_R + C_g} \times V_g + \text{constant} \tag{2.17}$$

By combining the lines corresponding to different occupations numbers in the dot, we can dress the regions in the (V_g, V_{bias}) space where the quantum dot is blocked. The different lines enclosing a blockade area form a diamond shape. In each diamond the number of electrons confined is fixed. The borders of the diamonds define the sets (V_g, V_{bias}) for which transport occurs through the ground state. We refer to them as Coulomb diamonds.
In terms of transport through the dot, crossing the border of the diamond implies that the current through the system increases sharply as the blockade is lifted. Rather than monitoring current through the system, a usual method used to gain sensitivity and obtain good resolution of the Coulomb diamonds is to probe the differential conductance dI/dV_{bias}. Thereby, instead of focusing on the absolute value of the current, more interest is put in the relative variation of the current through the quantum dot as a function of the bias voltage. That way a better contrast in non linear measurements can be obtained. For a dI/dV measurements we refer the reader to [39] and [40].
Figure 2.6 is a schematic colour plot of the differential conductance[5] through

[4]To study transport through a dot, we apply a bias voltage on one lead and keep the other lead connected to ground

[5]The color scale is related to the value of the differential conductance dI/dV. In Figure 2.6, a binary colour code has been used : white corresponds to zero differential conductance, blue corresponds to finite differential conductance.

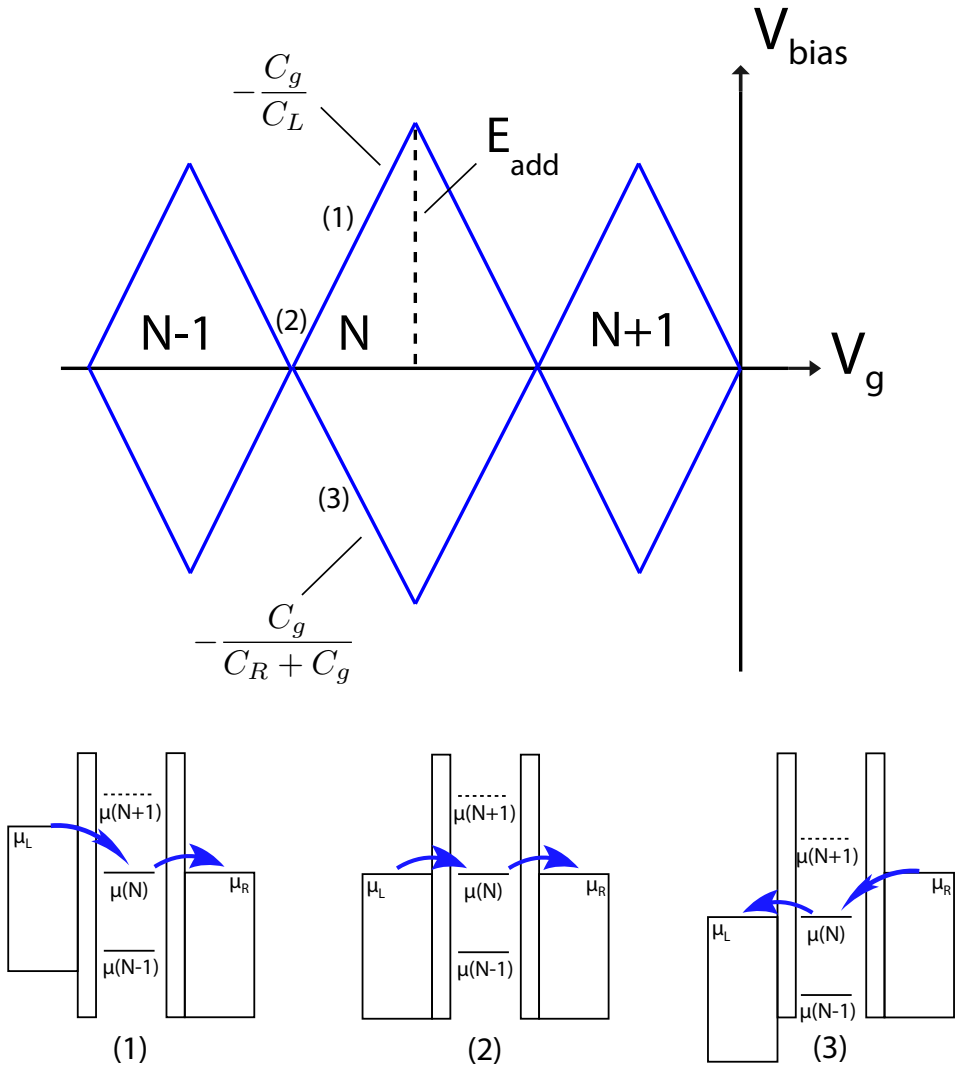

Figure 2.6: Schematic colour plot of the differential conductance through the dot versus the voltage bias and the plunger gate voltage. The diamond regions in the (V_g, V_{bias}) space enable to extract different important parameters of the dot: $E_{add}, \Delta V_g, \alpha_g$ and the different capacitances. Schemes inserted at the bottom of the figure show the alignment of the electrochemical potential of the dot with the leads in different areas of the stability diagram.

the system and shows Coulomb diamonds for symmetric tunnel barriers. A diamonds hight in the V_{bias} direction gives the addition energy. We omitted the factor $\frac{1}{e}$ for simplicity. The length of a diamond on the V_g axis gives ΔV_g from which we can extract now the α_g factor. All the capacitances can

at this point be determined.

Beyond transport through the ground states, multiple excitations exist in the system. The excitation spectrum can be probed in non linear transport. To be able to visit an excited state an electron needs to have enough energy to jump to the next orbital state or higher. In the framework of tunnelling, the incoming electrons on the dot have to first have enough energy to visit the ground state (resonance). The excess of energy within regards to the ground state can be used to occupy a higher orbital state. In other words excited states can be observed beyond the borders of the diamonds 2.7. We know the excitation spectrum is quantized. Then, starting from the border of a diamond at fixed V_g one needs to open the bias window by an amount : $\Delta V_{bias} = m\Delta E$. Where m is an integer number and assuming the level spacing is constant. If not ΔV_{bias} has simply to match the different ΔE_n of the system. When this condition is met the incoming electron has now different paths to go through the dot, which leads to an increase of the current detected. Since we are measuring the variation of the current through the dot via a dI/dV measurement, the result in the (V_g, V_{bias}) stability diagram is the presence of extra lines parallel to the borders of the diamonds indicating the increase of the local conductance [40]. Each line corresponds to a given excited state aligning in the conduction window. For a given number of electrons N, we define $\mu^*_{dot}(N)$ to be the electrochemical potential corresponding to an excitation of the ground state $\mu_{dot}(N)$.
Figure 2.7 shows a typical non linear transport experiment through a single quantum dot. The differential conductance $\frac{dI}{dV}$ (colours) is monitored as a function of V_{bias} and V_g. We see that this experiment is in good agreement with the simple constant interaction model. First of all, we clearly observe the Coulomb diamonds in dark blue where no current through the system is detected. Then, once the Coulomb blockade is lifted (borders of diamonds), extra lines appear corresponding to excited states aligning in the bias window with the ground state. From the distance separating two consecutive and parallel lines, one can extract the value of the level spacing. However asymmetries and deviations exist :

- The diamonds are tilted. This is a signature of a detuning of the tunnel barriers which leads to a detuning of the capacitances C_L and C_R affecting the degeneracy lines of the Coulomb diamonds. This also reflects in an asymmetry of the color contrast for positive and negative bias.

- The contrast decreases with decreasing plunger gate voltage. This can be due to a difference of coupling to the leads, of the charge states participating to the transport (see section 2.3.4). A charge state better coupled will result in a stronger conductance through the system. It can also be due to cross talk between the gates. The voltage applied

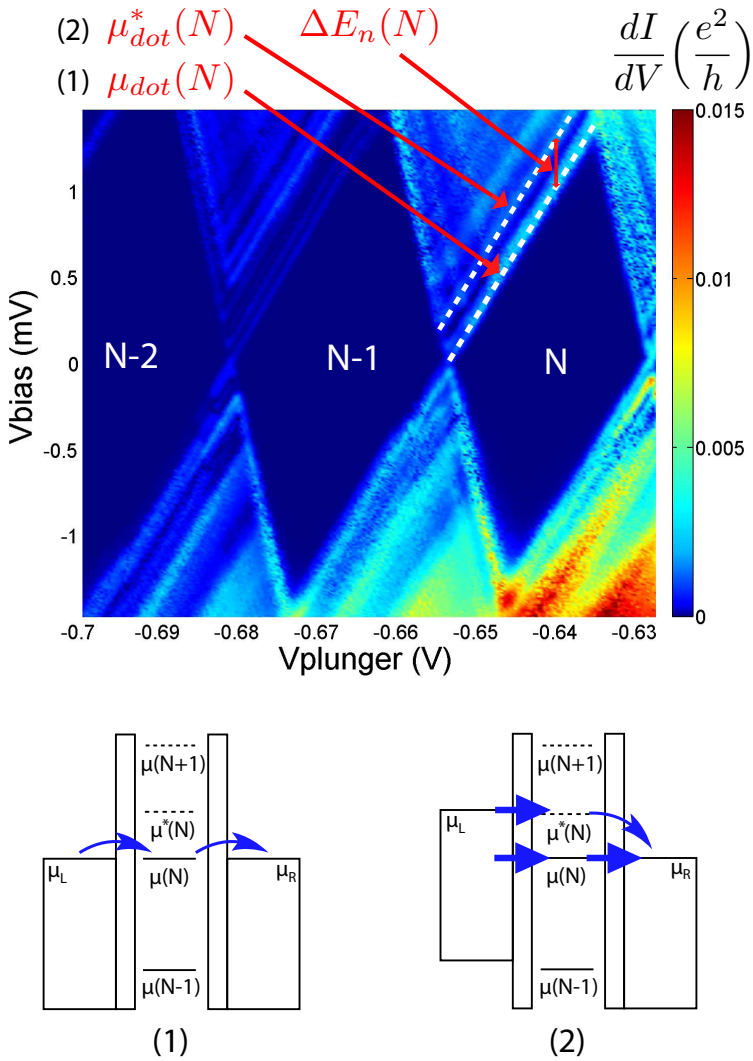

Figure 2.7: *Top.* $\frac{dI}{dV}$ colour plot as function of V_{bias} and V_g monitored at 20 mK in a quantum dot with a size of 300 nm. The dark blue regions in the diamonds correspond to the blockade regions. Above the borders of the diamonds, extra lines corresponding to excited states are clearly visible. The distance in the V_{bias} direction separating two parallel lines correspond to the excitations energies $\Delta E_n(N)$. *Bottom.* Schematic representations of the transport through the ground state and through the first excited state. Even though two states align in the bias window, only one electron can tunnel at a time.

on the plunger gate influences the voltages on the tunnel barrier gates and can lead to detuning of their transparencies.

- The size of the diamonds increases with decreasing gate voltage. By applying a more and more negative voltage on the plunger gate, the dot is effectively squeezed. A size reduction then leads to an increase of the addition energy.

- The level spacing is not strictly speaking a constant as anticipated previously.

2.4 Transport through double quantum dots

Now that we have the basic ingredients to understand transport through a single quantum dot, we are going to apply the previous formalism to a pair of quantum dots attached to leads and coupled to each other. We will first introduce a capacitive coupling between the dots and analyse the effect of its strength on the transport properties. This will enable us to derive the stability diagrams of double dots in different coupling regimes. In order to achieve a better treatment we will add a tunnel coupling between the dots and see how this influences the stability diagrams.

2.4.1 Semi classical model

In order to describe the transport properties through a double quantum dot, we make use of an electrical setup inspired of figure 2.2 and extend it to a parallel geometry. A small and a large quantum dot connect through tunnel barriers to two metallic leads each other. These dots are mutually coupled through a tunnel barrier too. The potential of each quantum dot can be varied with plunger gates that couple capacitively to the dots. The mentioned circuit is depicted on figure 2.8.
We only consider for the moment the electrostatic energy of the system and forget about the influence of the quantum states [41]. First we only treat the mutual coupling as purely capacitive. We assume to be in the linear transport regime (vanishing V_{bias}) and work at zero temperature. If cross capacitances and stray capacitances are negligible, the double dot electrostatic energy reads :

$$\begin{aligned} U(N_d, N_D) &= \frac{1}{2}E_d(N_d+\nu_d)^2 + \frac{1}{2}E_D(N_D+\nu_D)^2 \\ &\quad + E_{dD}(N_d+\nu_d)(N_D+\nu_D) \end{aligned} \tag{2.18}$$

The indexes d and D stand for small dot and big dot respectively. N represents a number of electrons in a given dot. $\nu_{d(D)}$ stand for $-\frac{1}{|e|}C_{gd(D)}V_{gd(D)}$. E_d, E_D and E_{dD} correspond to the charging energies of the small dot, the big dot and the mutual charging energy between the dots. The coupling E_{dD} is the change in energy of one dot when an electron is added to the

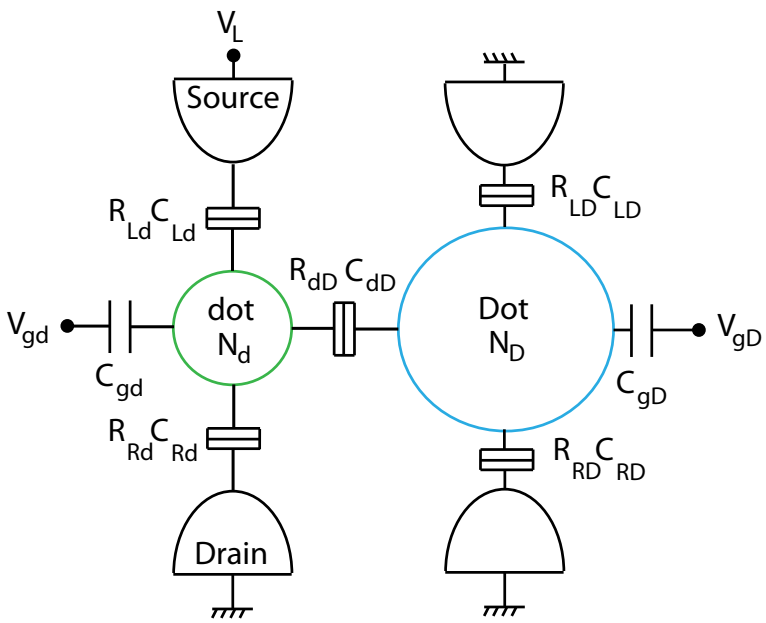

Figure 2.8: Electrical scheme of a double quantum dot arranged in a parallel geometry.

other dot. The different charging energies can be expressed in terms of the capacitances as follows:

$$
\begin{aligned}
E_d &= \frac{e^2}{C_d}\left(\frac{1}{1-\frac{C_{dD}^2}{C_d C_D}}\right) \\
E_D &= \frac{e^2}{C_D}\left(\frac{1}{1-\frac{C_{dD}^2}{C_d C_D}}\right) \\
E_{dD} &= \frac{e^2}{C_{dD}}\left(\frac{1}{\frac{C_d C_D}{C_{dD}^2}-1}\right)
\end{aligned}
\tag{2.19}
$$

$C_{d(D)}$ is the sum of all the capacitances attached to the dot d(D) : $C_{d(D)} = C_{Ld(D)} + C_{Rd(D)} + C_{gd(D)} + C_{dD}$. We can observe that the capacitive coupling between the dots actually renormalizes the charging energies of the independent dots. The ratio $\frac{C_{dD}}{C_{d(D)}}$ determines the importance of the renormalisation and the different transport regimes.
In the weak coupling regime, i.e. $C_{dD} = 0$, hence $E_{dD} = 0$, equation 2.18 reduces to:

$$
U(N_d, N_D) = \frac{(-N_d|e| + C_{gd}V_{gd})^2}{2C_d} + \frac{(-N_D|e| + C_{gD}V_{gD})^2}{2C_D} \tag{2.20}
$$

Which corresponds to the energy of two independent dots.
In the strong coupling regime, when $\frac{C_{dD}}{C_{d(D)}} \longrightarrow 1$, the electrostatic energy is given by:

$$U(N_d, N_D) = \frac{\Big(-(N_d + N_D)|e| + C_{gd}V_{gd} + C_{gD}V_{gD}\Big)^2}{2(\tilde{C}_d + \tilde{C}_D)} \tag{2.21}$$

This represents the energy of a single dot with $N_d + N_D$ charges and a total capacitance $\tilde{C}_d + \tilde{C}_D$, where $\tilde{C}_{d(D)} = C_{d(D)} - C_{dD}$ is the the total capacitance of dot $d(D)$. Thus a large intra dot capacitance leads to an effective single dot.

These extreme limits are not of great interest in our work. We will be more interested in intermediate regimes where the physics is richer. However tuning double quantum dots with a set of almost ten gates is delicate and has to be done step by step. Knowing these limits enables to define a starting point, the weak coupling regime, from which the intra dot coupling is increased gradually towards the strong coupling limit. This enables us to explore the evolution of the stability diagrams for different gate voltages.

2.4.2 Stability diagrams

To derive the stability diagrams of double quantum dots we focus once again on the electrochemical potentials of the system as in section 2.3.3. We now have to define two electrochemical potentials, one for each dot. The electrochemical potential $\mu_{d(D)}(N_d, N_D)$ of dot $d(D)$ is defined as the energy needed to add the ${N_{d(D)}}^{th}$ electron to dot $d(D)$, while having $N_{D(d)}$ electrons in dot $D(d)$. From equation 2.18 the electrochemical potentials of the two dots are:

$$\begin{aligned}
\mu_d(N_d, N_D) &= U(N_d, N_D) - U(N_d - 1, N_D) \\
&= \Big(N_d - \frac{1}{2}\Big)E_d + N_D E_{dD} \\
&\quad - \frac{1}{|e|}(C_{gd}V_{gd}E_d + C_{gD}V_{gD}E_{dD}), \qquad (2.22) \\
\mu_D(N_d, N_D) &= U(N_d, N_D) - U(N_d, N_D - 1) \\
&= \Big(N_D - \frac{1}{2}\Big)E_D + N_d E_{dD} \\
&\quad - \frac{1}{|e|}(C_{gD}V_{gD}E_D + C_{gd}V_{gd}E_{dD}) \qquad (2.23)
\end{aligned}$$

Then at fixed gate voltages, the changes in the electrochemical potentials when a single electron is added in the system read:

$$\begin{aligned}
\mu_d(N_d+1,N_D)-\mu_d(N_d,N_D) &= E_d \\
\mu_D(N_d,N_D+1)-\mu_d(N_d,N_D) &= E_D \\
\mu_d(N_d,N_D+1)-\mu_d(N_d,N_D) &= \mu_D(N_d+1,N_D)-\mu_D(N_d,N_D) \\
&= E_{dD} \qquad (2.24)
\end{aligned}$$

As in the case of a single dot, we have to pay a certain addition energy in order to add an extra electron in the system. For an electron added in dot $d(D)$ this energy simply corresponds to the addition energy $E_{d(D)}$. The change in energy when one of the dots is charged, is felt by the other dot through the mutual capacitance, therefore its electrochemical potential is raised by E_{dD}. So far we only considered the electrostatic part of the energy. From the work made on single dots, we know that the addition energy is a composition between the charging energy and the level spacing. To take into account the quantized states of the dots we take advantage of the fact that in the constant interaction model : $\mu_{i,n} = \mu_i{}^{class} + E_n$. This leads to :

$$\begin{aligned}
\mu_d(N_d+1,N_D)-\mu_d(N_d,N_D) &= E_d+\Delta_d E \\
\mu_D(N_d,N_D+1)-\mu_D(N_d,N_D) &= E_D+\Delta_D E \qquad (2.25)
\end{aligned}$$

Where E_d and E_D corresponds to the addition energies of dot d and D given by equations 2.19. $\Delta_d E$ and $\Delta_D E$ stand for the level spacings of dot d and D respectively. From equations 2.23, the charge stability diagrams of double quantum dots can be derived with the convention that E_d and E_D are now the generalized addition energies that consist of the sum of the electrostatic contribution (2.19) and the orbital contribution (level spacings $\Delta_d E$ and $\Delta_D E$).
We fix the electrochemical potentials of the leads (μ_{Ld}, μ_{Rd}, μ_{LD} and μ_{RD}) at zero and construct a charge stability diagram, giving the numbers N_d and N_D of electrons as a function of V_{gd} and V_{gD} at the equilibrium. Since the potentials of the leads are zero, the equilibrium charges will be given by the largest values of N_d and N_D for which both $\mu_d(N_d,N_D)$ and $\mu_D(N_d,N_D)$ are less than zero. For values larger than zero, electrons escape to the leads. When a set of two couples of numbers (N_d,N_D) is allowed, a charge degeneracy line is found in the stability diagram. Different lines can be obtained from equations 2.23, for a given intra dot coupling constant. We can derive three main type of diagrams corresponding to three main coupling regimes : weak coupling, intermediate coupling and strong coupling [42] [43]. These diagrams are shown in figure 2.9.

Weak coupling limit (Fig 2.9 a). In this limit the mutual capacitance C_{dD}

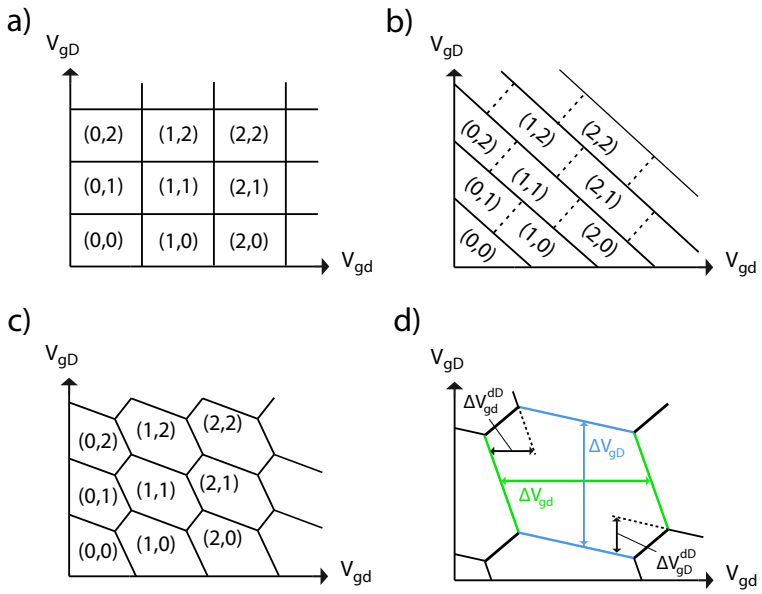

Figure 2.9: Schematic charge stability diagrams of the double dot. The equilibrium charge configurations are denoted (N_d, N_D) and form domains where the charge in the system is well defined. *a)* Weak coupling or vanishing C_{dD}. *b)* Strong coupling, $\frac{C_{dD}}{C_{d(D)}} \rightarrow 1$. *c)* Intermediate coupling with the formation of honeycomb diagrams. *d)* Close view of a honeycomb cell. The different sizes of the cell are directly related to the different energy scales of the coupled dots.

vanishes to zero. In the (V_{gd}, V_{gD}) space, the charge stability diagram is formed of parallelipipedic domains in which the device is blocked. In each domain one can define the charge configuration (N_d, N_D) of the double dot. The sizes of a parallelipided in the V_{gd} and V_{gD} directions are directly related to the addition energies of dot d and dot D respectively and follow a relation given by formula 2.11. Note that no cross capacitance have been assumed, therefore there is no influence of the plunger gate $d(D)$ on the charge configuration of dot $D(d)$. The quantum dots are completely independent.

Strong coupling limit (Fig 2.9 b). When the mutual capacitance becomes of the order of the total capacitances of the two dots, i.e. $\frac{C_{dD}}{C_{d(D)}} \rightarrow 1$, diagonal stripes define the stable charge configuration of the system. In each stripe the total number of electrons in the double dot is fixed. In such a regime it is more relevant to speak about the total number of electrons $N = N_d + N_D$ rather than the N_d and N_D separately. The double dot can simply be thought as a single large dot with two plunger gates, giving therefore coulomb peaks moving along a diagonal lines in the (V_{gd}, V_{gD}) space.

The distance separating two consecutive lines in the V_{gd} and V_{gD} directions is directly related to the addition energy of the total system (Eq. 2.11) . Generally speaking, the arm leavers of each plunger gate are not equal.

Intermediate coupling (Fig 2.9 c). When the capacitive coupling between the dots takes an intermediate value, honeycomb cells form domains in the stability diagram where the charge configuration is fixed. Starting from figure 2.9 a, when the coupling is increased, two main effects appear. First, the parallelipipedic domains get distorted because of the influence of the potential of one dot on the other. The second point is, when a quadruple point (4 charge configurations degenerated) appeared in the weak coupling diagram corresponding to $U_{dD} \to 0$ (Fig 2.9 a), we now find in the intermediate regime two triple points separated by an extra degeneracy line[6]. The reason is the following. The existence of a quadruple point in the honeycomb diagram would allow to add or remove two electrons (one in each dot) in the system at the same time. However the raise/drop ($\pm E_{d(D)}$) of the electrochemical potential of one dot when one electron is added/removed, is followed by a raise/drop ($\pm E_{dD}$) of the electrochemical potential of the other dot. Therefore two electrons cannot be added/removed at the same time. One has to compensate the shift E_{dD} of the electrochemical potential of the other dot to add/remove the second electron. The mutual capacitive coupling then opens a gap between the triple points (Fig. 2.9 c, ΔV_{gd}^{dD}, ΔV_{gD}^{dD}) which is seen via the degeneracy line separating the triple points. At the exact center of the gap, the double dot system is blocked by the mutual charging energy. This remark will be a key point in the understanding of experimental data in a particular regime that will be addressed in the last chapter.
The different dimensions of a honeycomb cell can be related to the addition energies of the coupled dots from :

$$\mu_d(N_d, N_D; V_{gd}, V_{gD}) = \mu_d(N_d + 1, N_D; V_{gd} + \Delta V_{gd}, V_{gD}) \tag{2.26}$$

We then obtain:

$$\Delta V_{gd} = \frac{1}{e\alpha_{gd}} E_d = \frac{1}{e\alpha_{gd}} \left(\frac{e^2}{C_d} + \Delta E_d \right) \tag{2.27}$$

Similarly,

$$\Delta V_{gD} = \frac{1}{e\alpha_{gD}} \left(\frac{e^2}{C_D} + \Delta E_D \right) \tag{2.28}$$

And from:

$$\mu_d(N_d, N_D; V_{gd}, V_{gD}) = \mu_d(N_d, N_D + 1; V_{gd} + \Delta V_{gd}^{dD}, V_{gD}) \tag{2.29}$$

[6] As an example we can see that there is no degeneracy point between the (0,0) and (1,1) domain in the intermediate regime

We derive:

$$\Delta V_{gd}^{dD} = \frac{{C_{dD}}^2}{eC_{gd}C_D} E_{dD} \tag{2.30}$$

Similarly,

$$\Delta V_{gD}^{dD} = \frac{{C_{dD}}^2}{eC_{gD}C_d} E_{dD} \tag{2.31}$$

A close up view on a honeycomb cell (Fig 2.9 d) shows the different dimensions in the (V_{gd},V_{gD}) diagram that have been derived in the previous equations [44] .

In order to test the double dot model, we are now going to compare it with experimental data. These data have been taken in an intermediate intra dot coupling and weak coupling to the leads. We now make an important remark about the experimental setup. The setup that we will use in all our experiments is not exactly the parallel geometry depicted in figure 2.8. We actually tune the dot to achieve a "T shape" geometry, a simpler form of the parallel geometry.

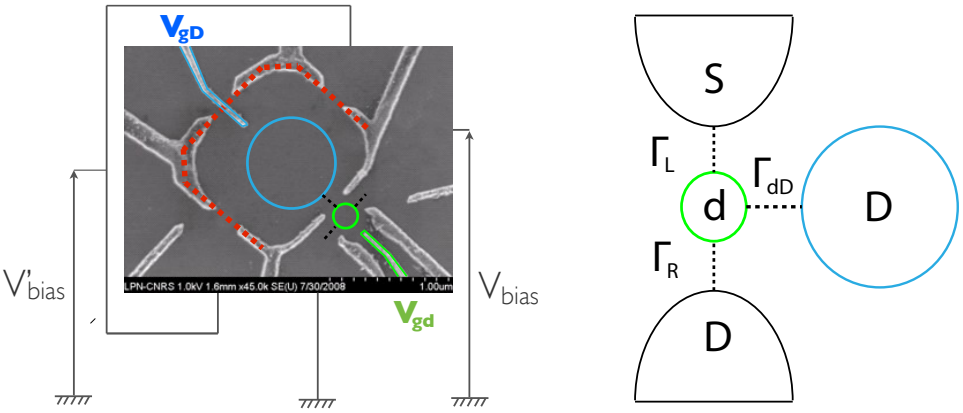

Figure 2.10: *Top panel.* Sem picture of a typical double quantum dot used during this project. The gates connecting the large dot (blue) to its nearest electronic reservoirs are superimposed with a red dashed line. This line indicates the tunnel barriers are close, i.e. far in the pinch off. The plunger gates of each dot have been highlighted with colours for clarity. The bias voltages attached to the different leads will be addressed in the next chapter.*Bottom panel.* Equivalent scheme of the double dot tuned as mentioned. The circuit forms a "T shape" where only the small dot is probed in transport.

By a "T shape" we mean only one dot, the small one, connects to two leads. The other dot, the big one, will connect to those leads through the first dot. To do so, we always make sure that the tunnel barriers connecting the big dot to leads μ_{LD} and μ_{RD} (Fig. 2.8) are far in the pinch off. That is to say

the voltages applied on these gates are as small (negative) as possible to be sure that the transparencies of the barriers are close to zero. That way the tunnel events through these barriers can be neglected and we can simply forget the metallic leads surrounding the big dot. This is what figure 2.10 shows on the left panel, where a SEM picture of our double dot presents a red dashed line on the gates connecting the big dot to its electronic reservoirs. This line indicates closed barriers. Concerning the bias voltages, we will discuss them in the next chapter when looking at the complete experimental setup. For the moment just assume the equivalence between the left panel and right panels of figure 2.10. In the "T shape" geometry depicted, only the small dot is probed in transport. The physics of the large dot will reflect in the current outcoming from the small one, due to intra dot coupling or hybridisation. We can think of the system as a small dot connected to three leads, one of them having a finite size.
A typical measurement of a honeycomb diagram is presented in figure 2.11. The graphic corresponds to a $\frac{dI}{dV}$ measurement (colours) when the two plunger gates V_{gd} and V_{gD} are scanned. To increase the contrast between the low conductance and high conductance areas, we have plotted the logarithm of the differential conductance. This measurement has been performed at low temperature, 20 mK, low bias, $2\mu eV$ and in the weak coupling regime to the leads. Honeycomb cells clearly appear in the stability diagram reflecting an intermediate capacitive coupling between the dots. For clarity, three honeycomb cells have been super imposed on the diagram. Each cell is composed of three main degeneracy lines which correspond to specific transport processes through the double dots.

Fig. 2.11 (1), $(n, N) \longrightarrow (n-1, N)$: Transport occurs through the small dot via resonant tunnelling, while the big dot is in the blockade regime.

Fig. 2.11 (2) $(n, N) \longrightarrow (n-1, N+1)$: No signal is detected on this particular line. We see that this line separates two different charge configurations of the double dot and corresponds to an exchange of an electron from one dot to the other. When we sit in the middle of this line, the electrochemical potentials of the dots are degenerated and lie below the Fermi energy of the leads. No transport occurs through the system and the blockade is defined via the mutual charging energy U_{dD}.

Fig. 2.11 (3) $(n, N) \longrightarrow (n, N+1)$: This degeneracy line corresponds to the degeneracy of the electrochemical potential of the big dot and the electrochemical potential of the leads. In the framework of capacitive coupling between the dots, we do not expect to detect conductance on this type of ridge. Indeed, in the T shape geometry we use, the small dot effectively connects to the leads. In order to understand transport on ridges of type (3), we need to go beyond inter-dot capacitive coupling and introduce tunnel

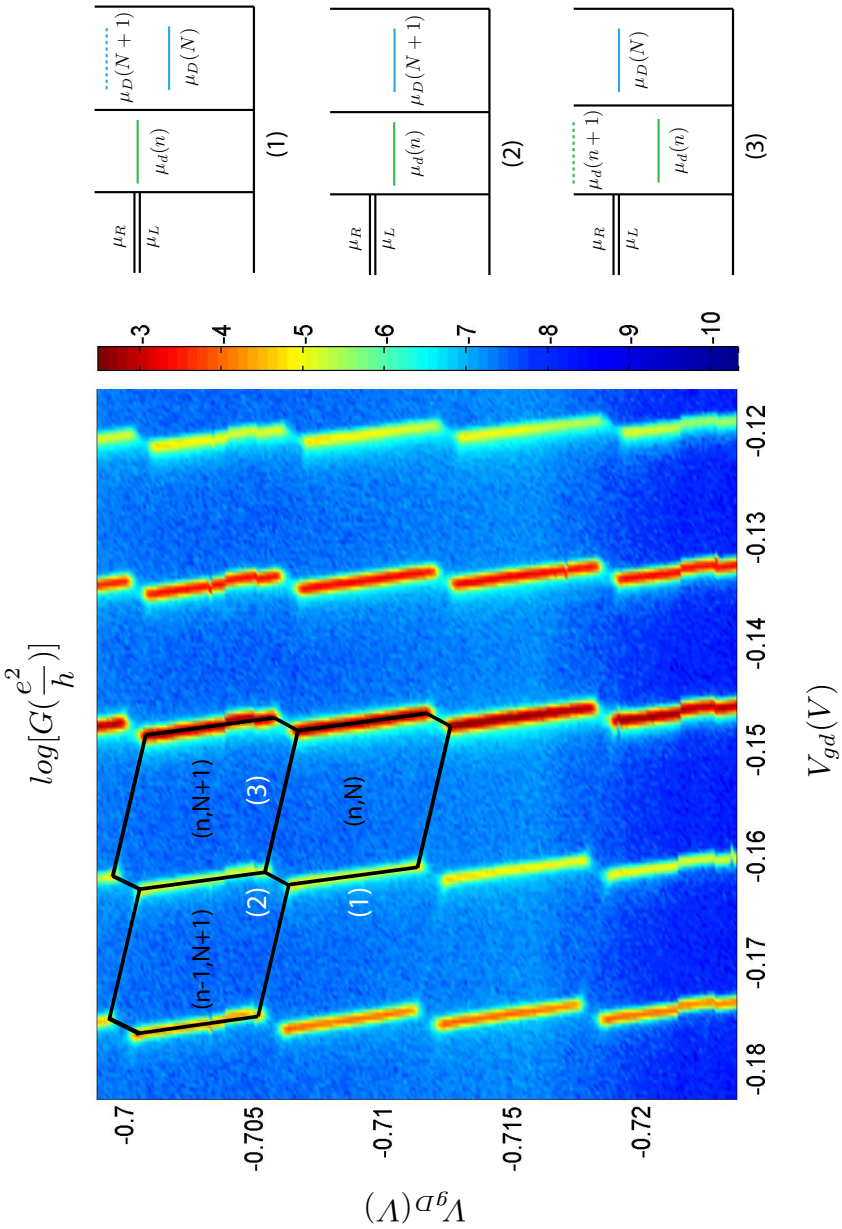

Figure 2.11: Logarithm of the differential conductance monitored when the two plunger gates are scanned. Honeycomb cells appear, reflecting the intradot coupling and the different processes participating to transport through the system. Each honeycomb cell is composed of three main degeneracy lines. They correspond to the degeneracy between the small dot and the leads (1), between the two dots (2) and between the big dot and the leads (3).

coupling (sec 2.4.3). Briefly, inter-dot tunnelling will mix the wave functions of the dots. Therefore, due to the mixing, a certain part of the small dot wave function will remain on ridges of type (3) which will lead to conductance through the device.

At the intersections of the three degeneracy lines, a triple point is formed and corresponds to alignment of all the electrochemical potentials in the double dot-leads system.

2.4.3 Tunnel coupling

When electrons can tunnel coherently from one dot to the other at appreciable rates, the eigenstates become delocalized, extending over the entire double dot system. In principle, these are quantum mechanical many body states of the two coupled dots. It is very difficult to give a full description of such a many body system. For simplicity we discuss here the case of a two level system which as proved to be useful in the understanding of double dots tunnel coupled [45]. Basically, we only take into account the topmost occupied level in each dot and neglect the interaction with electrons in lower energy levels [43]. This simplified picture can be justified as long as transitions occur between the ground states of both dots.
We model the double dot as a two level system described by a Hamiltonian $\mathbf{H}_0$ with eigenstates $|\phi_1>$ and $|\phi_2>$ and eigenenergies E_1 and E_2.

$$\begin{aligned} \mathbf{H}_0|\phi_1> &= E_1|\phi_1> \\ \mathbf{H}_0|\phi_2> &= E_2|\phi_2> \end{aligned} \tag{2.32}$$

We now introduce a tunnel coupling between the two dots described by an Hermitian matrix $\mathbf{T}$ taking the following form:

$$\mathbf{T} = \begin{bmatrix} 0 & t_{12} \\ t_{21} & 0 \end{bmatrix}$$

The system is now described by a new Hamiltonian $\mathbf{H}$=$\mathbf{H}_0$+ $\mathbf{T}$. The new eigenstates $|B>$ (Bonding state) and $|A>$ (antibonding states) correspond to delocalized states. The new eigenenergies can be expressed in terms of the eigenvalues of the uncoupled double dot and the tunnel matrix elements as follows:

$$\begin{aligned} E_B &= E_M - \sqrt{\frac{1}{4}(\Delta E)^2 + |t_{12}|^2} \\ E_A &= E_M + \sqrt{\frac{1}{4}(\Delta E)^2 + |t_{12}|^2} \end{aligned} \tag{2.33}$$

where $E_M = \frac{1}{2}(E_1 + E_2)$, $\Delta E = E_1 - E_2$ and $|t_{12}| = |t_{21}|$.
For a fix tunnel coupling, we see that E_B and E_A describe hyperbolas as

a function of the detuning parameter ΔE. Figure 2.12 (panel c) shows the deviation of the energy levels of the coupled dots from the energy levels of the uncoupled dots when the detuning parameter is varied. We see that the effect of the tunnelling is maximal when $\Delta E = 0$. At this point, the energy levels present an anti crossing that stabilizes the bonding state.
Beyond the renormalization of the energy levels of the system as pointed out by the anti crossing, the tunnel coupling induces another important effect that will influence conductance through our double dots : the mixing of the wave functions of the isolated states. To emphasize this point we write down the molecular eigenstates of the system (Eq. 2.34), that corresponds to a superposition of the isolated states $\mid \varphi_1 >$ and $\mid \varphi_2 >$:

$$\begin{aligned} \mid A > &= cos\frac{\vartheta}{2} \mid \varphi_1 > + sin\frac{\vartheta}{2} \mid \varphi_2 > \\ \mid B > &= -sin\frac{\vartheta}{2} \mid \varphi_1 > + cos\frac{\vartheta}{2} \mid \varphi_2 > \end{aligned} \tag{2.34}$$

$\mid A >$ and $\mid B >$ refer to anti bonding and bonding molecular states. $tg\vartheta = \frac{2t_{12}}{\epsilon_1 - \epsilon_2}$ defines the mixing between the wave functions and therefore determines the weights of each wave function in a given molecular state. As we can see, the proportion of $\mid \varphi_1 >$ and $\mid \varphi_2 >$ in the molecular states will vary as a function of the detuning parameter $\delta = \epsilon_2 - \epsilon_1$. We will go from molecular states very close to a pure isolated states for large detuning compared to the tunnelling element, $\delta >> t_{12}$, to equally mixed states for vanishing detuning, $\delta = 0$.

In order to test the two level description we made above we show in figure 2.12 (panel b) a stability diagram monitored in our double dot at low temperature, 20 mK. Compared to figure 2.11, we have simply depolarized the middle gates separating both dots which increases the inter dot tunnel coupling. We see in figure 2.12 (panel b) that the diagram is very close to a pure honeycomb diagram with corrections near the triple points that smooth the degeneracy lines of the system. One can observe that the profile of these molecular lines follows a hyperbola around the triple points (where the dots levels are degenerated), in agreement with (Eq. 2.33). Note that the contribution of the anti bonding state is not seen in the diagram. At low temperature and low bias, $k_B T, eV << t_{12}$, the anti bonding state is a high energy excited state that is not visited during resonant tunnelling with the leads.
Moreover, from the mixing of the wave functions that varies with the detuning parameter as stipulated by equation 2.34, we can also apprehend the modulation of the conductance on a molecular degeneracy line. As an example we focus on the area around the triple point in figure 2.12 indicated by the black arrow. At the triple point the small dot and large dot levels (electrochemical potentials) are degenerated, $\delta = 0$. Due to tunnel coupling

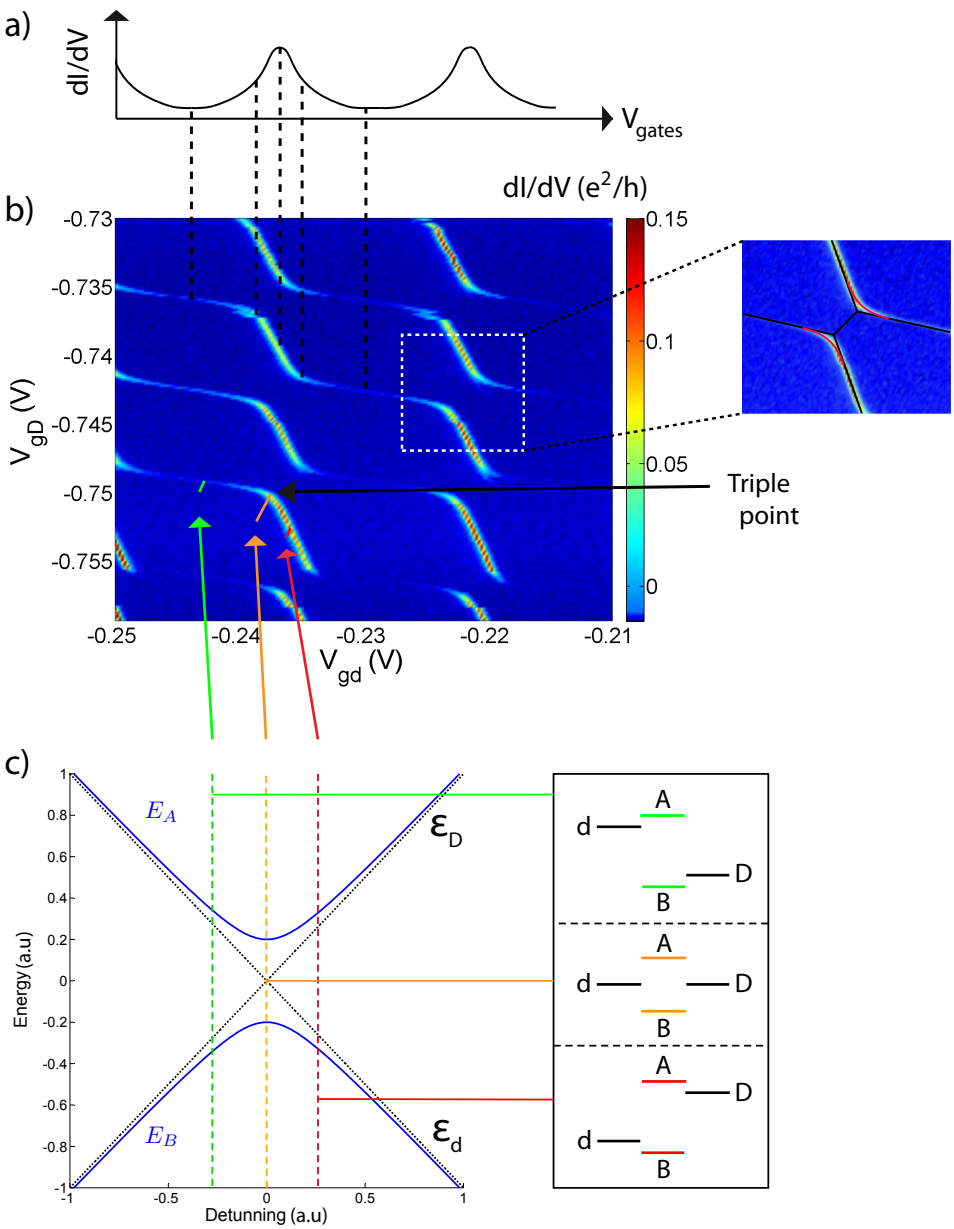

Figure 2.12: *Panel a).* Representation of the modulation of the differential conductance along a molecular degeneracy line. *Panel b)* Honeycomb diagram at low temperature and weak couplings (leads, dots). A zoom on two triple points (white dashed box) on the right side shows the effect of tunnelling (red lines) smoothing out the honeycomb structure (black lines). *Panel c)* Anti crossing between a small dot and large dot levels. On the right side a representation of the independent energy levels (d and D) and molecular levels (A and B) is given. The coloured arrows from panel c) to panel b) make the connection between the coloured cuts (dashed lines) and three different positions in the honeycomb diagram : large dot degeneracy line, triple point and small dot degeneracy line, from left to right respectively.

t_{dD}, this leads to an anti crossing as depicted in figure 2.12 (panel b and c). The molecular states $\mid B >$ and $\mid A >$ formed, are renormalized in energy by the tunnel coupling and hold an equal proportion of small dot and large dot wave functions, $\mid \varphi_d >$ and $\mid \varphi_D >$. A two level representation is given on the right side of the bottom panel for clarity. By continuity from the honeycomb lattice to the molecular degeneracy lines we expect the conductance to take an average value around the area pointed by the orange arrow, since 50% of the ground state has weight in the small dot wave function and therefore effectively connects to the leads. For finite detuning around the triple point, we expect the molecular states to be less renormalized and therefore closer to the pure wave functions. For negative detuning, green dashed cut in panel b), we see that the ground state is closer to the large dot level, that is to say holds a small proportion of the wave function of the small dot. We then expect the conductance to be weak near the area pointed by the green arrow. The red dashed cut for positive detuning, leads to a ground state close to the small dot level which means large conductance on the point indicated by the red arrow.
It appears that the previous remarks are in qualitative agreement with the colour plot shown in Figure 2.12 (panel b).
In conclusion for weak tunnel coupling in our device, the entire stability diagram can be understood in the frame of the constant interaction model applied to capacitively coupled dots (honeycomb diagrams) combined to a two level representation that captures the effect of tunnel coupling. As we will see later in the chapter dedicated to the experimental data, this description does not account for transport through our device for stronger inter dot tunnel coupling.

2.5 Cotunnelling

In the prior analysis of single electron tunnelling, we only considered first order transport processes. Transport was dominated by resonant tunnelling only occurring at resonance with the Fermi energy of the leads. Off resonance Coulomb blockade leaded to the suppression of the current. However in the blockade regime, higher order processes may become relevant in the understanding of transport. These higher order processes become increasingly important when the conductance of the tunnel barriers increase towards $\frac{e^2}{h}$, such that quantum fluctuations broaden the energy levels in the dot, allowing more channels for charge transfer. We refer to these transitions as cotunnelling events, because they involve the cooperation of two electrons. The basic idea is to take advantage of the Heisenberg principle from which large energy fluctuations (of the order of the charging energy in a Coulomb valley) can exist on a short time scale. A simple picture would depict an electron entering the dot and occupying a high energy state during a short

time scale, while an other electron already confined would escape from the dot within this time window (Fig. 2.13). Therefore during a short moment, the dot contains one electron in excess normally forbidden because of the addition energy one has to pay within the vicinity of the Coulomb blockade valley. Such a state is refer to as a virtual state. We can identify two types of cotunneling events: elastic [46] [47] and inelastic [48].

Elastic cotunnelling: $eV < \Delta E$. During an elastic cotunnelling event, no energy is transferred to the dot. After the transition, the state of the quantum dot is unchanged. An example of such a process is depicted in figure 2.13 a. An electron from the left lead enters the dot while a lower energy electron confined within the dot escapes to the right lead. The state of the quantum dot after the sequence is conserved. Note that this description is a very simple and common way of imaging cotunnelling events. Obviously the phenomenon is much more complex. However the description of a tunnel event during which an electron at the Fermi energy in the leads enters the dot (containing n electrons) and occupies a (n+1) high energy particle state[7], followed by a tunnel event during which an electron of the (n+1) particle state escapes the dot and occupies a free state at the Fermi energy in the leads, requires a proper mathematical framework which is not the aim sat this stage. The main point here is that such cotunnelling processes dominate transport in the Coulomb blockade valleys at low bias across the dot and which we encounter for via the naïve picture in figure 2.13 a.

Inelastic cotunnelling: $eV \geq \Delta E$. In the case of inelastic cotunnelling events, energy is transferred to the dot. The initial and final states of the dot will be different. To illustrate in a simple way the mechanism at the origin of this process, we make use of the same type of scheme as in the previous paragraph. Figure 2.13 b is an example of inelastic cotunnelling. The main difference here is that the bias voltage across the dot enables the incoming electron to visit an excited state. We already discussed about transport through excited states in the framework of resonant tunnelling (see section 2.3.5). It appears that the condition $eV \geq \Delta E$ required to occupy excited states within the dot can be extended to cotunnelling events. After the sequence depicted in figure 2.13 b, an excess of energy ΔE is left in the dot. Naturally this is not a stable configuration and the extra energy has to be dissipated. The dissipation will be done in the leads when the electron in the excited state will leave the dot during the following cotunnelling event[8]. The typical signature of inelastic cotunnelling is an increase of the current in a Coulomb valley when $eV \geq \Delta E$. This effect has been pointed by $\frac{dI}{dV}$

[7] A n body quantum state.

[8] When an electron of the (n+1)* particle state, corresponding to an excitation of the (n+1) particle state spectrum, will leave the dot during a following cotunnelling event

measurements: an horizontal line present in the Coulomb diamonds shows that the differential conductance increases because the electron has now two "virtual paths" to tunnel through the dot [49] [50].

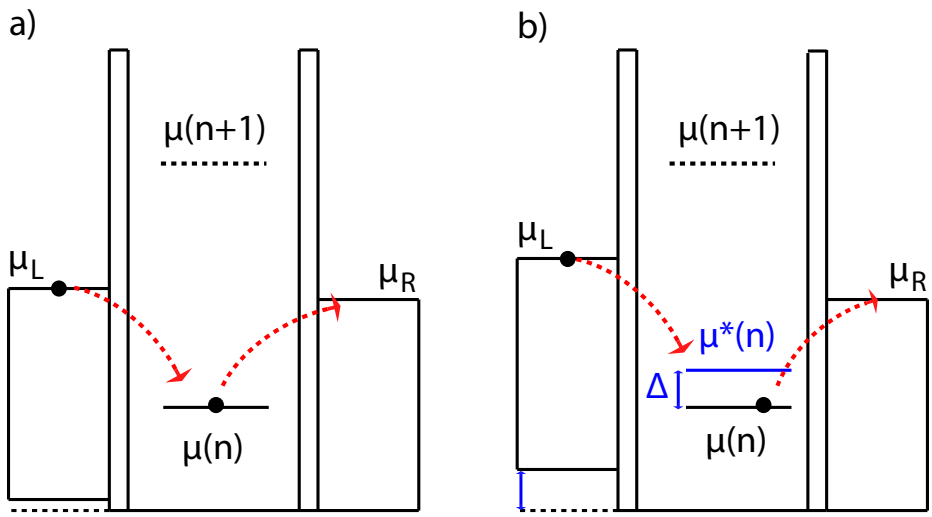

Figure 2.13: *a*: *Elastic cotunnelling*. On a short time scale an electron of the left lead occupies a high energy virtual state. According to Heisenberg principle such energy fluctuations are allowed in a related time window. In this time window a low energy electron escapes from the dot, bringing back the dot in its initial state. *b*: *Inelastic cotunnelling*. When the bias across the dot is large enough, i.e. $eV \geq \Delta E$, the incoming electron can now visit an excited state. When the low energy electron leaves the dot, an energy ΔE (Δ in the figure) has been transferred to the dot. This energy will be dissipated in the leads during the next cotunnelling events.

Note that even though tunnelling into a virtual state does not conserve energy, the entire cotunnelling process does conserve the energy.
We only considered above charge transfers without taking care of other degrees of freedom. Actually other degrees of freedom such as spin can lead to transport processes involving cotunnelling which dominate the low temperature behaviour of quantum dots. This type of physics, earlier discovered in metallic systems containing magnetic impurities, is known as the Kondo effect and has been successfully applied to quantum dots. The latter can be regarded as the result of a coherent superposition of higher order cotunneling events and will be the main focus of this thesis.

2.6 Kondo effect

Before proceeding with a discussion of the features of the Kondo effect in quantum dots, let us first recall the main features of the Kondo effect as

exhibited by dilute magnetic alloys. While it is well known that the suppression of electron-phonon interactions with decreasing temperature leads to the decrease of the resistance of pure metals, experiments performed more than seventy years ago pointed out a change in the sign of the temperature coefficient of the resistance at very low temperature, which then increases with decreasing temperature. This unexpected effect was explained in 1964 by Jun Kondo [51]. The Kondo effect finds its origin in the scattering of the conduction electrons with magnetic impurities trapped in the metal host through an antiferromagnetic exchange interaction. The key advance in the understanding of these scattering processes was the realization that their description requires to go beyond second order perturbation calculations. The reason is the importance of virtual exchange scattering processes, in which the conduction electrons scatter between some initial and final state, via an intermediate virtual state. In such a process their spin is effectively flipped with the magnetic impurity conserving thereby the total spin momentum. Later, Wilson extended Kondo's work using a numerical renormalization group approach [52]. He showed that the resistance due to exchange scattering should saturate in the low temperature limit. In this regime, the localized magnetic moment of the impurity is screened by the spin exchange with the surrounding electrons [53]. Later on the basis of the Anderson model [54], Glazman and Raikh [55] and Ng and Lee [56] predicted that quantum dots should exhibit the Kondo effect.

2.6.1 Anderson Hamiltonian

To describe a local moment we consider a single quantum state E_d. In order to take into account Coulomb interactions, a term U shifts the energy level for double occupancy. Four configurations of the impurity state exist : an empty state at $E = 0$, two single occupied state at E_d (spin degeneracy) and a singlet state at $2E_d + U$. The different configurations are depicted in figure 2.14. The empty and double occupied state are non magnetic whereas the single occupied state present a magnetic moment $S = \frac{1}{2}$. The existences of a stable magnetic moment is the key understanding of the standard Kondo effect.

We now couple this localised d state to electronic reservoirs (Fig. 2.14 4). As in the case of a quantum dot, the localised quantum level connects through tunnel barriers to the metallic reservoirs. The Anderson Hamiltonian of the system describes the d level of the impurity hybridised with the conduction electrons of the leads,

$$\begin{aligned} H &= \sum_{\sigma} \epsilon_d n_{d,\sigma} + U n_{d,\uparrow} n_{d,\downarrow} + \sum_{k,\sigma} \epsilon_k c^{\dagger}_{k,\sigma} c_{k,\sigma} \\ &\quad + \sum_{k,\sigma} (t_k c^{\dagger}_{d,\sigma} c_{k,\sigma} + t^*_k c^{\dagger}_{k,\sigma} c_{d,\sigma}) \end{aligned} \tag{2.35}$$

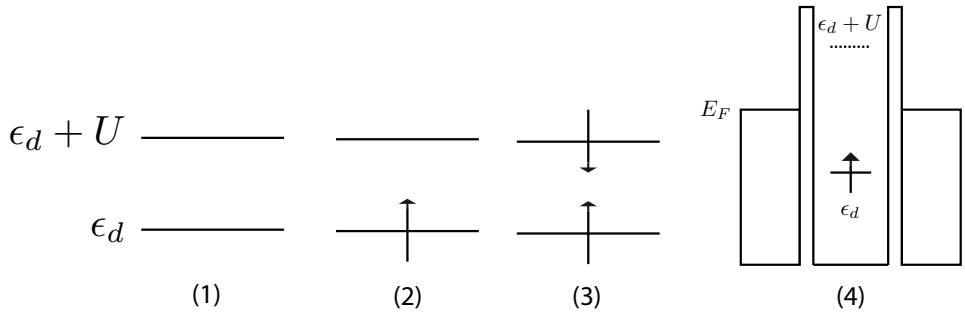

Figure 2.14: Configuration for the impurity state. (1) $E = 0$ no magnetic moment. (2) $E = E_{d,\uparrow(\downarrow)}$ magnetic moment $S = \frac{1}{2}$ (taking into account spin degeneracy leads to two possible states at E_d). (3) $E = 2E_d + U$ no magnetic moment. (4) Localized level coupled to electronic reservoirs. The situation depicted is the local moment regime.

The first term is the energy of the localised level without any interactions. The second term corresponds to the on site Coulomb interaction acting when the d level is double occupied. The third term represents the kinetic energy of the free conduction electrons in the leads. The last term describes the hybridisation between the d level and the k states in the leads via tunnelling (t_k)[9]σ and k stand for the spin component and the wave vector respectively. The simplest case of a non degenerate d orbital which has at most double occupancy with a spin $\uparrow$ and a spin $\downarrow$ electrons is considered. Such an atomic description of a localised quantum level is relatively general and already enabled us to describe transport through quantum dots within the weak coupling limit ($t_k \to 0$) though using a semiclassical approach. In the strong coupling limit we know that cotunnelling events overcome the blockade and have to be taken into account to understand transport through the system. These cotunnelling events happen to be at the origin of the Kondo effect.

2.6.2 Link between the Anderson and the Kondo Hamiltonians

It was shown by Schrieffer and Wolff [57] that such an Hamiltonian (Eq. 2.35) for odd occupancy, case (2) figure 2.14, can be approximated to a Kondo Hamiltonian,

$$H_K = \sum_{k,\sigma} \epsilon_k c^\dagger_{k,\sigma} c_{k,\sigma} - \sum_{k,k'} \frac{J_{k,k'}}{\hbar^2} (\psi^\dagger_{k'} S \psi_k)(\psi^\dagger_{d'} S \psi_d) \tag{2.36}$$

[9]Strictly speaking this term of the Hamiltonian describes a single lead. To account for several leads, the sum should be carried over a additional index accounting for each lead. For symmetric couplings of the d level to each leads, the summation of this last index can be dropped.

$\psi^\dagger_{d'} S \psi_d$ is the spin operator of electrons in the d level of the impurity and the spin operator $\psi^\dagger_{k'} S \psi_k$ is the operator describing the transitions of the free electrons between states k and k'. For an exchange coupling J negative, the interaction is antiferromagnetic and the energy is minimised by forming a singlet between the local moment and the free electrons. The connection between Kondo physics and quantum dots is made when an odd number of electrons confined within the dot act as a single spin coupled to electron reservoirs.
However, it is not obvious that an equivalence between the Anderson Hamiltonian and the Kondo Hamiltonian exists. A schematic cotunnelling mechanism can help to understand the link between these Hamiltonians and why quantum dots undergo the Kondo effect.

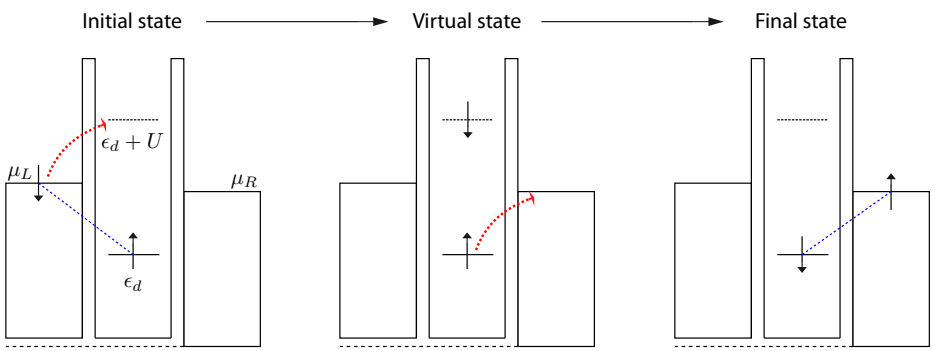

Figure 2.15: Schematic representation of the cotunnelling sequence leading to a spin flip on a quantum dot. The process depicted is an electron process where a high energy singlet is formed in the dot during a short time. An equivalent sequence exists with an empty virtual state if the localized electron tunnels out of the dot before a conduction electron tunnels in. This process is referred to as a hole process.

In figure 2.15, we start from an initial configuration where we consider two spins, one in the leads and one in the dot, with opposite directions. A cotunnelling process allows the electron of the Fermi sea to tunnel into the dot and form a high energy singlet within a short time window, this is the virtual state. An electron wihtin the dot then tunnels out of the dot to occupy an empty state in the continuum of the right lead and the energy of the dot drops back to its initial value. Because each tunnelling event conserves the spin, the result is an effective flip of the spin of the quantum dot. The Schrieffer Wolff transformation incorporates the tunnel events to second order into an effective exchange coupling taking the following form:

$$J_{k,k'} = t_k^* t_{k'} \left(\frac{1}{U + \epsilon_d - \epsilon'_k} + \frac{1}{\epsilon_k - \epsilon_d} \right) \tag{2.37}$$

In the local moment regime, that is to say $U + \epsilon_d > \epsilon_F$ and $\epsilon_d < \epsilon_F$, the effective exchange coupling is negative for scattering of conduction electrons in the region of the Fermi level $\epsilon_k, \epsilon_{k'} \backsim \epsilon_F$. Therefore the interaction term in the Kondo Hamiltonian (Eq. 2.36) is antiferromagnetic.

2.6.3 Notes on perturbation theory

The Schrieffer-Wolff transformation makes a parallel between Hamilonitian 2.35 and 2.36, but does not give the solution to the Kondo problem. As pointed out by Kondo, finding the solution to Hamiltonian 2.36 requires to go beyond usual perturbation theory. In his original paper [51], Kondo showed that in a metal containing diluted magnetic impurities, the spin flip events involving the spin of the free conduction electrons and a localized spin, lead to a correction of the resistance that to third order in J reads:

$$R^{spin}_{impurity} = \frac{3\pi m J^2 S(S+1)}{2e^2\hbar E_F}\left(1 - 4J\rho_0(E_F)\ln\left(\frac{k_B T}{D}\right)\right) \tag{2.38}$$

where m is the electron mass, S the spin of the localized moment, $\rho_0(E_F)$ is the density of states in the metal at the Fermi energy and D the energy bandwidth of the problem. As one observes, the correction to third order gives rise to a $\ln T$ dependence that increases as T decreases for an anti-ferromagnetic coupling J. We can see through this expression the importance of high order spin flips as temperature decreases that strongly renormalize the effective exchange interaction. Actually the more the temperature is lowered and the more higher order corrections to the exchange interaction become important[10]. This feature leads to great difficulties in the derivation of a complete solution to the Kondo problem and was a great challenge in the late 1960s and early 1970s for theoretical physics. If we go back to equation 2.38, the break down of the perturbation calculations performed by Kondo appears when the third order correction becomes of the order of the second order term. In other words when,

$$-J\rho_0(E_F)\ln\left(\frac{k_B T}{D}\right) \simeq 1$$

Which leads to the definition of a very important energy scale of the Kondo effect: the Kondo temperature,

$$k_B T_K \simeq D\ \exp\left(\frac{-1}{\rho_0(E_F)J}\right) \tag{2.39}$$

In order to find a solution to the Kondo problem at all temperatures, non perturbative tools were developed to account for corrections to all orders.

[10]The Kondo effect can be considered as an example of asymptotic freedom, i.e. a situation where the coupling becomes non perturbatively strong at low temperatures and low energies

The understanding of the complete mathematical background related to the Kondo effect are not the aim of this thesis and we will address briefly some points of the non perturbative methods used to treat the problem. The first step was made by Anderson, within the framework of the so called poor man's scaling [58]. The ideas developed in this model can be approached to the Schrieffer-Wolff transformation where the high energy excitations can be absorbed as a renormalization of the coupling J. The underlying philosophy of this method is to realize that only a few features of the high energy physics of the system are relevant to account for its low energy excitations. For an Hamiltonian H(D) parametrized by a high energy cut-off D, the highest one particle excitation[11], the idea is to reduce the cut-off D bit by bit by adjusting the Hamiltonian at each step in order to conserve the low energy dynamics. Within the framework of the Anderson Hamiltonian, he high energy charge fluctuations will be quenched during the scaling and the low energy spin excitations of the system will be revealed.
To carry out the scaling here, the conduction band is divided into states at energy ϵ_k, $-\tilde{D}+\delta \mid D \mid < \epsilon_k < \tilde{D} - \mid \delta D \mid$, which are retained and states within $\mid \delta D \mid$ of the band edge which are to be eliminated provided the effective exchange Hamiltonian ($J\mathbf{S}.s$[12]) is perturbatively renormalized by changing $J \rightarrow \delta J$. From the lowest order corrections to J due to virtual scattering of conduction electrons with energy ϵ in the band edge[13], one can find the expression of δJ,

$$\delta J = -\rho_0 J^2 \frac{\mid \delta D \mid}{D} \tag{2.40}$$

Which leads to the scaling equation,

$$\frac{dJ}{d\ln\big(\rho_0 J\big)} = -\rho_0 J^2 \tag{2.41}$$

Integrating equation 2.41 from the initial band width $\tilde{D}$ and coupling constant J (Schrieffer-Wolff type) to a new band width $\bar{D}$ and renormalized coupling constant $\bar{J}$ yields,

$$\tilde{D}\exp\Big(-\frac{1}{\rho_0 J}\Big) = \bar{D}\exp\Big(-\frac{1}{\rho_0 \bar{J}}\Big) \tag{2.42}$$

Equation 2.42 shows that the solution of the scaling equation 2.41 is characterized by a single parameter which plays the role of a scaling invariant [59]. Comparing equation 2.39 and 2.42 we see that this scaling invariant is the Kondo temperature. This energy scale is the unique energy scale of the

[11] We will see that in the case of quantum dots, the cut-off energy corresponds to the charging energy

[12] Kondo type Hamiltonian

[13] Expressed in terms of Feynamn diagrams

Kondo problem which makes it a universal energy scale. Any system undergoing the Kondo effect is governed by the Kondo temperature and all observables can be expressed in terms of a dimensionless parameters such as T/T_K[14]. Unfortunately the poor man's scaling procedure stops when D becomes of the order of T_K due to new divergences appearing in the renormalized parameters of the low energy Hamiltonian.
The complete scaling procedure is a hard task. In order to find the solution to the Kondo problem on the entire energy range (from $T >> T_K$ to $T << T_K$), the development of the Numerical Renormalization Group (NRG) theory by Wilson was necessary [52]. We will not address features of such complex calculations which are way beyond the range of this thesis. During the renormalization procedure developed by Wilson, the Hamiltonian is not forced to match the Kondo Hamiltonian and is free to evolve. In a very elegant way, the NRG method leads to an effective Anderson Hamiltonian at very low temperature ($T << T_K$) with a strongly reduced Coulomb repulsion term. The reduction is such that a perturbative treatment[15] is possible in order to derive the ground state properties. An important point, earlier conjectured and proved by the NRG is the nature of this ground state as temperature approaches zero. It appears that the localized spin is gradually screened out by the conduction electrons as the temperature is lowered, such that as $T \rightarrow 0$ it behaves effectively as a non-magnetic impurity giving a temperature independent contribution to the resistivity in this regime. This regime is called the unitary limit and the system consists of an N body singlet where the local moment entangles with the spins of the conduction electrons in the metal host.
Interestingly, where the Kondo effect gives rise to a raise of the resistivity in metals containing diluted magnetic impurities, it was proven that in quantum dots the result of the Kondo effect is an equivalent raise (same temperature scaling) of the conductance through it [54] [55]Ng and Lee [56]. This point will be discussed in more details when presenting the Kondo resonance. Briefly, the establishment of a Kondo state at low temperature ($T << T_K$) between the reservoirs and the quantum dot will enable to create a channel (pinned at the Fermi energy) for conductance in the vicinity of a Coulomb blockade valley corresponding to an odd filling of the dot (spin 1/2 impurity).

2.6.4 Kondo temperature

As mentioned, the Kondo effect is governed by a single energy scale called the Kondo temperature, T_K, that in a sense defines the binding energy of the singlet state formed at low temperature. The expression of the Kondo

[14] Generally speaking the ratio between an external energy and the Kondo temperature $k_B T_K$

[15] U can be treated as a perturbation

temperature in the framework of the Kondo Hamitonian 2.36 reads with the proper pre-factors:

$$T_K \simeq D\sqrt{\rho J}\exp\left(-\frac{1}{\rho J}\right) \tag{2.43}$$

where ρ_0 as been written ρ for simplicity. Interestingly Haldane [60] showed later that the Kondo temperature could be expressed in terms of the Anderson model parameters as:

$$T_K \simeq \frac{\sqrt{\Gamma U}}{2}\exp\left(\frac{\pi\epsilon(\epsilon+U)}{\Gamma U}\right) \tag{2.44}$$

with $\Gamma \sim \rho t^{216}$ being the effective coupling of the localized level with the leads, U the addition energy and ϵ the detuning parameter measuring the position of the localized level relative to the Fermi energy of the leads. All the parameters of the Anderson model collapse into a single energy scale, confirming that in the Kondo regime the Kondo temperature becomes the unique relevant energy scale of the system. Note that this expression of the Kondo temperature is widely used in the context of quantum dots. Any external excitation ($E_{external} = k_B T, eV, \mu_B B, ...$) can be compared to the Kondo temperature in order to identify the regime the system sits in.

- At low energy, that is to say $T_K >> E_{external}$, the system is in the low temperature limit also called the unitary limit. The local moment is screened by the surrounding electrons forming a N body non magnetic state. Is this regime, Nozières [61] showed that the system behaves as a Fermi liquid. The conductance can be expressed [62],

  $$G(V=0,T) = G_0\left(1-\left(\frac{\pi T}{T_K}\right)^2\right) \tag{2.45}$$

  The external perturbation in this equation is a thermal perturbation. As mentioned previously this perturbation can be of other origin such as magnetic field for example. The ratio T/T_K denotes the ratio of two energies competing together.

- At high energy, $T_K << E_{external}$, the Kondo coupling can be treated as a perturbation. The impurity acts as a diffusion center as proved by weak localisation measurements in metallic nanowires [63]. Logarithmic corrections are found in the conductance that follows a law [62],

  $$G \simeq G_0\frac{1}{\ln^2\left(T/T_K\right)} \tag{2.46}$$

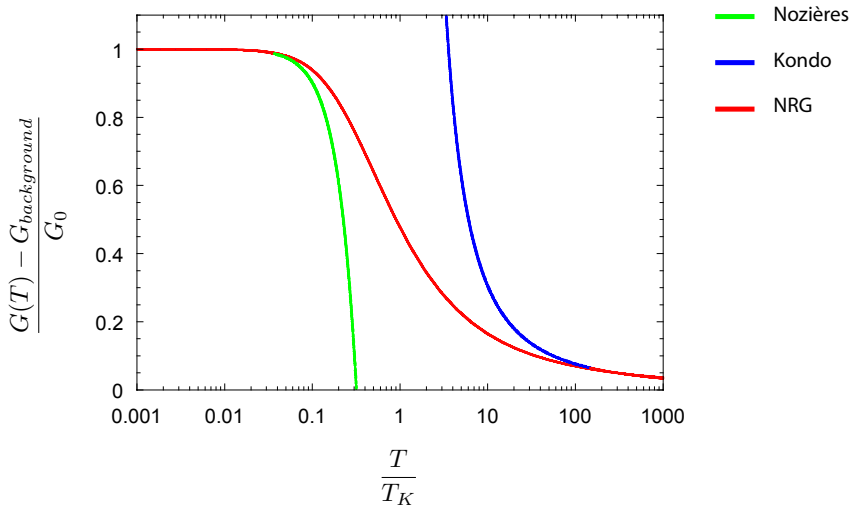

Figure 2.16: Evolution of the renormalised conductance versus renormalised temperature in the Kondo regime. The red curve corresponds the universal function f obtained using numerical renormalization group calculations. For comparison the low temperature and high temperature limits as obtained by Nozières and Kondo respectively have been added.

However the link between the low and high temperature limits cannot be expressed with an exact analytical formula. The solution was given Numerical Renormalization Group calculations [64]. This numerical approach enables to compute and extract the whole temperature dependence of the conductance (Fig. 2.16),

$$\frac{G(T) - G_{background}}{G_0} = f(T/T_K) \tag{2.47}$$

$G_{background}$ and G_0 are parameters that are sample dependent as we will see. The crucial point is that the numerical function f is a universal function that does not depend on the system under study but only on the Kondo temperature and the value of the spin of the impurity.

2.6.5 Kondo resonance

The Kondo effect causes a distinctive modification of the density of states of the system impurity+electronic reservoirs. This point is of great importance in tunnelling experiments since the intensity of the current is linked to the local density of states. We have to understand this modification to apprehend transport experiments performed in quantum dots in the Kondo regime.

[16] t represents the tunnel coupling of the impurity to the reservoirs.

A simple two level system can enable to capture the basis of this modification. We consider a two level system composed of a non interacting level spin degenerated simulating an electronic reservoir at the Fermi energy. A localized level detuned from the Fermi energy at $\epsilon_d < E_F$ is then coupled to the first level via a tunnelling element t. This localized level has an on site Coulomb repulsion energy U pushing the double occupied localized state to high energy (Fig 2.17). This model is a non degenerate Anderson model

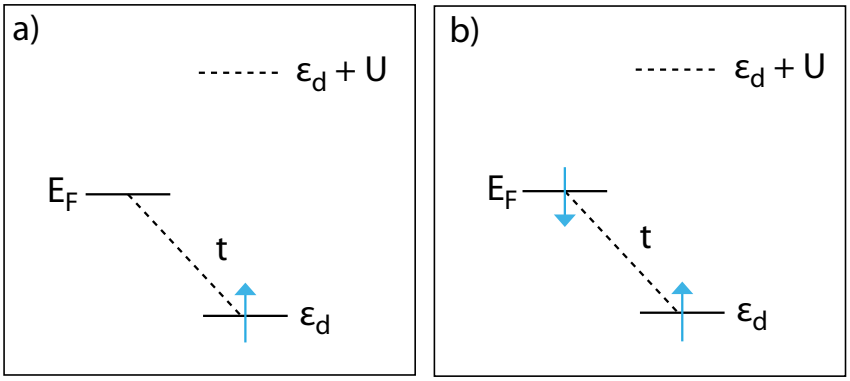

Figure 2.17: *a)*. Ground state of two level system with a non interacting level at E_F and localized level at ϵ_d with on site repulsion (U) when the system contains a single electron. textitb). Ground state of the system when it contains two electrons. A singlet delocalized between the localized d level and the non interacting level is formed. Note that the tunnel coupling t is supposed to be weak compared to the other energy scales.

with a single conduction band state at E_F. The Hamiltonian of the system is the Anderson Hamiltonian presented before (Eq. 2.35) where all the sums over the k index have been dropped. For our purpose it is enough to consider states with only one or two electrons. For an impurity state well below the Fermi energy we have $t << E_F - \epsilon_d$. In this limit the one electron eigenstates differ weakly from the uncoupled states and can be expressed as[17]:

$$E_+ = \epsilon_d - \frac{t^2}{E_F - \epsilon_d}, \qquad E_- = E_F + \frac{t^2}{E_F - \epsilon_d} \tag{2.48}$$

We see that the ground state is E_+ and differs from ϵ_d of a correction factor $\frac{t^2}{E_F - \epsilon_d}$ small in the limit we are considering.
The two electron states can be classified as singlets or triplets. For large on site Coulomb repulsion, the states in which the impurity is predominantly doubly occupied are pushed to very high energy, $2\epsilon_D + U$, and can be forgotten at low energy. We can also neglect the states in which the non interacting level is predominantly doubly occupied since they are also

[17] A Taylor expansion of equation 2.33 for $t_{12} << \Delta E$ leads to this result

high energy states ($\simeq 2E_F$). The ground state will be a state in which the two electrons are shared between the non interacting and localized levels. Taking into account the spin, two states are possible, a triplet state and a singlet state. One can show that the eigenenergies of these states are [59],

$$\begin{aligned} E_T &= \epsilon_d + E_F \\ E_S &= \epsilon_d + E_F - \frac{2t^2}{E_F - \epsilon_d} \end{aligned} \tag{2.49}$$

The ground state when the system contains two electrons is a singlet state formed between the non interacting level at E_F and the localized d level (Fig. 2.17, b). The singlet state is more stable than the triplet state due to hybridisation(Eq. 2.49). The reduction factor stands as $\frac{2t^2}{E_F-\epsilon_d}$ which can be associated to the energy gain $2J$ in the Kondo Hamiltonian with J being given by the Schieffer- Wolff transformation in the limit $U \to \infty$.

We consider now the excitations of two particle system. We consider an excitation in which an electron is removed from the ground state at E_S. Two possible final states exist : the state at E_- and the state at E_+ being the lowest energy state (Eq. 2.48). One can calculate the energy of both transitions:

$$E_S - E_+ = E_F - \frac{t^2}{E_F - \epsilon_d} \tag{2.50}$$

which corresponds to an excitation energy just below the Fermi energy. And,

$$E_S - E_- = \epsilon_d - \frac{3t^2}{E_F - \epsilon_d} \tag{2.51}$$

which corresponds to an excitation energy well below the Fermi and close to ϵ_d. Based on their respective energy cost, we see that the last transition (Eq. 2.51) is the most probable. Nevertheless the fact that the transitions shown in equation 2.50 carry some weight is of importance in the understanding of the Kondo effect. A comparable treatment for the addition of an electron to the singlet shows transitions with spectral weight situated just above the Fermi energy (particle-hole symmetry). These transitions around the Fermi energy are the keystone of transport in the Kondo regime as we are about to see. For a more detailed analysis of this two level system and for the complete treatment of the Kondo effect in the framework of the Anderson Hamiltonian (Eq. 2.35) we refer the reader to [59]. The complete calculation shows that the singlet binding energy increases from $2J$ to k_BT_K. The spectral weight around the Fermi energy develops into the Kondo resonance with a FWHM k_BT_K in the unitary limit and centred at E_F.
The resonant state (Fig. 2.18) sensed in the simplified Anderson model and confirmed by renormalization calculation in the Anderson model is an essential point in transport experiments performed in the Kondo regime as

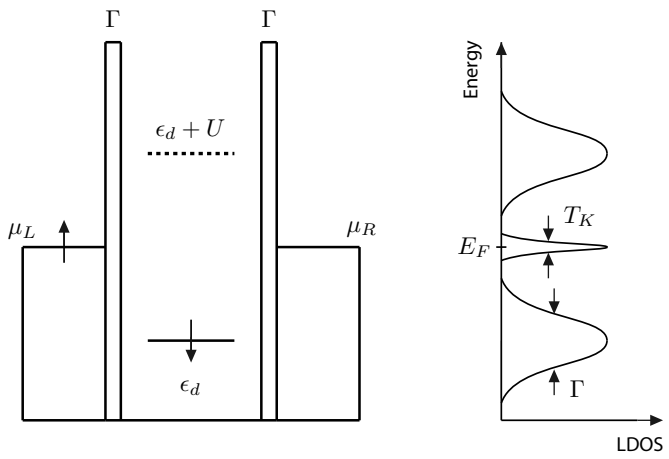

Figure 2.18: *Left panel.* Schematic representation of the singlet formed at low temperature between the impurity and the free electrons in the leads. *Right panel.* Plot of the energy versus the local density of states of the system. A kondo resonance locked at the Fermi energy develops in the low temperature regime of the Kondo effect which opens an extra channel through the device.

mentioned. The existence of a Kondo resonance at the Fermi energy in the unitary limit illustrates the fact that a virtual resonant state is created at low temperature. Even though the impurity or quantum dot is blocked, the Kondo effect reestablishes conductance via this extra channel and can reach $\frac{2e^2}{h}$ for symmetric tunnel barriers. This is valid at low temperature when the Kondo singlet is well formed. In the high temperature limit the singlet is gradually destroyed as well as the resonant state. Conductance drops following the universal law mentionend previously (Fig. 2.16).
The main signatures of the Kondo effect in quantum dots are :

- The enhanced conductance in the odd valleys (local moment regime) of the Coulomb blockade at low energy (eV, k_BT, $g\mu_B B << k_BT_K$)

- The existence of a Kondo resonance at low energy accessible via non linear measurements and referred to as a zero bias anomaly since it is locked at the Fermi energy of the leads (the zero bias). One can give a simple explanation of the presence of a ZBA in the Kondo regime. The Kondo temperature defines the binding energy of the N body singlet formed between the localized state and the leads. IN the vicinity of a Kondo valley, when a bias voltage of the order of this energy scales is applied, $\mid eV \mid \sim k_BT_K$, the Kondo singlet is broken and the mechanism leading to transport through the device is destroyed. As a result a peak of width of the order of T_K is seen in the dI/dV_{bias} vs V_{bias} characteristic curve. Another way to apprehend the

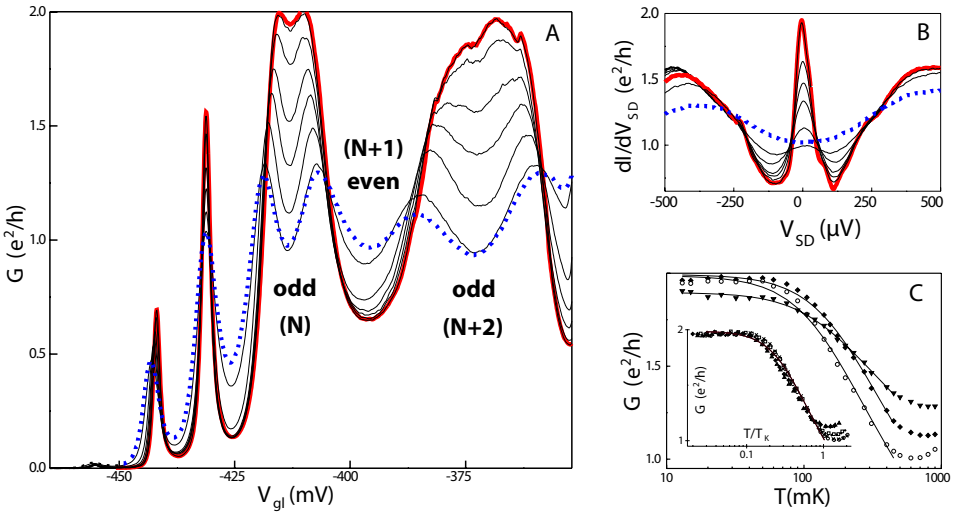

Figure 2.19:

ZBA stands in the fact that at zero bias the virtual processes leading to the Kondo mechanism involve free electrons at the same energy in both leads. When the bias voltage is raised, these mechanism do not occur at the same energy any more and the coherence of the process is lost. Consequently, the Kondo mechanism is quenched, therefore the conductance decreases.

- The evolution of the conductance in the odd valleys follows a universal function when an external perturbation such as temperature is applied to the system.

These different points are illustrated in figure 2.19. These data are extracted from work made by van der Wiel et al. [65]. The experiments were performed in the Quantum Transport department leaded by Leo Kouwenhoven of Delft University of Technology.

Figure 2.19 A shows a series of Coulomb peaks when the plunger gate of a single quantum dot is scanned. At low temperature (red line, 15 mK) the Coulomb blockade peaks sequence exhibits a parity effect with one minima over two increasing with decreasing temperature. The interpretation of this effect is clear in the Kondo regime. For odd occupancy, the dot acts as a magnetic impurity and undergoes the Kondo effect. The Coulomb blockade is lifted with the formation of the Kondo singlet and conductance reaches the quantum of conductance in the odd valleys. For even occupancy, the dot is none magnetic. It cannot enter the Kondo regime in that case and conductance decreases in the even valleys.

Figure 2.19 B is a non linear transport where the bias voltage across the quantum dot is scanned when the dot is in the Kondo regime (odd valley). At low temperature (red line) a narrow peak in the local density of states (dI/dV) is observed. This is the Zero Bias Anomaly (ZBA) illustrating the formation of a Kondo resonance at low energies. Notice this peak is centered at zero bias, that is to say at the Fermi energy of the leads. At high temperature the ZBA is lost, the Kondo cloud is destroyed as well as the Kondo resonance.

Figure 2.19 C shows the evolution of the conductance in a Coulomb blockade valley undergoing the Kondo effect in agreement with the NRG calculations. A scaling of the renormalized conductance (G/G_0) versus renormalized temperature (T/T_K) shows the universal character of the Kondo effect when the dot is in the Kondo regime.

Chapter 3

Experimental setup

The energy scales of the physics probed in lateral quantum dots set the experimental constraints. Low temperature measurements, typically below 100 mK and low noise electronics are required in order to investigate lateral quantum dots. This chapter is dedicated to the presentation of the cryogenics techniques used to cool the samples down to 20 mK and to the electronics developed in the Neel Institut to perform transport measurements at low temperature.

3.1 Dilution refrigerator

3.1.1 Principle

The dilution refrigerator is the work-horse of low temperature physics. This device is the most widely used in laboratories to work at temperatures below 100 mK. It presents the advantages to work in closed cycle, that is to say the capability to stay cold without any time limit, and without creating any electromagnetic field (to the extent of the pumps).
The main idea, proposed originally by London, Clarke and Mendoza [66], stands on the thermodynamic properties of $^3He - ^4He$ mixtures. If you lower the temperature of any solution of more than 6% ^3He sufficiently, the mixture will separate into two phases. One of these phases will (at very low temperatures) be almost pure ^3He. The other phase will be mostly pure ^4He, but even at $T = 0$, will contain a fraction of 6% ^3He impurity. This property is the key of the operation of dilution refrigerators.
If we consider a "mixing chamber" (Fig. 3.1, mixing chamber) holding a solution of $^3He - ^4He$, at low temperature the light phase rich in ^3He atoms will float on top of the heavy phase poor in ^3He atoms. At the boundary of the two species, an effective liquid-vapor interface of ^3He develops below 0.7 K. Note that this is a common representation to think of the rich ^3He phase

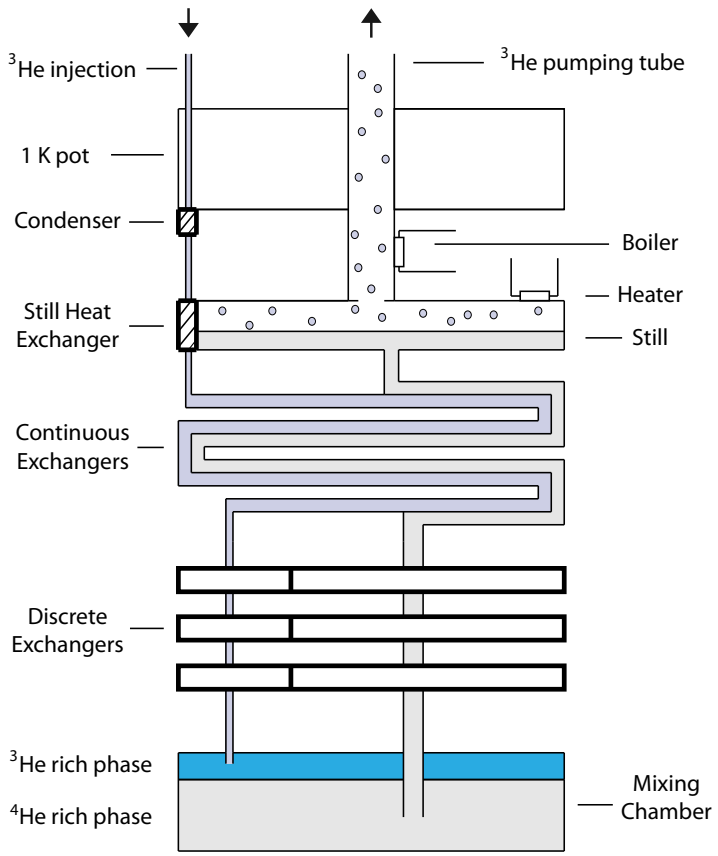

Figure 3.1: Basic components of a dilution refrigerator

as a liquid and of the poor ^3He phase as a gaz[1]. By pumping on the ^3He vapor (poor ^3He phase), the equilibrium between the two phases is destroyed. In order to reestablish the equilibrium, ^3He atoms of the liquid phase will migrate towards the vapor phase leading to an effective evaporation process. During the process energy has to be brought to the fluid. This energy will be taken from the environment, in other words the mixing chamber and the sample thermally anchored to it. By injecting back the ^3He vapor into the "mixing chamber" at the new equilibrium temperature, which is done with proper thermalization points and heat exchangers (Fig. 3.1, 1K pot, Still, continuous ans discrete exchangers), the evaporation process can be reproduced continuously and enables in practice to cool down samples to 10 mK. Figure 3.1 is a schematic representation of the dilution stage of a refrigerator as we used during this project. For a detailed understanding of dilution refrigerators and experimental principles of low temperature physics we refer

[1]Though reality is more subtle, this description enables to understand in simple terms the operation of a dilution refrigerator

the reader to [67].

3.1.2 Coaxial lines and filtering

The cabling of a dilution refrigerator is a crucial point for any low temperature measurement. Since we are interested in transport experiments at low frequency (<100 Hz) and low temperature (< 100 mK), we require wires with low resistance, low thermal conductivity and good attenuation properties at high frequency.
Following Zorin's work [68], we use "Thermocoax" cables manufactured by Philips (type 1 NcAc) with an outer diameter $d = 0.5\ \mu m$. In the role of filtering elements they presents a good alternative to ordinary power transmitting cables for several reasons. First, the DC resistance is of 50 $\Omega.m^{-1}$ and almost independent of temperature. Second, the jacket is a bulk tube, so external screening of these lines is unnecessary. Third, the thermal conductivity of the materials, i.e. inner wire, insulator, and the jacket are closely related and very low (almost 20 times less than copper at room temperature), so the lines are able to link the coldest part of the cryostat with the warmer part without important heat flow. Last and of great importance, due to skin effect in the conductors, the cables present a good attenuation factor at high frequency.
We recall the main specifications of these coaxial lines:

- **Inner wire**. NiCr alloy with a resistance per unit of length R = 50 $\Omega.m^{-1}$ only differing from a few percent at 4.2 K.
- **Jacket**. Stainless steel with a resistance per unit of length R= 6.9 $\Omega.m^{-1}$.
- **Insulator**. Highly compacted mineral powder of MgO with negligible leakage at low temperature
- **Capacitance and inductance** Capacitance and inductance per unit of length: C=490 $pF.m^{-1}$ (low RC constant) and l=0.14 $\mu H.m^{-1}$.
- **Attenuation** Typical values of the attenuation per unit of length at 10 MHz, 2 GHz and 10 GHz : $A_{10MHz}(w) \simeq 10\, dB.m^{-1}$, $A_{2GHz}(w) \simeq 100\, dB.m^{-1}$ and $A_{10GHz}(w) \simeq 200\, dB.m^{-1}$.

Figure 3.2 (left panel) shows the amplification factor, that is to say the opposite of the attenuation, of a 50 centimetres long "Thermocoax" line for frequencies above 10 MHz. In our case, 3 meters long coaxial lines were necessary to cable the fridge from the 300 K plate of the refrigerator to the sample holder. The different thermalization points are realized by soldering the jackets of the cables to different areas of the dilution stage. Therefore there are no interruptions of the lines which minimizes the possible entrance

of high frequency radiations.
Concerning low frequencies, typically below the megahertz, two types of low pass filters are used. An RC filter with a rise time of $\sim$ 1 ms and a cut off frequency at 100 Hz is connected in series with a commercial low pass filter (minicircuits SLP 1.9 +) which has a cut off frequency at 1.9 MHz (Fig. 3.2 right panel). Due to the lack of space in the fridge, these filters could not be attached to the lines at low temperature. They are connected at the top of the measuring lines at room temperature.

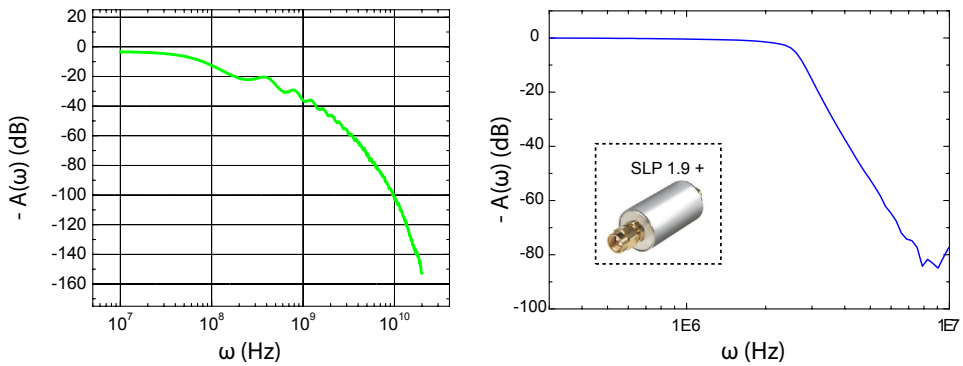

Figure 3.2: *Left panel.* Amplification factor of a "Thermocoax" line of 50 cm long at high frequencies. *Right panel.* Amplification factor of a "Minicircuit" low pass filter (model SLP 1.9 +) showing the cut off frequency at 1.9 MHz. Around 10 MHz the curve show a cusp which is actually due to the noise of the spectrum analyser in this frequency range.

The importance of filtering does not stand only on the reduction of the noise captured during the acquisition to obtain "clean" signals. Obviously minimizing the noise entering the measuring chain and amplified with the signals of interest is essential, since averaging is time consuming and useless against certain type of noise, for example $1/f$ noise [69]. However another aspect of great interest comes from the effective electronic temperature of the electrons flowing through the sample. We already mentioned this in the previous chapter, when we presented Coulomb blockade. The point is that, it is not sufficient to cool down a sample holder to low temperature to insure that the electrons flowing through the sample itself have the same temperature. In order to understand this statement, we recall the two main mechanisms that participate to the thermalization of free electrons in conductors. First, the electron-phonon interaction enables to cool down electrons by cooling down the lattice. This process, very efficient at high temperatures, becomes negligible below 1K typically. At lower temperature, another type of interaction tends to thermalized a bath of electrons : the electron-electron interaction [70]. In this regime, the thermal bath that allows to thermalize the conduction electrons within the sample is actually the wires [71] (they

can be considered as thermal baths due to their macroscopic size). The noise

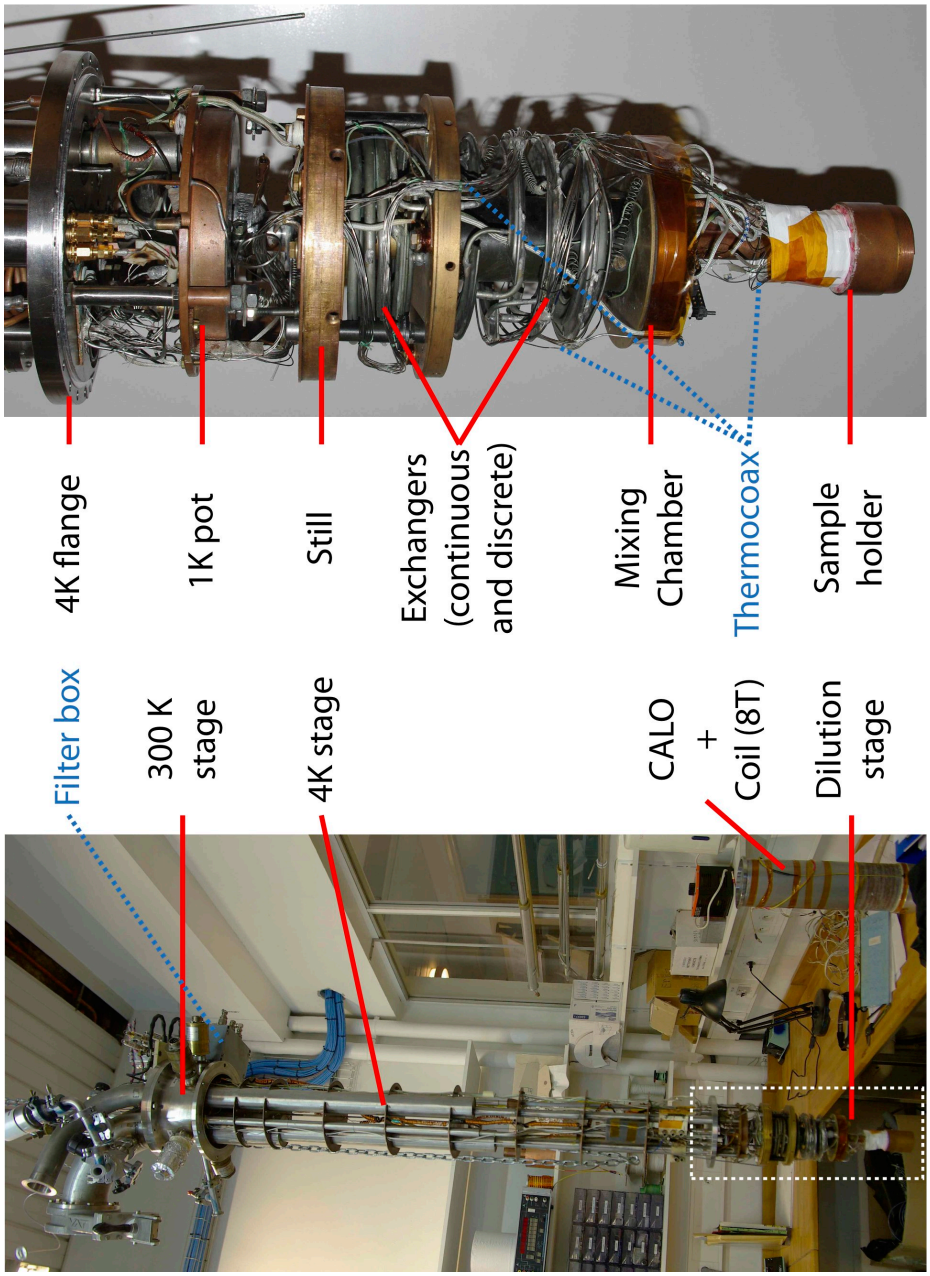

Figure 3.3: Pictures of the dilution refrigerator used during this project. *Bottom panel.* Entire vue of the fridge and the calorimeter (CALO) holding the 8 Tesla coil. *Top panel.* Zoom on the dilution stage showing the essential elements from the 4K flange to the mixing chamber under which the sample holder is thermally anchored.

entering the acquisition chain provides energy to the electrons of the hole setup and can be seen as a heating source. This effect is not important at high temperature, but is of great concern for the parts sitting at low temperature, that is to say the wires and the sample. An excess of noise will inevitably manifest itself in a difficulty to effectively cool down a sample at very low temperature, in other words to get a low electronic temperature. In that sense filtering plays a crucial role.
All the different elements cited previously, from cryogenics to filtering, can be identified on figure 3.3 which displays an overview of the dilution refrigerator used for all the experiments performed on double quantum dots, and a close up view of the dilution stage.

3.2 Electronics

The different electronic instruments used to polarize the metal gates, to bias the quantum dots and to detect the out coming currents, were all developed in the Néel Institut. This work was done in close collaboration with the NANO and MCBT electronic departments under the direction of Daniel Lepoittevin [72], Christophe Guttin [72] and Tristan Meunier [72].

3.2.1 Digital-to-analog converters

Specifications

The bias voltage across the dot and the DC voltages used to polarize the lateral gates, are generated by digital-to-analog converters (DACs) that enable to remote control the quantum dots through a virtual interface on a computer. Many DAC chips are available in the commerce corresponding to different uses (audio, video, ...). In our case, our choice was motivated by two main criterions : the stability of the output voltage of the chip within temperature and time. A very good candidate is the LTC2642 16 bit DAC, manufactured by Linear Technology.
We recall here the principal specifications of this chip:

- **Resolution**. 16 bits on a ± 5 V scale, that is to say 150 μV resolution
- **Supply current**. Low supply current, 120 μA, allowing to operate the DACs on batteries to avoid as much as possible ground loops and reduce interferences effects on the measurement signal
- **Ouput noise**. 30 n$V_{rms}/\sqrt{Hz}$
- **Thermal drift**. 0.25 ppm/°C

The following bench tests confirm the noise level within frequency and the quality of the stability of the output voltage of the LTC2642 DAC. A power

spectrum in units of $V_{rms}/\sqrt{Hz}$ within a frequency range from 100 Hz to 100 kHz, is displayed in the top panel of figure 3.4. In agreement with the specifications, we obtain an almost flat frequency spectrum with a noise level at $\sim$ 25 $nV_{rms}/\sqrt{Hz}$. Measurements at higher frequency, typically above 1 MHz, show a diminution of this noise floor down to $\sim$ 20 $nV_{rms}/\sqrt{Hz}$. The 1/f noise structure present around 100 Hz is actually the 1/f noise of the spectrum analyser. The bottom panel shows the total output voltage integrated over a 100 kHz bandwidth.

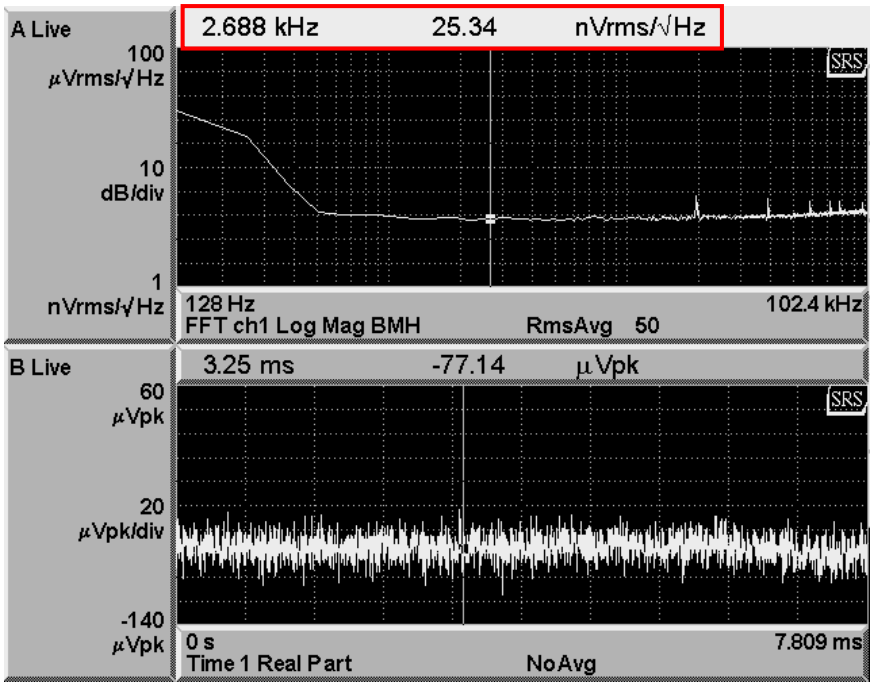

Figure 3.4: *Top panel.* Power spectrum in units of $V_{rms}/\sqrt{Hz}$ of the voltage output of a LTC2642 DAC in the frequency range 100Hz-100kHz.*Bottom panel.* Output voltage integrated over a 100 kHz bandwidth.

Concerning the stability, figure 3.5 shows a measurement of the DAC output voltage within time. A polarization of -1 V was applied and monitored during 15 hours with a Keithley 2002 digital multimeter. Note that the temperature was not monitored at the same time, therefore we cannot decorrelate the drift within temperature and the drift within time. However this simple experiment shows a total drift of $\sim$ 10 μV for the entire acquisition time.

Metal gates polarization

All metal gates are polarized with DC voltages of the order of -1 V. Since the quantum dots are defined through the voltages applied on the gates, it is necessary to deliver clean (low noise) and stable signals on the lateral gates.

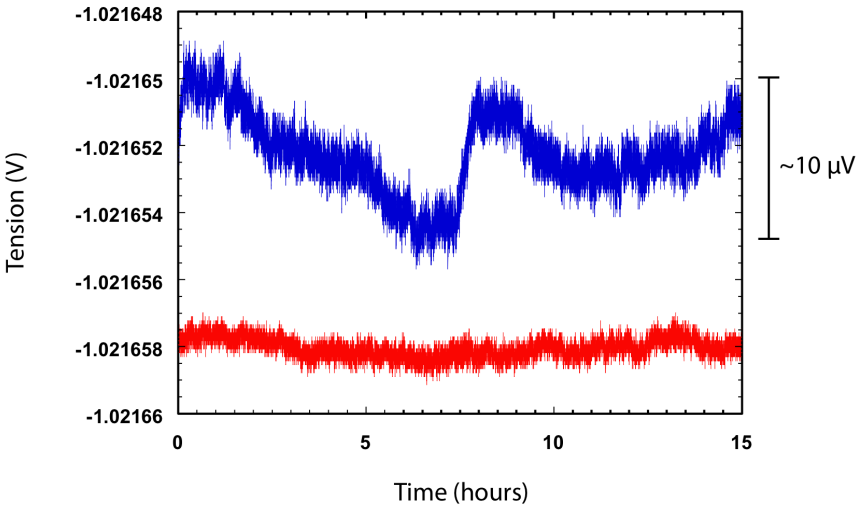

Figure 3.5: Stability of the voltage output of a LTC2642 DAC. Red curve : Voltage input drift of the digital multimeter (Keithley 2002) when grounded. The curve has been offset for clarity. Blue curve : voltage output drift of the DAC measured with the multimeter.

The output voltages of the DACs are filtered through 3 different types of filters as mentioned previously : RC filter 100 Hz cut off, SLP 1.9 MHz cut off and "Thermocoax" lines with high attenuation at high frequency, typically the gigahertz. Therefore the total output noise is strongly reduced and the effective temperature extracted from Coulomb blockade peaks (30-40 mK) illustrates the quality of the voltages applied at the end of the coaxial lines (bias voltage is another limiting parameter). Concerning the stability, we can estimate at $\sim 1\mu V$ for a change of 5°C of T_{room}) when a 1 V polarization is applied. Note that the experimental room is air conditioned, which actually makes our estimate a high limit. The drift within time cannot be eliminated and we know that it is of a few μV (Fig 3.5) for several hours. To give an idea of the impact of such a drift, lets convert this few microvolts scale into an effective energy within the dot. The conversion is made via the alpha factor that is typically of the order of the 10% for metal gates in lateral quantum dots. We find an energy drift induced by the metal gates around the μeV. This energy scale is well below the intrinsic energy scales of our quantum dots and beyond our detection sensitivity. Therefore we will not be much concerned by drifts that small developing on such time scales.

Bias voltage

The bias voltage across the structure is composed of a DC and a AC excitation super imposed by using a single DAC channel. The idea is to monitor

responses of the system only at the frequency of the AC excitation (around 10 Hz) by performing a synchrone detection. First of all, the synchrone detection is a way to minimize the influence of the noise on the measurement by optimizing the signal to noise ratio: the measurement bandwidth is shifted at a chosen frequency and can be made very narrow around it. Then, this type of measurement, that is to say collecting the AC response to a DC+AC excitation, is a direct dI/dV measurement, in our case a direct measurement of the differential conductance, which avoids numerical noise normally produced when performing a numerical derivative. The bias voltages we apply, are usually of the order of $2\mu eV$. To achieve such low biases, a voltage divider is necessary and has the advantage of dividing the entire noise level too. Thermostable resistances manufactured by CADDOCK (USF 200, 2 ppm/°C) were used to realize our voltage dividers. Again for a problem of space, the voltage divider could not be placed near the sample at low temperature and we connect it in series with the different filters : RC filter 1kHz cut off (to avoid out of phase signals), SLP 1.9+ and "Thermocoax" lines.

Communication

The software layer was developed in collaboration with Sylvain Hermelin [72]. Communication with the different DAC channels is made via an Ethernet connection with a National Instrument card sbRIO-9602 integrating a real time processor, a FPGA circuit and different I/O. This logical circuit allows for a large amount of uses and enabled us to configure a synchrone detection (AC+DC excitation on a single channel, numerical demodulation) minimizing the entrance of extra noise in the measurement chain by eliminating additional instruments. It offered also the possibility to deport the main part of the signal processing on the card, which means a gain of time by avoiding delay times usual commercial operating systems suffer from. Finally this solution is a relatively low cost solution with the possibility to integrate a large number of DAC channels (~ 100) in a reduced space.

3.2.2 Current-to-voltage converter

The current (AC+DC) outcoming of the system in response to the voltage excitation, is collected by a current-to-voltage converter (Fig. 3.6) that converts and amplifies the signal which is finally demodulated to extract the differential conductance.
The first concern is the input current noise of the amplifier since the currents we want to deal with span in a range of a few hundreds of fA to a few tens of pA. The progress in electronics is such that nowadays, I/V converters are only limited by the Johnson-Nyquist noise of the feedback resistance giving

the gain of the amplifier.

$$I_{converter} = \sqrt{\frac{4k_B T \Delta f}{R_{feedback}}} \tag{3.1}$$

In the tunnelling regime, the typical gain we use is a 10^9 gain, that is to say a 1 GΩ feedback resistance which leads to an input current noise of 4.3 $fA/\sqrt{Hz}$. Figure 3.7 is a measurement of the noise spectral density in units of $fA/\sqrt{Hz}$ that confirms a noise level situated around 4 $fA/\sqrt{Hz}$. The reduction of this noise after 100 Hz is due to the cut off frequency of the amplifier at this gain.

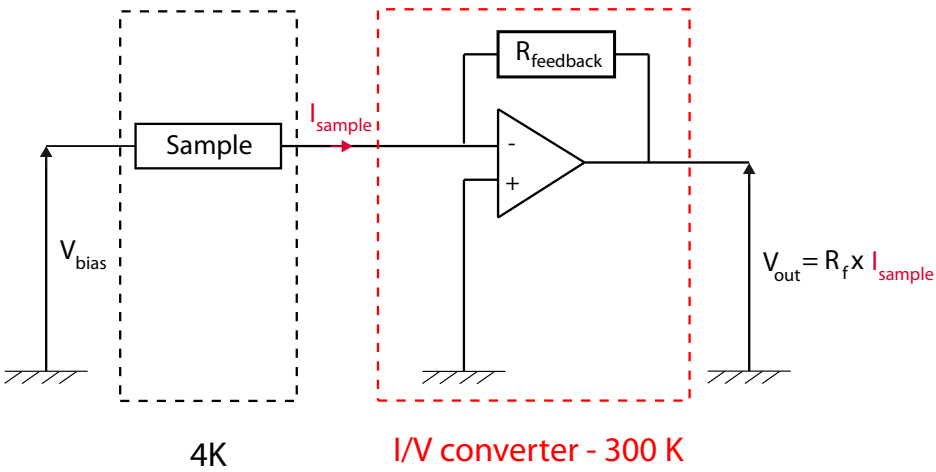

Figure 3.6: Schematic two point measurement used to study transport through quantum dots. The red dashed box encloses the I/V converter sitting at room temperature. The black dashed box encloses the sample, sitting at low temperature in the dilution refrigerator.

Another important feature is the input voltage offset. Each I/V converter presents a voltage input offset which can be tuned via an adjustment screw in our case. It is actually difficult to make it smaller than a few tens of μV. Since this offset directly biases the sample (on the drain), it has to be countered with the bias voltage (on the source) to achieve zero DC bias. The main problems related to the voltage offset are the noise it brings on the sample and the drift it is subject to.
A excess of noise on the input would manifest itself by instabilities of the structure and cooling problems for reasons we have already evoked (section 3.1.2). It is worth noting that no voltage divider is present as in the case of the bias voltage applied on the source. We therefore need a low noise input and good filtering at high frequency. The filtering set-up has already been addressed earlier, we just emphasize that no RC filter is used before the I/V

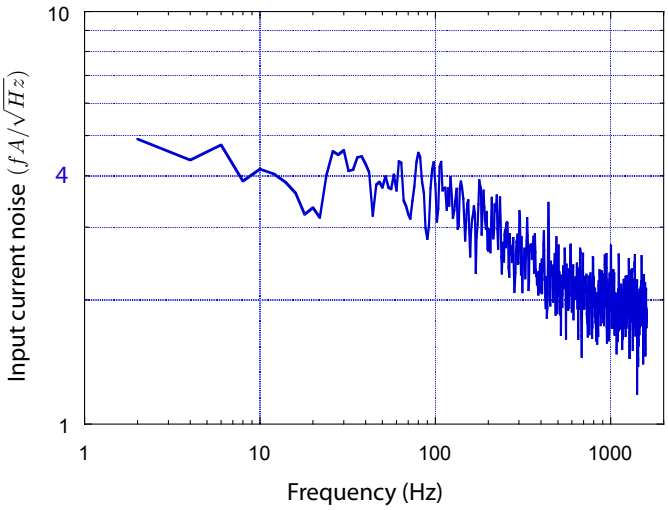

Figure 3.7: Ouput current noise spectral density in units of $fA/\sqrt{Hz}$. The reduction of the noise level after 100 Hz is due to the cut off frequency of the I/V converter.

converter due to impedance mismatching. Figure 3.8 shows the noise level at the input of the amplifier with a pronounced peak at 50 Hz showing the influence of the electrical network and a relatively high 1/f noise structure. The white noise extracted from the power spectrum lies at 10 $nV/\sqrt{Hz}$.

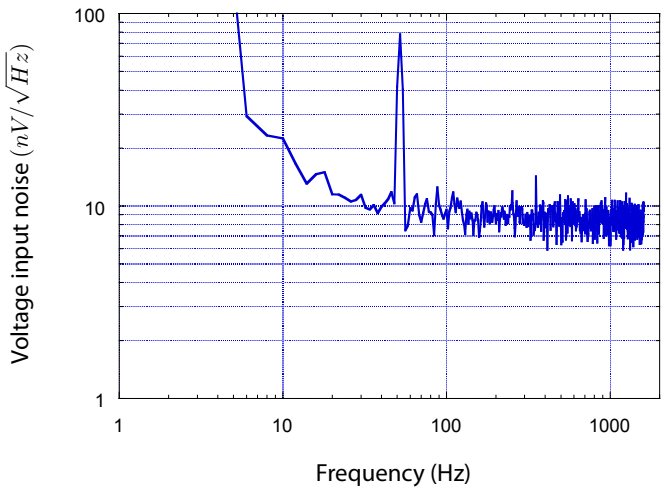

Figure 3.8: Voltage input noise spectral density of the I/V converter in units of $nV/\sqrt{Hz}$. The sharp peak centered at 50 Hz shows the dramatic influence of the electrical network via ground loops.

As we mentioned, the zero DC bias will be defined with respect to the

voltage offset at the input of the converter (the offset of the DAC+divider is negligible). To equilibrate the electrochemical potentials on the source and drain, one has to counter the offset due to the amplifier on the drain, with the voltage bias applied via the DAC. In the case of our experiments the voltage offset on the converter is of 140 μeV at room temperature with a variation of a few μeV at low temperature at the end of the coaxial line. To identify the effective zero DC voltage bias we perform Coulomb blockade measurements at low temperature. By focusing on the amplitude of the Coulomb peaks (in DC current), we search for the bias corresponding to a situation where this amplitude is suppressed, that is to say when the electrochemical potentials of the dots are equal. An AC component is then added to the DC component on the source to create a voltage bias across the quantum dots. A delicate point as mentioned, is the drift within temperature and time of the I/V converter offset that effectively changes the zero bias across the structure. For this purpose, our home made converter is based on a stable Texas Instrument chip (TLC220). A stability measurements of the voltage offset of the I/V converter is shown in figure 3.9.

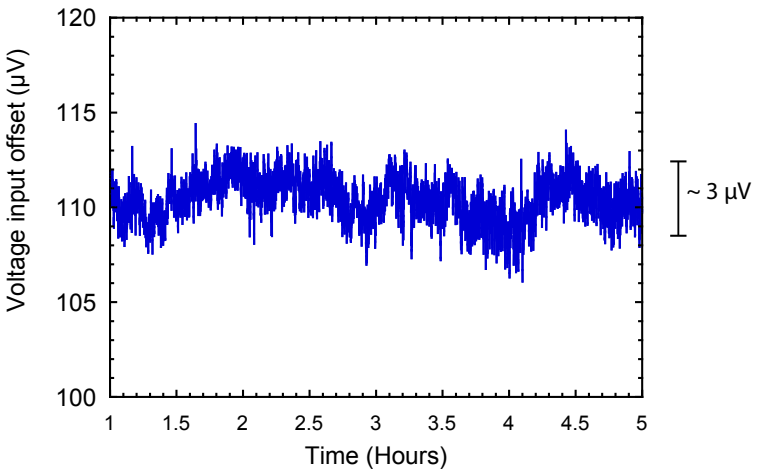

Figure 3.9: Stability of the voltage input of the I/V converter used during this project. The voltage input was monitored with a Keithley 2002 multimeter. We find a total drift (time+thermal) of 3 μV for a 5 hours acquisition measurement.

A total drift of $\sim 3\mu V$ was measured within 5 hours of acquisition with a Keithley 2002 already used to measure the stability of our DACs. Note that the Keithley multimeter has a voltage input drift on the order of the μV (Fig. 3.5, red curve). We can estimate the drift of the I/V converter around 2 μV. This gives us the accuracy of the definition of the effective zero bias across the structure for long time acquisitions.

3.2.3 Acquisition chain

We summarize the different elements entering the acquisition chain in the schematic representation given in figure 3.10.

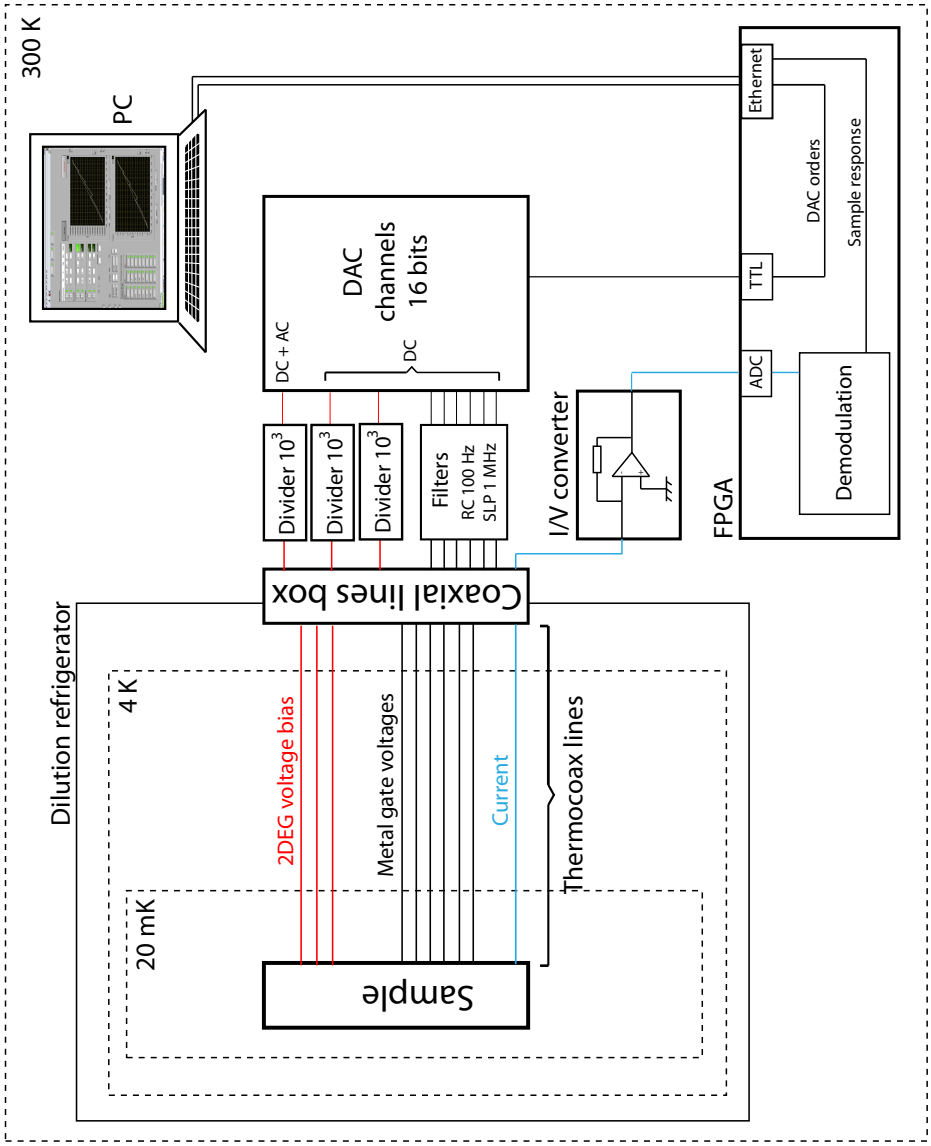

Figure 3.10: Schematic representation of the acquisition chain used to study transport through quantum dots.

Chapter 4

Experiments and interpretations

In this chapter we will present experiments performed on a double quantum dot sample where the inter-dot tunnel coupling and the coupling to the free electron reservoirs, influence drastically transport through the system. These studies aim to understand the effect of the hybridisation of a quantum dot with metallic leads, that is to say a conventional non interacting reservoir and with a second quantum dot which can be regarded as an interacting finite reservoir. As mentioned earlier, in each experiment we probe the conductance through the small quantum dot side coupled to a large quantum dot.
We know from the Meir-Wingreen formula [73] that the conductance through an interacting region of electrons is related to the spectral function of this region and from which can be derived the addition spectrum. Our goal will be to understand how the different couplings in the system modify the addition spectrum of the small quantum dot and how this reflects in the conductance through the total system.
Before going into details of each experiment, we recall the main characteristics of the sample and the set-up used to study transport through the system. Note that all the experiments we will discuss in the following, were performed using the same double quantum dot sample. The following table (Table 4.1) summarises the different sizes[1] and bare energy scales of each quantum dot composing the device[2].
As mentioned in section 2.4.2, Chapter 2, the equivalent electrical set-up used to probe the transport properties of the two quantum dots is a T-shape geometry. As one can see in figure 4.1, in this set-up only the small

[1] The sizes indicated represent the lithographic sizes.

[2] The different energy scales were measured via non linear transport experiments (Coulomb diamonds, Chap 2, section 2.3.5). They were extracted by polarizing only one quantum dot at a time, this is why we refer to them as bare energy scales.

	Small dot	Large dot
Size (nm)	500	1500
Charging energy (μeV)	700	300
Level spacing (μeV)	150	20-30

Table 4.1: Table recalling the lithographic sizes of each quantum dot forming the double dot and their bare charging energies and level spacings.

dot connects through tunnel barriers to the metallic leads. All the measurement are performed as follows : a voltage bias is applied on one lead of the small dot and the response of the system to this excitation is collected via an I/V converter connected to the remaining lead (Fig. 4.1, purple dashed box). This set-up enables us to monitor the conductance of the small dot only. We can actually reformulate this: from the point of view of quantum mechanics, our geometry allows us to probe only the part of the total wave function of the system belonging to the small dot and effectively connecting to the reservoirs. The presence of the large dot, tunnel coupled to the small dot, will then be seen in the conductance due to hybridisation of the wave function.
In practice, to achieve the T shape set-up we require two main features we already addressed in chapter 2 and 3 and that we recall here for clarity:

- To insure that the large dot only couples to the small dot, we need to isolate it from the nearby conduction electrons. This is done by pushing the gates defining the coupling of the large dot to the surrounding mesa (Fig. 4.1, dashed leads), far in the pinch off regime (Fig. 4.1, dashed red lines). That way, charge fluctuations through the tunnel barriers formed by the gates develop on very long time scales and can be neglected in our analysis. We consider that the large dot fluctuates only via tunnel processes through the smaller dot.

- To be able to apply a single voltage excitation on one lead with respect to the others, we need to define the same potential for the three other leads (1 lead small dot, 2 leads large dot). We mentioned in chapter 3 that the I/V converter brings a non negligible voltage offset on the lead it connects to (Fig. 4.1, point A). This voltage offset, of the order of 140 μeV, is large compared to the small voltage biases we usually apply ($V_{excitation}$) that are of the order of the μeV. This bias offset is compensated on the other lead of the small dot ($V_{bias} = V_{excitation} + V_{offset\ I/V}$), but also on both leads connected to the large dot ($V'_{bias} = V_{offset\ I/V}$). Even though the tunnel barriers connecting the large dot to its leads are far in the pinch off regime, such a high offset has to be compensated to avoid large potential differences between the leads that can give rise to parasitic cross currents.

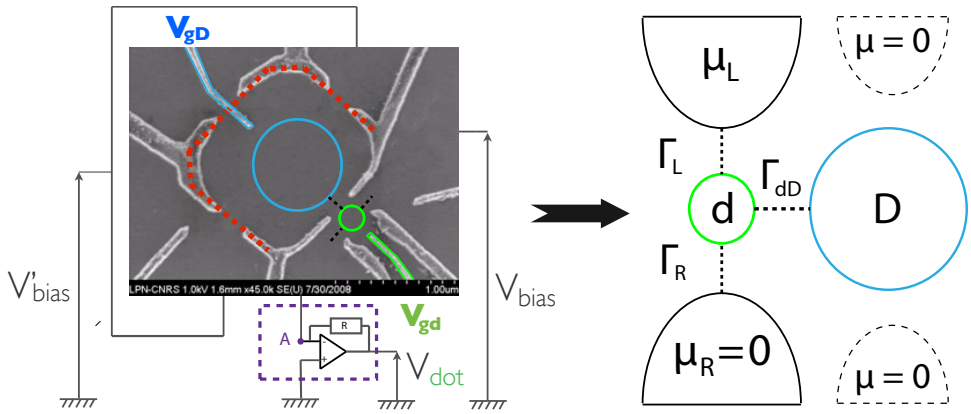

Figure 4.1: *Left panel.* SEM image of the double quantum dot. A green and a blue circle sketch the quantum dots formed in the mesa. The red dashed line superimposed of the large dot gates indicates that these gates are pushed far in the pinch off. The black dashed lines indicate the relevant couplings in the system ($\Gamma_{Leads-dot}, \Gamma_{dot-Dot}$). The position of the excitation voltage (V_{bias}), the I/V converter (purple dashed box) and the voltages applied on the large dot leads (V'_{bias}) have been added for clarity. *Right panel.* Scheme of the equivalent geometry. The dashed leads surrounding the large dot will not enter our analysis and will be dropped.

The different experiments will be presented as follows:

We will present an experiment where we will focus on the effect of inter-dot tunnel coupling and try to understand how this influences transport through our device in a regime where hybridisation involves several energy levels. To account for the physics of a multi-level interacting system we will have to go beyond the semi-classical description used in chapter 2 (sec. 2.4.1) to describe transport through weakly interacting quantum dots. A particular interest will be given to the evolution of the transport properties when the temperature of the sample is increased.

In a second experiment we will focus on the study of a pronounced Kondo effect defined on the orbital degeneracy ridge of the double dot where the system is blocked due to the mutual charging energy of the dots (Fig. 2.11, 3). We will understand how such a Kondo effects develops at that particular degeneracy point and discuss the degrees of freedom involved. Evidence of the hybridisation of the dots energy levels will lead us to study the interplay between the Kondo temperature defined via the coupling with the leads and the exchange interaction defined through the inter-dot tunnel coupling.

4.1 Interplay between inter-dot tunnelling and temperature

We report first on measurements where we will investigate the effect of hybridization between the dots mediated by the inter-dot tunnel coupling, t_{dD}, and try to understand how this influences transport through the device at low and high temperature. From the strong tunnelling element connecting the dots found in the stability diagrams, a multi level molecular approach will be necessary to describe the double dot. The effect of temperature will be captured via the number of molecular states participating to the transport. A comparison between k_BT and t_{dD} will enable a definition of "low" and "high" temperature limits.

4.1.1 Low temperature and high temperature limits

The major observations are found in the low temperature stability diagram and its evolution in temperature. The low temperature, 20 mK, and high temperature, 500 mK, stability diagrams are depicted in figure 4.2 as color plots of the differential conductance in units of $\frac{e^2}{h}$, as a function of V_{gd} and V_{gD}. For clarity, three dimensional graphics of the previous colorplots are shown in figure 4.3.
The global remarks we can make from these diagrams are:

- *Leads-dot coupling.* In the low temperature stability diagram, the conductance monitored within the Coulomb blockade valleys is of the order of $10^{-3}\frac{e^2}{h}$. This value has to be compared with the weak coupling limit, $\Gamma_{dot-leads} \leq k_BT < \Delta E, E_C$ [32], where the conductance within the valleys is of the order of $10^{-4}\frac{e^2}{h}$, as shown in figure 2.12. It appears that in figure 4.2 the conductance is enhanced in the vicinity of the Coulomb blockade valleys. This effect can be attributed to cotunneling events contributing to the conductance due to finite coupling of the system with the leads. However, we are still far from the strong coupling limit as we will see in the following experiment (see section 4.2) where the conductance in the Coulomb blockade valleys is 100 times larger, ($\sim 0.1\frac{e^2}{h}$). Therefore, the coupling of the double dot with the leads will be treated as a weak perturbation in the following, $\Gamma_{weakcoupling} \leq \Gamma_{current\ \ experiment}$, and we will concentrate on the effect of inter-dot tunnel coupling. Effects of non negligible coupling to the leads, $\Gamma \sim \Gamma_{Kondo\ \ regime}$ will be discussed at the end of this section.

- *dot-Dot coupling.* In the low temperature and high temperature limits, the degeneracy points of the system appear as smooth lines which do not follow a honeycomb lattice. This regime appears as a molecular regime (see strong coupling limit Chap 2, sec. 2.4.2 and 2.4.3)

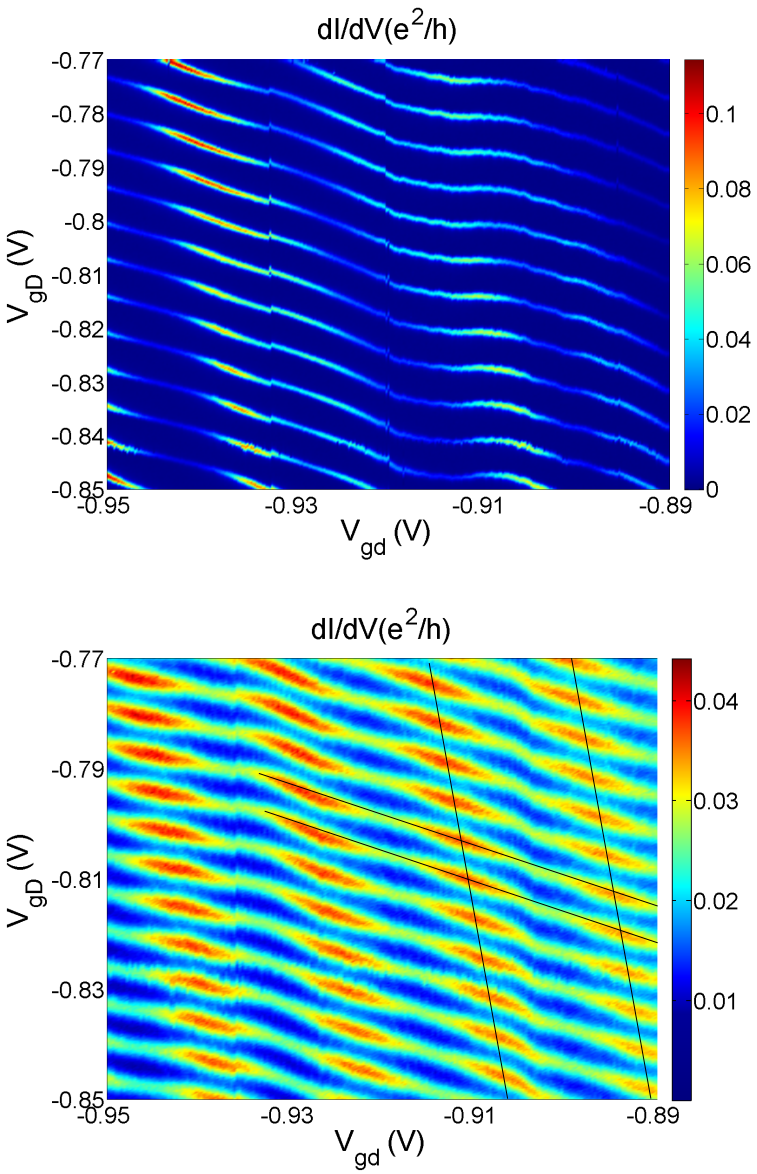

Figure 4.2: Low temperature and high temperature stability diagrams of the double dot system. *Top panel* Colorplot in units of $\frac{e^2}{h}$ of the low temperature stability diagram (20 mK). The degeneracy points of the system appear as smooth lines in the diagram differing a lot from the usual honeycomb lattice and indicating strong inter-dot tunnel coupling. The pattern followed by the degeneracy lines appears to be complex and cannot be interpret in terms of independent dots, again indicating strong inter-dot coupling. *Bottom panel* High temperature diagram, 500 mK. The degeneracy points still appear as smooth lines, however the complex low temperature pattern has been lost and a regular pattern is observed at higher temperature.

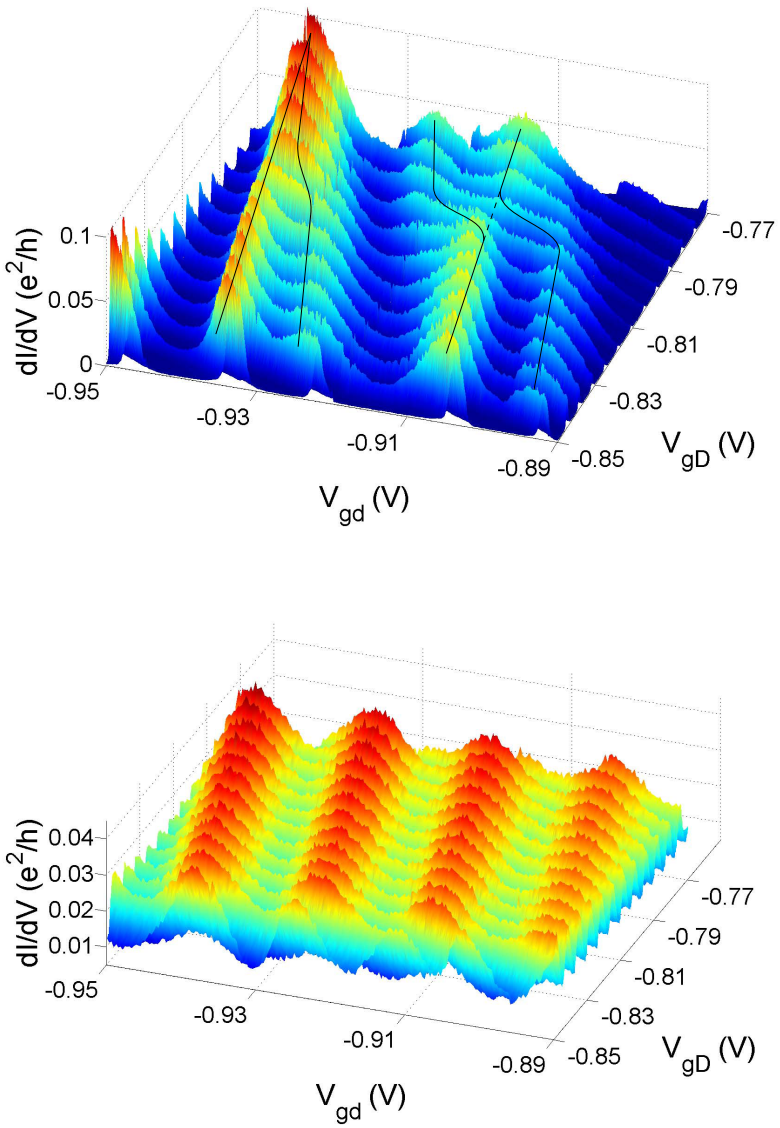

Figure 4.3: Low temperature (top panel) and high temperature (bottom panel) stability diagrams of the double dot system shown in three dimensional plots. The complex low temperature pattern and regular high temperature pattern followed by the degeneracy points of the system appear with more clarity in these graphics.

where almost diagonal degeneracy lines are observed. This indicates a strong inter-dot tunnel coupling smoothing out the honeycomb lattice. Note that these lines appear as equally spaced, indicating a constant addition energy for the complete system dot+Dot.

- *Conductance pattern.* At low temperature the conductance pattern, that is to say the modulation along the molecular degeneracy lines, is quite irregular. As depicted in figure 4.3 (top panel), large conductance peaks unequally spaced along the V_{gd} direction are observed, indicating the reminiscence of the small dot charge states. Moreover in the V_{gD} direction we can see that on the left part of the diagram two peaks structures merge, and on the right part of the diagram two peak structures cross each other. The point is that in the framework of the constant interaction model usually used, we expect that the molecular degeneracy lines display a periodic modulation because the addition of electrons in each dot is controlled by their respective addition energies that tend to be almost constant in our dots[3]. The reminiscence of the small dot and large dot charge states would result in a periodic and continuous modulation of the conductance along the diagonal lines. We cannot account for the observed irregularities in this framework.

- *Temperature evolution.* Surprisingly, when the temperature is raised, a rather regular conductance pattern is recovered (Fig. 4.2, bottom panel). That is to say, the modulation of the conductance along the molecular degeneracy lines follows a periodic modulation, indicating a regular filling of each dots that can be accounted for in the framework of a constant addition spectrum of the dots.

In order to describe transport at low temperature we need to work in a more general framework than the semi-classical constant interaction (model Chap. 2, sec. 2.4.1) to understand why irregularities in the conductance pattern (or in the reminiscence of the charge states of both dots) are observed at low temperature and how they can disappear at high temperature. We believe that the main parameter explaining these unexpected diagrams, results from the strength of the inter-dot tunnel coupling. Therefore we will focus on the molecular addition spectrum of the system and consider the coupling to the leads as a weak perturbation to simplify our study. We will see that due to the important value of the inter-dot tunnelling and the relatively low value of the large dot level spacing ($20\mu eV$), several energy levels will be involved in the hybridisation process and a multi level description will be required to apprehend transport. Interestingly the effect of temperature will be incorporated quite naturally in our model via the number of molecular

[3]Measurements performed on both dots independently show a rather constant addition energy. This is due to the fact that their addition energy is dominated by their charging energy, much larger than their level spacing.

states involved in transport.
With the help of numerical calculations we will simulate conductance maps in order to confront our model to the experimental data. All theoretical and numerical investigations were done in close collaboration with Denis Feinberg [72] (theory), Carlos Balseiro [74] (theory and numerical code) and Pablo Cornaglia [74] (theory and numerical code). Note that our goal is not to reproduce the entire stability diagram but to capture as much physical effects as possible via this description.
Before going into the core of the multi-level interacting dot model, we will address briefly two extreme limits in order to situate the context of this experiment : the weak inter-dot tunnel coupling and the strong inter-dot tunnel coupling regime[4]. As we will see simple pictures of the system can be given in these limiting regimes. For small tunnel coupling, the system will display a behaviour close to uncoupled[5] dots (honeycomb diagrams). For large tunnel coupling, no distinction will be made between the wave functions of each dot and the system will behave as a large quantum dot (merged dots).

4.1.2 inter-dot tunnel coupling : limiting cases

To situate the context of the experiment we present in this part two limits that can be addressed in double quantum dots : the weak inter-dot tunnel coupling regime and the strong inter-dot tunnel coupling regime.

Weak inter-dot tunnel coupling

The problem of weak inter-dot tunnel coupling was already addressed in chapter 2, section 2.4.3 in the framework of a two level system. We recall here the main points and the range of validity of this simple description.
For weak tunnel coupling, the behaviour of the double dot differs weakly from purely capacitively coupled dots. A honeycomb lattice is found in the low temperature stability diagram (Fig 2.12, panel b) and the effect of inter-dot tunnelling is seen as a small correction to the honeycomb that appears to be slightly smoothed near the triple points because of the formation of molecular states.

Hypothesis

To describe transport in this regime, the following hypothesis are made:

- The electron-electron interactions are treated via a charging energy in the framework of the constant interaction model (chapter 2, sec

[4] We will precise what we mean by "strong" and "weak" limits
[5] Uncoupled from the point of view of tunnel coupling

2.4.2). To take into account orbital effects, we make the following approximation : $\mu_{system}(N) = \mu_{classical} + \Delta E$ where the electrochemical potential of the system is described as the sum of a classical contribution representing a mean field Coulomb interaction [6] and an orbital contribution that implicitly takes into account energy renormalization effects coming from the formation of molecular states between the dots.

- The effect of inter-dot tunnelling leading to the formation of molecular states is done via a two level system in the case of a single electron (one level per dot). Only the top most occupied energy levels of each dot are considered. Spin effects are neglected by considering a single electron. Transport is described as the tunnelling of a single charge.

Range of validity

By assuming we can describe our double dot as a two level system tunnel coupled, we assume that the hybridisation process involves only two energy levels. This approximation as we will see later is actually strong. It implies that the tunnel coupling is smaller than the other intrinsic energy scales of the system, in other words $t_{dD} < \Delta E_{d(D)}, E_{dD}, E_{d(D)}$. We recall the notations used in chapter 2 for clarity:

- $\Delta E_{d(D)}$: level spacing in dot d (or D)
- E_{dD} : mutual charging energy of the double dot
- $E_{d(D)}$: charging energy of dot d(or D).

By referring to table 4.1, we can see that the lowest energy scale will be the level spacing of the large dot, $\Delta E_D \sim 20\mu eV$. This value sets the minimum criterion required to account for transport in our double dot via a two level representation.

An estimation of the tunnelling matrix element between the dots can be extracted from figure 2.12 (panel b) in order to confirm the two level scenario. By analysing the deviation of the experimental degeneracy lines from the underlying honeycomb structure, a value of t_{dD} can be extracted. On a triple point, this deviation is exactly t_{dD} (Chap 2, sec. 2.4.3), with a conversion factor transforming gate voltage to energy that is the alpha factors of each plunger gate. In figure 2.12 (panel b), we find a shift in gate voltage of 300 μV on each gate, which corresponds to a tunnel coupling around 20 μeV for alpha factors of the order of 0.05 (measured in previous experiments). If we compare this estimation to the large dot level spacing (smallest level spacing), we find that $t_{dD} \lesssim \Delta E_D$. This estimation confirms a two level scenario, and that we are in the limit of this description.

[6] Described via a network of capacitors

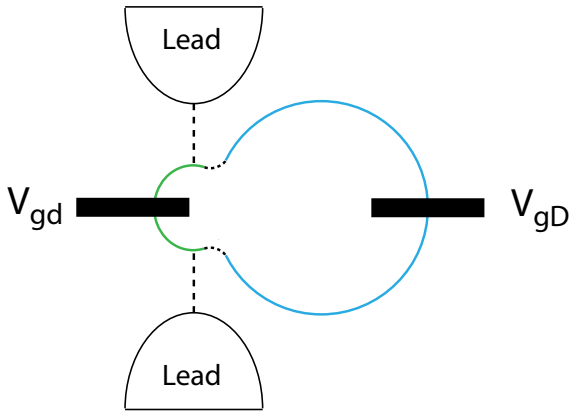

Figure 4.4: Schematic representation of the double in the strong coupling limit. The system acts as a single large quantum dot controlled via two plungers gates (black rectangles).

Strong inter-dot tunnel coupling

In the other limit, that is to say strong inter-dot tunnel coupling, we expect the double dot system to act as a single molecular object where no distinction can be made between one dot or the other.
This regime corresponds to $t_{dD} \gg \Delta E_{d(D)}, E_{dD}, E_{d(D)}$, in other words t_{dD} is the dominant energy scale of the problem.

- $t_{dD} \gg \Delta E_{d(D)}$. From this equation we know that several levels of each dot will be involved in the formation of the molecular spectrum of the system. Although we do not know the complete molecular spectrum, we can anticipate from equation 2.34 that the mixing parameter will be quite homogeneous as a function of detuning of the dot levels. The resulting molecular states will hold an equal proportion of the small dot and large dot wave functions in the entire stability diagram.

- $t_{dD} \gg E_{dD}, E_{d(D)}$. For a tunnel coupling exceeding the intrinsic charging energies we expect that an electron charging one dot will be able to tunnel immediately to the other dot and vice versa. As a result we can only talk of the charging of the entire object.

The above assumptions tend to wash out the distinction one can make between each dot. A simple description of the double dot device in this regime is to think of it as a large dot enclosing both dots, that can be controlled via two plunger gates (Fig. 4.4). As in the case of weakly interacting quantum dots, transport can be described in this limit with a semi-classical formalism (chap 2, sec. 2.3.3) already introduced in the context of transport through single quantum dots.

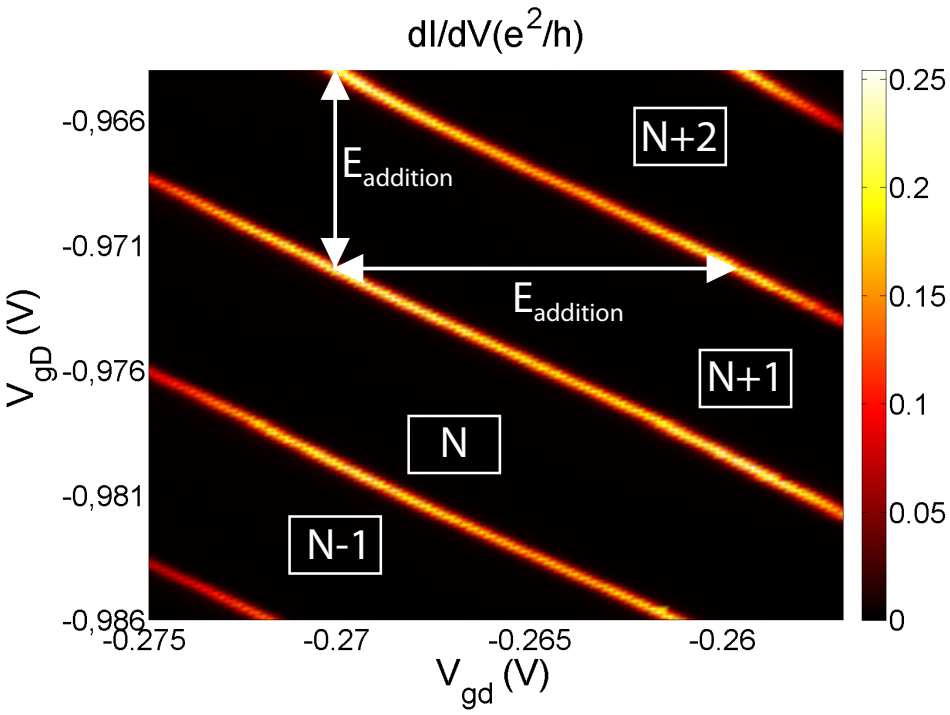

Figure 4.5: Stability diagram monitored at low temperature in our double dot device. The coupling of the system with the leads is weak (FWHM of the Coulomb peaks : 40 mK). The inter-dot coupling is made very large by depolarizing sufficiently the middle gates. The stability diagram displays diagonal degeneracy lines which are not subject to a modulation of their amplitude.

In terms of transport, the stability diagram will be composed of a series of diagonal degeneracy lines in the (V_{gd}, V_{gD}) space, indicating that controlling the system via one plunger gate or the other is equivalent. The slope of these lines are determined by the alpha factors of the corresponding gates. Moreover, since no distinction can be made between each dot, this lines should not display a periodic modulation of the conductance typical of the reminiscence of the charge states of the small dot. Therefore a flat conductance is expected along a degeneracy line of the system. This behaviour can be seen in the stability diagram shown in figure 4.5 that corresponds to an experiment performed at low temperature (20 mK) in our double dot device. This regime was achieved by depolarized as much as possible the middle gates separating the dots, which leads to important inter-dot tunnelling. Let us recall that in large quantum dots where the ratio $E_C/\Delta E$ is large, the addition energy is dominated by the charging energy determined by the geometrical size of the device (constant interaction model). Thereby

equally Coulomb blockade peaks or lines (in a 2D gate space) are expected (see Fig. 2.4). These features appear in the stability diagram addressed in figure 4.5.

Intermediate regime

As mentioned, the problem we want to address within this experiment (Fig. 4.2, Fig. 4.3) is the intermediate regime, where a multilevel system is required in order to account for the molecular spectrum, but where the charging energies of each dots are the dominating energy scales of the problem. We assume that the experimental regime within this experiment corresponds to: $\Delta E_D < t_{dD} < E_{dD}, \Delta E_d < E_D, E_d$. Numerical simulation will help us to confirm this hierarchy.
We want to emphasize here, that even though a simple description can be achieved in the case of weak and strong inter-dot tunnelling, the evolution from one limit to the other is not straightforward (Fig. 4.6).

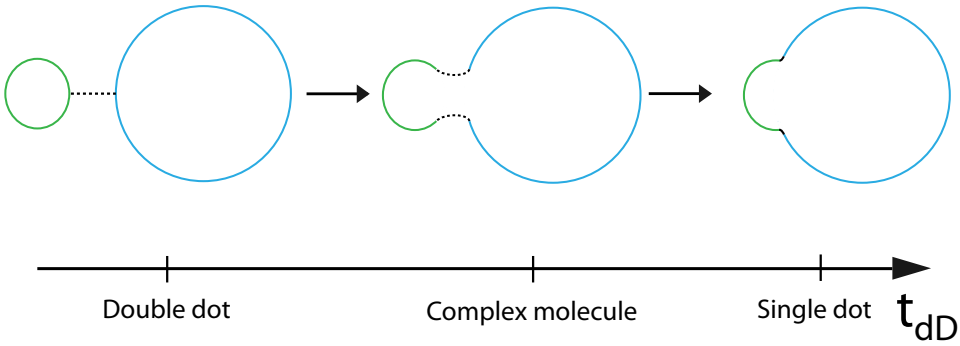

Figure 4.6: Schematic representation of the evolution of the inter-dot tunnel coupling in the double dot.

Starting from the weak coupling limit, by continuity, we would expect the smoothing of the honeycomb lattice to be more and more pronounced until diagonal degeneracy lines are found in the stability diagram. At order zero we would simply expect the high contrast modulation of the (molecular) degeneracy lines found in the weak coupling limit to be reduced gradually until flat molecular degeneracy lines are found for strong inter-dot tunnelling. During this evolution we would tend to believe that the periodic modulation along the molecular degeneracy lines remains unchanged, at that we simply lose track of the charge states of both dots when the amplitude of this modulation becomes to small. We illustrate this in figure 4.7. The point is that such a naïve extrapolation is wrong, in particular due to multilevel effects that one has to account for when the threshold $t_{dD} > \Delta E_{d(D)}$ is crossed. Contrary to the weak and strong limiting cases, in the intermediate regime the eigen molecular spectrum of the system cannot

be derived independently from the Coulomb repulsion contribution to the energy. As a consequence, we need to go beyond the semi-classical description ($\mu_{system}(N) = \mu_{classical} + \Delta E$) and work in a more general framework to understand transport in this situation.

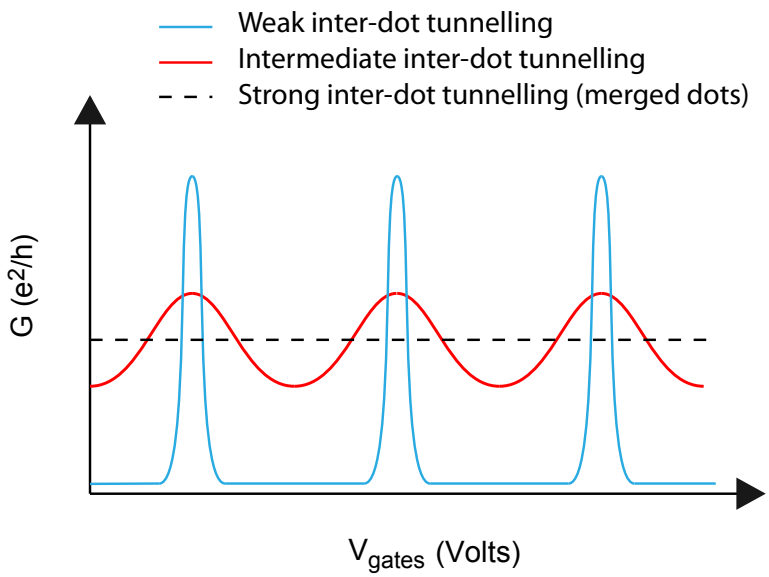

Figure 4.7: Schematic representation of the evolution the conductance pattern along a molecular degeneracy line from weak coupling (honeycomb) to strong coupling. From a naïve point of view we see that the amplitude of the modulation of the conductance is reduced as t_{dD} increases, though the periodicity is unchanged.

The study of transport will be done via exact diagonalization of a multi level interacting quantum dot Hamiltonian. We will present the hypothesis made to simplify the study and discuss the different steps of the calculation that enable us to calculate the conductance through the system as a function of the energy of both dots (plunger gates voltage) and the temperature of the leads. The different conductance maps obtained will be confronted to the experimental data to confirm our analysis.

4.1.3 Effect of cross talk

Before presenting a multi-level model describing our double quantum dot system, we would like to point out an important experimental issue that affects the conductance properties.
A very generic effect in lateral quantum dots and that influences the conductance maps is the cross talk effect. Due to capacitive coupling between the gates at the surface of the sample, moving the voltage on one gate always

affects the voltages on the surrounding gates. To obtain a stability diagram we sweep the plunger gate of each dot (V_{gd} and V_{gD}). Therefore we aim to incorporate in our analysis the cross talk between the plunger gates and the middle gates separating the dots and defining the inter-dot tunnel coupling (Fig 4.8). That way the tunnelling element will vary in both directions of the voltage gate space(Eq. 4.1).

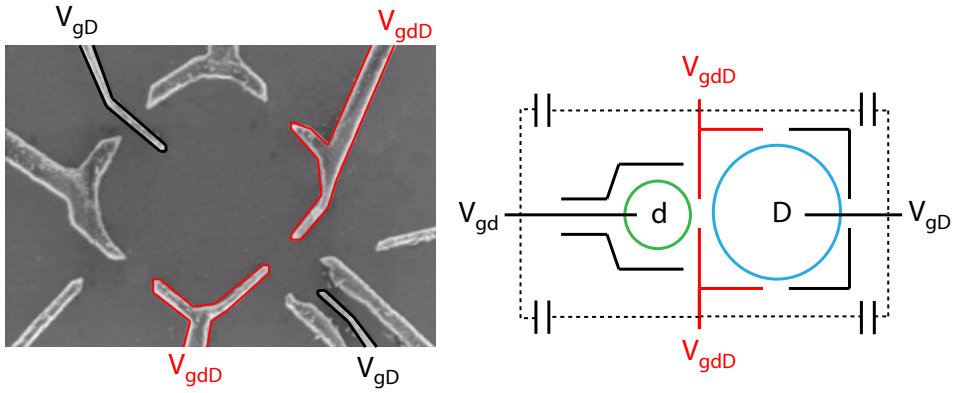

Figure 4.8: *Left panel.* SEM picture of the double dot device. The black gates correspond to the plunger gates that are swept to obtain a stability diagram. The red gates correspond to the middle gates separating the dots and defining the inter-dot tunnel coupling. *Right panel.* Scheme of the double dot device. The small dot and large dot appear as green and blue circles respectively. All the metal gates defining the dots in the 2DEG have been represented for clarity. Capacitors connect the plungers gates to the middle gates and lead to cross talk between them.

$$t_{dD} = t_0 + \alpha \times V_{gd} + \beta \times V_{gD} \tag{4.1}$$

The effect of cross talk is actually clearly seen in a larger stability diagram monitored at low temperature. Figure 4.9 displays large views (2D and 3D) of the low temperature diagrams previously shown in figures 4.2 and 4.3. We see in the 2D color plot of the top panel, that honeycomb cells are present in the left part of the diagram, whereas rather smooth lines are found from the center part to the right part. A continuous change from a double dot like regime to a single molecule like regime is observed with a cross over region around the center of the map where complex structures appear. We see that the inter-dot tunnel coupling increases when the small dot plunger gate voltage (V_{gd}) is made less negative, consistent with a cross talk effect. The 3D diagram in the bottom panel shows that in the V_{gD} direction the modulation presents also irregularities which can be attributed to cross talk induced by the large dot plunger gate.

Let us recall that the inter-dot tunnelling element t_{dD} determines the importance of the change in energy of the eigenstates of the system with respect to the pure small dot and large dot energy levels. By varying the tunnel coupling (Eq. 4.1), we directly affect the molecular energy spectra. We believe that a variation of the tunnel coupling within the diagram is a source of complexity and it will be taken into account in the numerical simulations.

Interestingly, from the diagram in figure 4.9, we can get lower limit for the tunnel coupling. It appears that on the bottom left corner of the diagram, honeycomb cells are present. From this diagram we can estimate t_{dD} and find a tunnel coupling of the order of 30-40 μeV in this parameter region. Due to cross talk, this value will increase when depolarizing the plunger gates, clearly pointing in the direction of a large tunnel coupling compared to the large dot level spacing, $t_{dD} > \Delta E_D$, at the center and right part of the stability diagram.

4.1.4 Multi level system approach

The Hamiltonian used to describe the system is shown in appendix A. This is a two impurity Anderson Hamiltonian widely used in the context of double quantum dots. To simplify our study of transport we make the following hypothesis:

- We consider that each dot holds three energy levels. Therefore the sums in H_d and H_D are carried from $i = 0$ to $i = 2$. The total double dot system will be able to hold up to 12 electrons. Note that these calculations are time consuming (30 hours per conductance map) and a finite number of states, that is to say a finite space in the energy diagram of the double dot is calculated.

- The different parameters entering the Hamiltonian in appendix A, that is to say the charging energies U_d, U_D, U_{dD} and the level spacings ΔE_d, ΔE_D are all estimated from experimental data taken on the double dot sample.

- We calculate the eigenstates of the isolated double dot, therefore the terms H_V and H_{band} are dropped in the Hamiltonian. The transport will be calculated at second order in the dot-leads coupling. Kondo physics cannot be accounted for in this context.

Mathematical procedure

We present here the different steps of the calculation. In order to extract the conductance through the double dot, we make use of the Meir-Wingreen

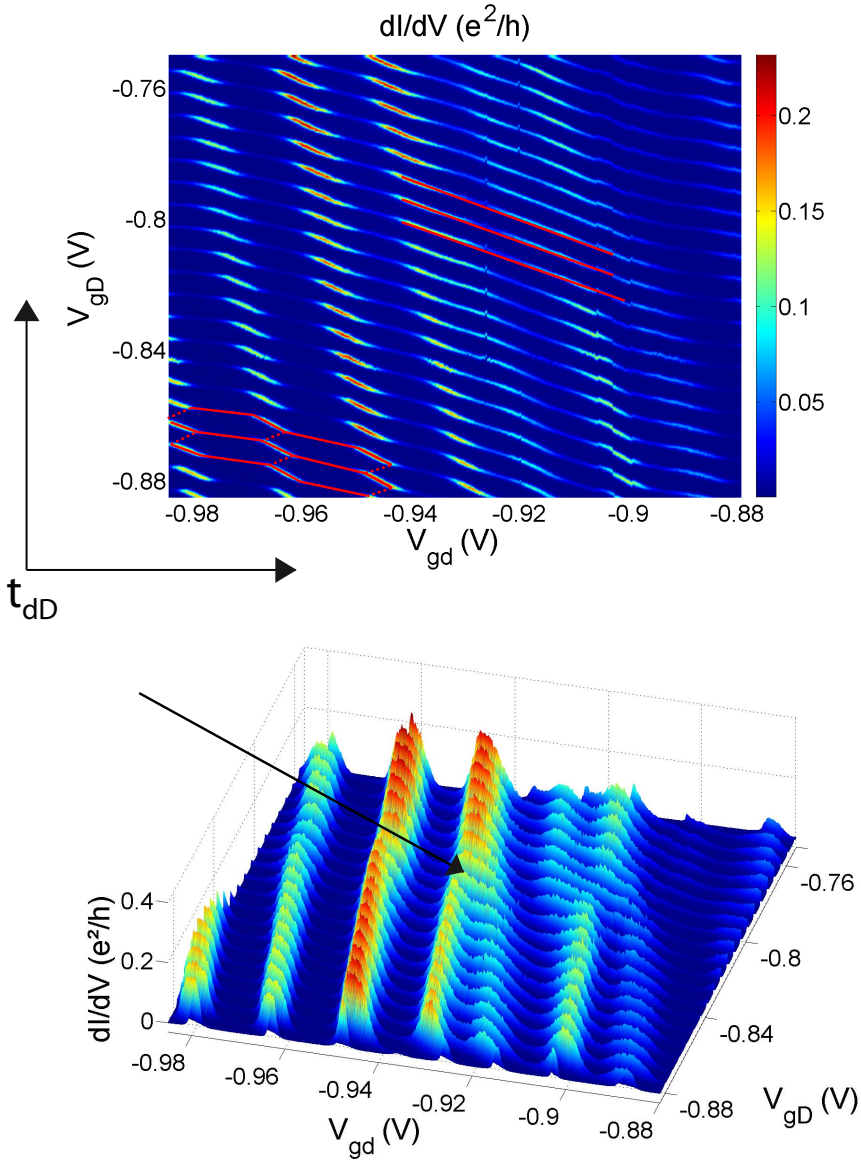

Figure 4.9: Larger view (2D and 3D) of the low temperature stability diagram shown in figures 4.2 and 4.3. *Top panel*: On the left part of the diagram we can identify honeycomb cells, whereas in the center and left part of the diagram the degeneracy lines follow smooth lines, with long linear domains. This effect can be attributed to cross talk induced by the small dot plunger gate V_{gd} mainly. *Bottom panel*: The three dimensional graphic shows in better details the complexity of the diagram. For example in the center of diagram indicated by a black arrow, two peak structures merge and on the right part a crossing seems to happen. We believe that the combination of cross talk induced by the two plunger gates, as indicated by the axis on the bottom left corner of the 2D diagram, can lead to such complex patterns.

formula [73] which relates G to the spectral function $A(\epsilon)$ of the system:

$$G = \frac{e^2}{h}\pi \int d\epsilon \frac{\partial f(\epsilon)}{\partial \epsilon} \mathrm{Tr}\left\{\mathbf{\Gamma}(\epsilon)\mathbf{A}(\epsilon)\right\} \tag{4.2}$$

where $f(\epsilon)$ denotes the Fermi-Dirac distribution in the leads, $\Gamma(\epsilon)$ represents the coupling of the small dot to the leads and $A(\epsilon)$ is the spectral function of system. Note that the couplings to right and left leads are supposed identical.
The spectral function $A(\epsilon)$ is a generalisation of the density of states when interactions are present [75]. Basically it gives the spectral weight related to the transition from a N particle state (of N particle molecular spectrum) of the system to a $N+1$ particle state (of a $N+1$ particle molecular spectrum) and takes into account electron-electron interactions and orbital effects. Due to the T-shape geometry, only the states holding weight within the small dot are considered to contribute to the spectral function that affects the conductance through the system(Eq. 4.2). Note that temperature effects are taken into account in the spectral function via statistical probabilities (Boltzmann type) that give the probability to occupy a given state at a given temperature. These probabilities will enable to activate high energy transitions which have low weight at low energy by increasing the temperature.

The calculations are performed as follows:

- The different eigenstates (molecular states) of the reduced Hamiltonian are calculated via exact diagonalization for N electrons, where N varies from 0 to 12.
- Once the N body molecular spectra are known, the transitions elements from a N particle state to a $N+1$ particle state are calculated at fixed temperature. These transitions will enable to calculate the degeneracy lines in the stability diagram from a Coulomb blockade valley with N electrons to a Coulomb blockade valley with $N+1$ electrons.
- The matrix $A(\epsilon)$ obtained is then incorporated in the Meir-Wingreen formula to extract the conductance through the system at a given temperature. Note that the Fermi distribution takes into account the broadening of the density of states in the leads with T, which in simple terms enlarges the conduction window through the device.

4.1.5 Numerical simulations

Note that all the different graphics are subject to boundary effects coming from the finite number of states considered. For example, on certain borders of the diagrams, the degeneracy lines of the system disappear. This

behaviour can be attributed to the fact that one dot is completely empty in that region and transition to the next electronic configuration would imply a negative occupation of that dot. Since these border effects do not describe physical effects we will not pay attention to them. The different energy scales used during the calculation are indicated at the top of each map and are expressed in meV. They follow the same notations used previously to describe the intrinsic energies of the double dot system. The tunnel coupling and cross talk effect are accounted via the law:

$$t_{dD} = 0.03 + (\epsilon_d + \epsilon_D) * 0.0011 \tag{4.3}$$

where ϵ_d and ϵ_D are the free parameters in the Hamiltonian of appendix A that enable to vary the dots energy. These parameters are by definition negative and enable to simulate the effect of the plunger gates. They are expressed in mV for that reason, however one cannot transpose ϵ to V_g directly as we will discuss on later. The choices of the different parameters in equation 4.3 were made by matching the intercept $t_0 = 0.03$ meV with the experimental estimations (see sec. 4.1.3) and by varying the slope $\Delta t/\Delta\epsilon$ until the numerical simulations managed to capture some conductance features seen in the low temperature experimental data (qualitative agreement when $\Delta t/\Delta\epsilon = 0.0011$ meV.mV^{-1} as we will see).

Low temperature results

Figure 4.10 shows a conductance map calculated in the regime $t_{dD} > k_B T$ where $T = 100mK$.
In the corresponding diagram the main features we observe are:

- The presence of honeycomb cells in the bottom left corner of the conductance where the tunnelling element is the smallest because of the cross talk applied in both voltage directions.
- On the right side of the diagram an apparent structure where two conductance peaks merge is observed.
- Globally, a rather complex conductance pattern is found is this temperature regime.

We believe that the complex conduction pattern captured via these calculations, reflect the complex molecular spectra formed in this particular tunnelling regime. At low temperature, we assume transport to involve a single resonant molecular state. Therefore we should be very sensitive to the nature of this molecular state (proportion of small dot versus large dot) and the way it connects to the leads. In other words, we are doing the spectroscopy of the molecular spectrum of the double dot device.
Notice that the relative voltage scans in the numerical simulations are smaller

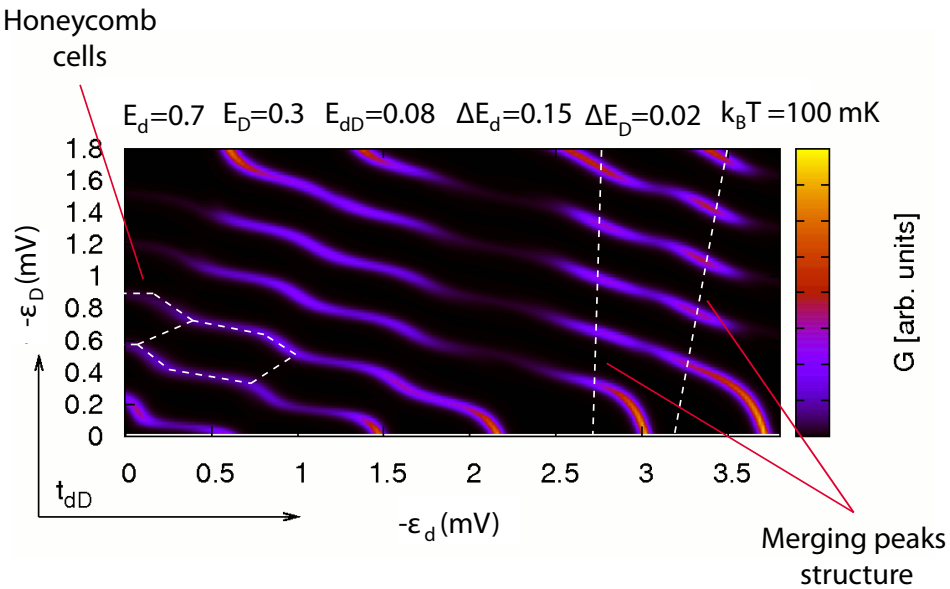

Figure 4.10: Low temperature, 100 mK, conductance map. Note the presence of honeycomb cells in the bottom left corner of the diagram and the presence of a structure where an apparent merging of two conductance peaks is seen.

than the experimental ones. ϵ_d and ϵ_D are expressed in voltages via a conversion factor that is the electron charge e. To match the experiments the conversion should also take into account the ratio between the plunger gate capacitance and the total capacitance of the corresponding dot. This ratio is always smaller than one which explains why the relative voltage scans appear to be larger in the experiments (see alpha factor, sec. 2.3.3).

High temperature results

Figure 4.11 shows a conductance map caculated in the regime $t_{dD} < k_B T$ where $T = 500mK$.
In the corresponding diagram the main features we observe are:

- All the degeneracy lines are subject to thermal broadening.
- The presence of cross talk is still seen in this conductance map where on the bottom left side we can identify broadened honeycomb cells and on the top right side we see rather linear degeneracy lines. This is consistent with the fact that cross talk does not depend on temperature.
- The modulation of the degeneracy lines follows a periodic pattern as indicated by the white dashed lines in both voltage directions. The

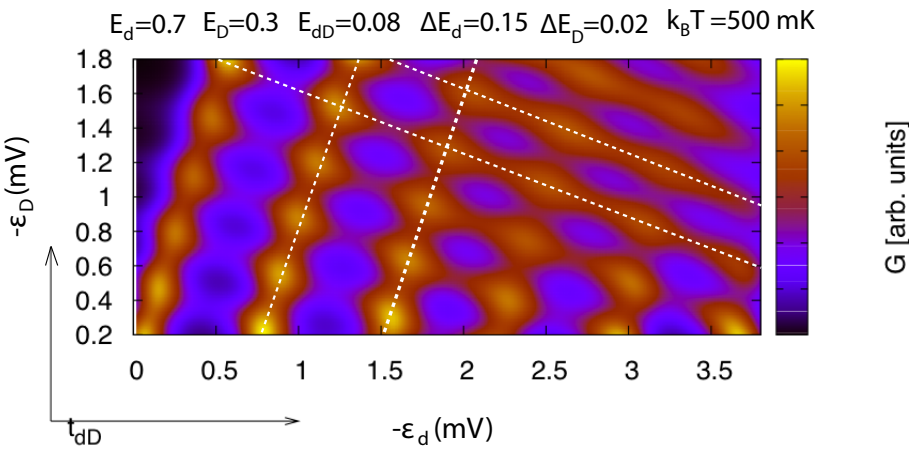

Figure 4.11: High temperature, 500 mK, conductance map. A regular conductance pattern is recovered. The modulation of the conductance following both voltage axis appears to be periodic, indicating a regular filling of the dots.

reminiscence of small dot and large dot charge states can now be conciliated with constant addition energies for both dots.

In the high temperature limit, $T >> t_{dD}$, we expect that due to the broadening of the Fermi distribution within the leads, at resonance we now have several molecular states available for transport[7]. Therefore the bonding and anti bonding states now contribute equally to transport which washes out the effect of t_{dD}. As we can see, this leads to a rather regular conductance pattern subject to thermal broadening. Another way to think of the device, is to identify it as a small dot connected to metallic leads and coupled incoherently with a large dot. The molecular waves that spread through the double dot at low temperature effectively lose there coherence at high temperature and one recovers the small dot and large dot wave functions as a result. The large dot acts simply as a charge reservoirs and we recover a modulation of the conductance on the degeneracy lines of the system that keeps track of a regular filling of the small dot and the large dot in the ϵ_d and ϵ_D directions respectively.
Interestingly an analogy with single quantum dots can be made. At low temperature $k_BT < \Delta E$, a single resonant state contributes to transport through the device. As a result a series of Coulomb blockade peaks with different amplitudes is found and illustrates the unicity of each charge state (Chap 2., sec. 2.3.4). At higher temperature, $k_BT > \Delta E$, several states contribute to the current at resonance. As a result, enlarged Coulomb peaks

[7]Remember we are always in the single electron tunnelling regime

are observed in transport with an almost identical amplitude. This is understood as an averaging of the current of several states which on long time scales (acquisition time scales), washes out the random variation of the amplitude of the Coulomb peaks.

4.1.6 Cross talk between the plunger gates

If we compare the high temperature experimental data 4.2 (bottom panel) and numerical data 4.11 we can see that the reminiscence of the small dot charge states (high conductance) follows tilted periodicity lines. However the slopes found in the experiments and the numerical simulations do not agree.

Numerical simulations

It appears that the slopes found in the numerical simulations can be attributed to the particular form of the Hamiltonian in appendix A and the role played by ϵ_d and ϵ_D. These free parameters used to vary dot d in H_d and dot D in H_D, actually do not vary the energy of the dots independently when both terms are added with the interaction term H_{dD} in the complete Hamiltonian. Therefore the degeneracy lines of the system appear to be tilted since the energy of both dots is changed when a single ϵ parameter is moved.

Experiments

In the experiments, the conductance maps are plotted as a function of the plunger gate voltage. To understand the effect of these voltages, equation 2.18 is a good illustration. Due to the particular form of each interaction term, it appears that one can compensate a shift in n_d by a shift in V_{gd}, and a shift in n_D by a shift in V_{gD}, independently of each other. As a result, the periodicity lines indicating the position of the small dot charge states are expected to be vertical (Fig. 2.9).
Strictly speaking we would expect to see the behaviour in the experimental data. However an experimental issue, the cross talk between the plunger gates of both dots, explains the deviation of the periodicity lines from vertical lines. When the voltage on one plunger gate is increased, due to cross talk, the plunger gate of the other is increased by a smaller amount. This effect tends to give the slope the periodicity lines follow in the experiment. It appears that this effect dominates the effect of the mutual charging energy in our experiments. However this type of cross talk is not relevant in our analysis since it does not affect the tunnel coupling.

To summarize, the (ϵ_d, ϵ_D) and (V_{gd}, V_{gD}) spaces are not equivalent but

are related. Work still under progress aims to express the numerical data in terms of the plunger gate voltages.

4.1.7 Effect of hybridisation with the leads

So far we did not discuss the effect of hybridisation with the leads. The difficulty of treating this coupling is that one can no more perform exact diagonalizations of the complete Hamiltonian shown in Annex A. More sophisticated methods such as NRG calculations are required in order to extract the relevant mechanisms leading to transport at low energies. These methods are extremely time consuming and before treating the effect of hybridisation with the leads our choice was to account for transport in a simpler framework. Indeed we saw that by considering the molecular eigenstates of the system we succeeded to capture physics in the low temperature regime, and also incorporated naturally the effect of temperature via the number of molecular states participating to transport.
However the question of non negligible $\Gamma_{dot-leads}$ remains open and in particular the possibility of Kondo mechanisms at low temperature. Due to the complex conductance pattern seen at low temperature, we did not investigate yet such mechanisms that we assume to be difficult to extract due to the irregularities present in the conductance diagram.
We will see in the following experiment, a regime where inter-dot tunnel coupling and strong coupling to the leads have to be considered in order to account for the low temperature transport mechanisms.

4.2 Kondo effect on an orbital degeneracy point

In the following experiment we will focus on the orbital degeneracy point of the dots (Fig. 4.12, red line). By orbital degeneracy of the dots, we mean that the electrochemical potentials of each dot are degenerated (dot-Dot degeneracy), leading to charge fluctuations between them (see Chap. 2, sec. 2.4.2). This situation is met in a honeycomb diagram on the red dashed line depicted in figure 4.12.

4.2.1 Low temperature stability diagram

The starting point is a stability diagram of the double dot taken at low temperature, 30 mK, in a regime where the coupling to the leads (small dot-leads) and between the dots have been increased compared to the weak coupling limit already addressed earlier (Chap. 2, sec. 2.4.3, Chap. 4, sec 4.1.2).
Figure 4.13 shows two stability diagrams where the bottom one corresponds to the weak coupling regime and will serve as a reference and the top diagram

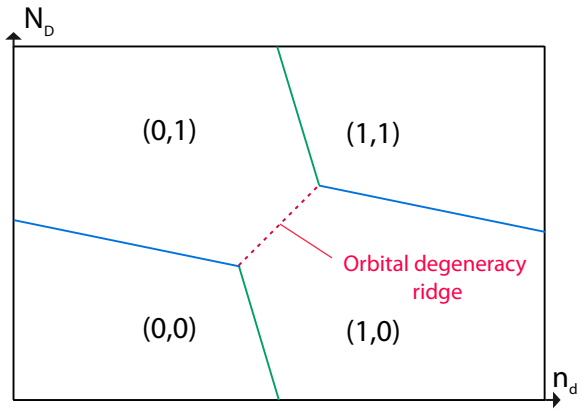

Figure 4.12: Scheme of a part of a honeycomb diagram. n_d and N_D represent the occupation numbers of the small and large dot respectively. Red dashed line : orbital degeneracy line. Blue line: large dot degeneracy line. Green line: small dot degeneracy line.

corresponds to the situation where the tunnel couplings are stronger. A few remarks can be made at this stage:

- *Leads-dot coupling.* In the bottom diagram of figure 4.13 the degeneracy lines appear as very fine lines and the conductance in the valleys of the honeycomb cells is of the order of $10^{-4}\frac{e^2}{h}$[8], which corresponds to our noise detection level. This regime is a very well defined Coulomb blockade regime, $h\Gamma \lesssim k_BT < \Delta E, E_C$ [32], and was already describe in the framework of weak couplings in chapter 2. In the top diagram the degeneracy lines present important Γ broadening, that is to say they are enlarged due to hybridisation with the leads, $h\Gamma > k_BT$, and the conductance in the valleys is greatly enhanced : $\sim 0.1\frac{e^2}{h}$, again suggesting Γ broadening and also cotunnelling processes participating to transport (Chap.2, sec. 2.5).

- *dot-Dot coupling.* The bottom diagram differs very weakly from a pure honeycomb diagram. The impact of tunnelling between the dots is mainly seen at the triple points where the lines are slightly smoothed and where the effect of tunnelling between the dots is expected to be the largest (Chap. 2, sec. 2.4.3). In the top diagram, the effect of tunnelling does not limit itself to the triple points and extends further on the degeneracy lines. The entire honeycomb structure is distorted and the presence of large conductance on the degeneracy lines associated to the large dot, suggest stronger mixing of the wave functions, thereby stronger inter-dot tunnel coupling.

[8]The color code of the diagram has been offset in order to reveal the degeneracy lines of the large dot that present very low conductance actually slightly above the noise level.

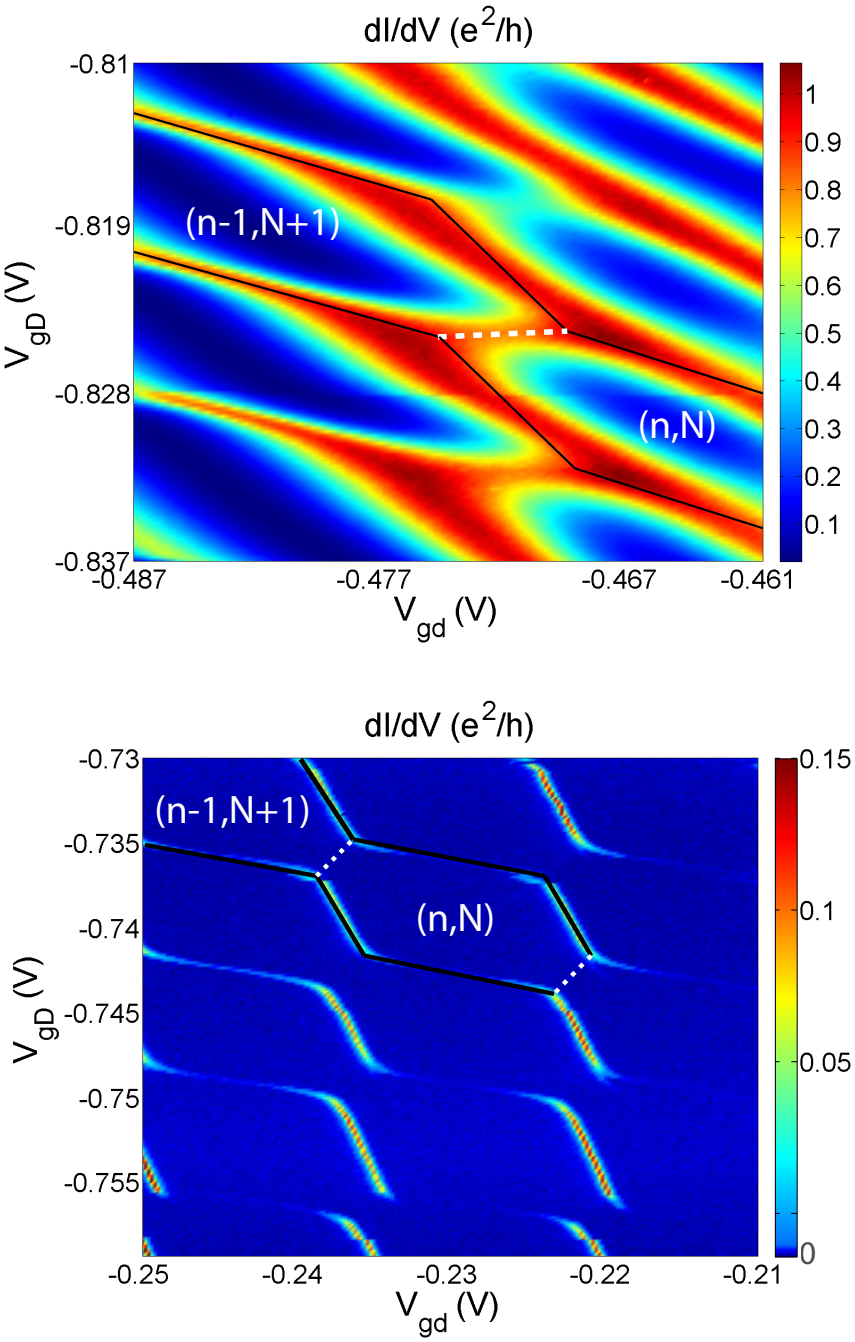

Figure 4.13: *Top diagram.* Low temperature (30 mK) stability diagram with important coupling to the leads seen in the Γ broadening of the degeneracy lines and the enhanced conductance in the Coulomb valleys ($\sim 0.1\frac{e^2}{h}$). Note that the effect of inter-dot tunnel coupling is seen in the smoothing of the underlying honeycomb diagram. Unusual feature : the orbital degeneracy ridge of the dots, indicated with a white dashed line, presents very high conductance, of the order of $\frac{e^2}{h}$. *Bottom diagram.* Reference diagram taken also at low temperature (30 mK), in the weak coupling limit to the leads and between the dots. The important point is the absence of conductance on the orbital degeneracy lines, where the system is blocked via the mutual charging energy of the dots (U_{dD}) as expected.

- *dot-Dot degeneracy line* We see the appearance of conductance on the orbital degeneracy line of the dots (Fig. 4.13, white dashed lines) in the top diagram whereas the system is completely blocked in the weak coupling situation as expected. Moreover the conductance on these degeneracy lines is very high, since it reaches almost the quantum of conductance, $\sim \frac{e^2}{h}$.

The question of how the enhancement of the inter-dot tunnel coupling and the dot-leads coupling results in strong conductance at low temperature on the orbital degeneracy ridge of the dots, arises. More precisely, which mechanism reestablishes transport on a degeneracy ridge where we expect the system to be blocked via the mutual charging energy of the double dot, U_{dD}[9]. As we will see in the following, we can relate transport on this ridge to Kondo physics. In order to determine the different energy scales entering the problem and to describe the Kondo mechanism on the ridge we will first try and describe the system in the framework of a two level system. Experimental data will help us to test this simple approach. We will close our analysis on possible scenarios that enable us to solve theoretical issues of the two level model. In particular, a multi level approach supported by NRG calculations currently running, will be discussed.

4.2.2 Kondo signatures

Evolution in temperature

We study the evolution of the stability diagram as a function of temperature. We therefore vary the temperature of the sample from 30 mK to 440 mK and for each temperature we monitor the same stability diagram. Figure 4.14 (top panel) shows a high temperature limit diagram monitored at 320 mK and the evolution of an entire dot-Dot ridge at all the temperatures we studied (bottom panel). Despite the general thermal broadening of the degeneracy lines expected from the broadening of the Fermi-Dirac spectral density in the metallic leads, the notable feature is the disappearance of conductance on the orbital degeneracy line at high temperature. It is actually not straightforward to position the ridge and a guide to the eye has been added in the top panel of figure 4.14 (white dashed line) to show its position. A more detailed analysis of the evolution of the ridge within temperature is shown in the bottom panel of Figure 4.14. The two peak structures present a high and low temperature corresponds to triple points of the stability diagram separated by the ridge under consideration. Each curve was extracted from a stability diagram monitored at constant temperature. The waterfall formed by all the curves shows a symmetric behaviour with respect to the center of the ridge and one can notice that the conductance drops faster at

[9] We changed notation here concerning the mutual charging energy. We will keep the notation U_{dD} in the following

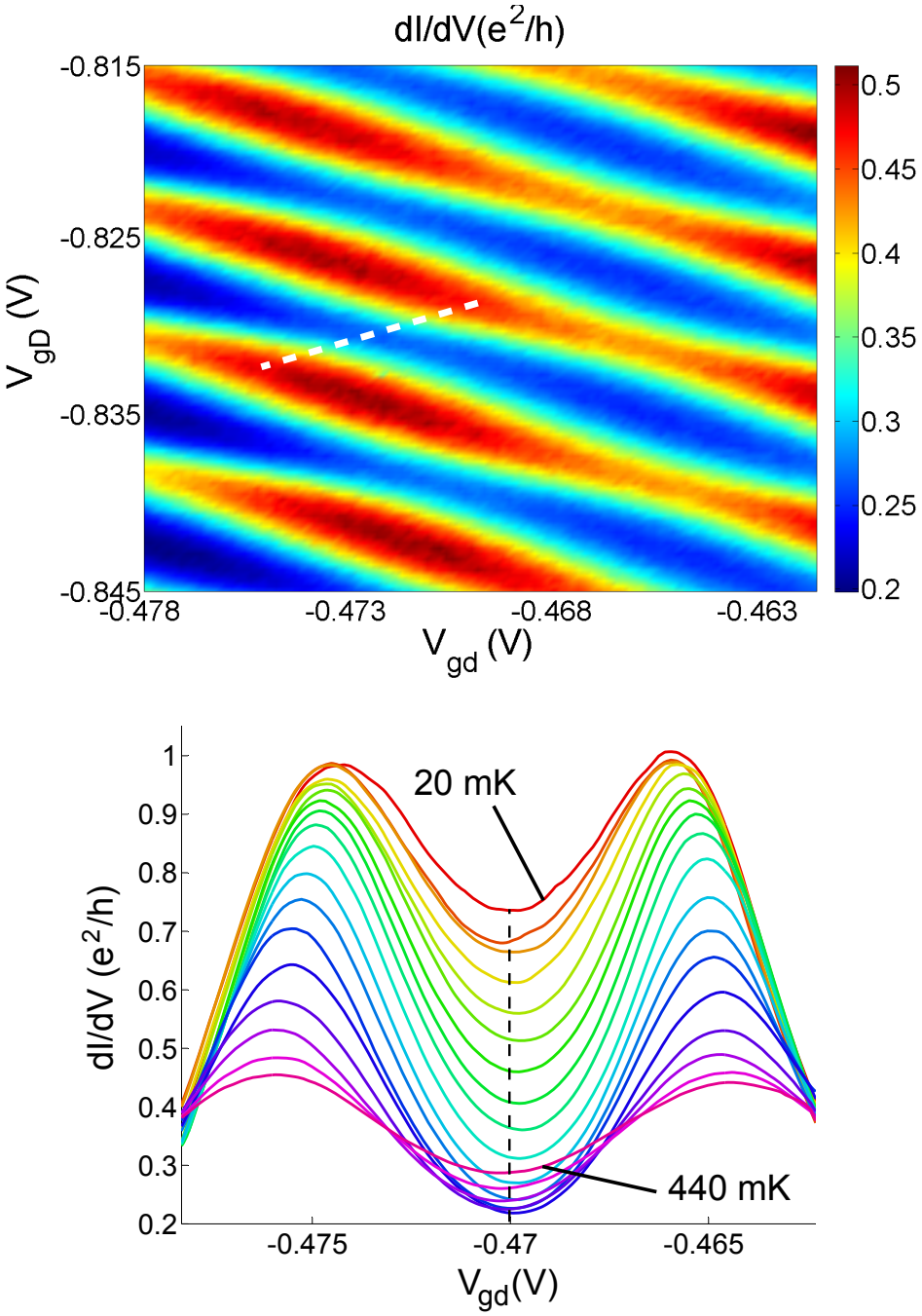

Figure 4.14: *Top panel.* High temperature (320 mK) stability diagram corresponding to a close up view around a the orbital degeneracy ridges monitored at low temperature (Fig 4.13) . The position of the ridge is indicated with a dashed white line, however the ridge is almost indistinguishable at this temperature. *Bottom panel.* An orbital degeneracy ridge extracted from the stability diagrams at all the temperatures studied between 30 mK and 440 mK. Note that the abscissa axis is actually the composition of two gate voltage scans. For simplicity we only expressed V_{gd} on the graphic, however this does not correspond to a projection.

that center than near the triple points.
We can summarize briefly the behaviour in temperature by the three following points:

- When the temperature increases the conductance on the ridge drops, that is to say the mechanism that leads to high conductance at low temperature is destroyed at high temperature
- More precisely, the conductance at the center of the ridge drops faster when temperature increases than near the triple points with a quite symmetric behaviour with respect to the center.
- The peak structures that we identify with the triple points move closer to each other as the temperature is decreased.

We know from theory that a possible mechanism leading to strong conductance at low temperature in a Coulomb blockade valley of a quantum dot and destroyed at higher temperature, is the Kondo effect.

- Our first observation, that is to say in the valleys separating two triple points, Coulomb blockade is lifted at low temperature and a high conductance ridge appears, is consistent with Kondo effect in quantum dots. Note on this ridge the relevant charging energy is the mutual or molecular charging energy U_{dD}.
- Our second observation can be analysed by taking advantage of the Haldane formula of the Kondo temperature in the Anderson model (Chap 2.6.3, 2.44). This formula states that the Kondo temperature is maximal when $\epsilon = 0$ or $\epsilon = -U$, that is to say on the Coulomb peaks. Even though this formula is actually not valid close to the Coulomb peaks[10], the profile of the Kondo temperature versus detuning (in practice gate voltage) around the center of the Coulomb blockade valley follows the Haldane formula. We therefore expect the Kondo temperature to increase when we move near the charge degeneracy peaks. The fact that conductance drops faster at the center of the orbital ridge is consistent with a smaller Kondo temperature than near the triple points. Going back to Haldane's formula we see that the profile of the Kondo temperature is symmetric around the position $\epsilon = -U/2$, that is to say the center of the valley. This agrees with the symmetric behaviour in gate voltage the waterfall shows.
- Our last observation concerning the position of the triple points as a function of temperature has already been reported in the context of Kondo physics in single quantum dots [65].

[10] Close to the Coulomb peaks we enter the so called mix valence regime [76]

We can now try and go beyond this qualitative analysis. We know in the framework of the standard Kondo model, that the conductance in a Coulomb blockade valley undergoing the Kondo effect, follows a universal T dependence. Although this law is given via numerical calculations, an empirical formula deviating weakly from the numerical function exists and was proposed by Goldhaber-Gordon [76]:

$$G(T) - G_{background} = G_0 \left(\frac{{T'_K}^2}{T^2 + {T'_K}^2} \right)^s \tag{4.4}$$

with $T'_K = T_K / \sqrt{2^{\frac{1}{s}} - 1}$ where the fit parameter $s \simeq 0.22$ for a spin-1/2 system. G_0 corresponds to the saturation value of the conductance at low temperature ($T << T_K$), $G_{background}$ is a possible conductance background offsetting the whole curve and T_K is the Kondo temperature.

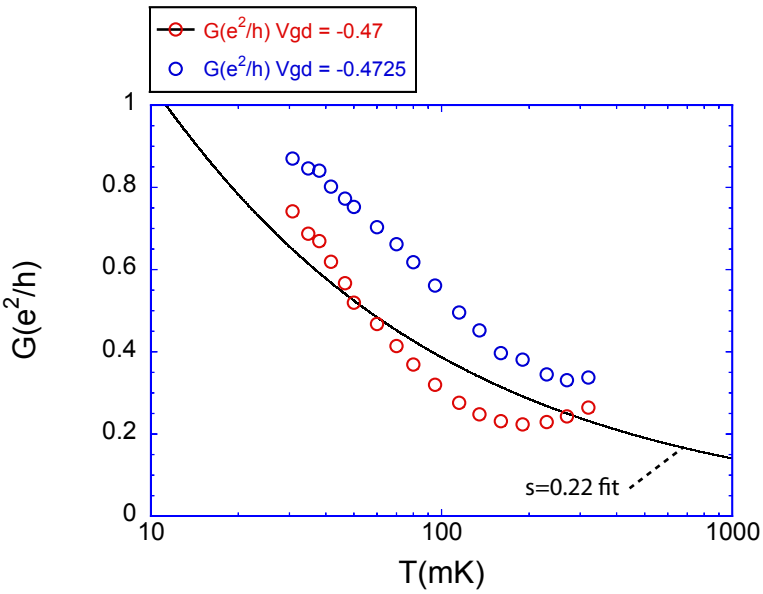

Figure 4.15: Conductance versus temperature on the orbital degeneracy ridge for two different gate voltages in figure 4.14. Red circles correspond to a cut in the middle of the ridge. Blue circles correspond to a cut on the left side of the ridge.The black curve is a fit to the red circles using equation 4.4 with T_K and G_0 as free parameters.

We apply this fit to a cut performed at the center of the waterfall curves (Fig. 4.14, black dashed line) at $V_{gd} = -0.47V$ and use T_K and G_0 as free parameters. The result of the fitting is depicted in figure 4.15, where the red circles correspond to the experimental data that we fit with the black curve, being the empirical fit, Eq. 4.4. Even though the fit agrees with an enhancement of the conductance when the temperature decreases, it fails to

reproduce properly the experimental data which appear to follow a steeper temperature dependence.
For the moment, we conclude that the temperature behaviour of the conductance on the orbital ridge is not consistent with a standard Kondo scaling law. To make sure we are dealing with Kondo processes, non linear transport experiments are required.

Non linear transport measurement

Another feature of the Kondo effect that we can test is the behaviour of the system when a finite voltage bias is applied across the leads. In the Kondo effect, a Kondo resonance is formed at low temperature, and shows as peak in the local density of states locked at the Fermi energy (in practice zero bias). In non linear transport measurements this peak is seen as a zero bias anomaly (Chap. 2, sec. 2.6). Since we expect the Kondo resonance to extend on the entire Coulomb blockade valley where the local moment is defined, we expect to detect a ZBA for any gate voltage corresponding to this blockade valley. Experiments have already reported this behaviour in several devices such as single dots or carbon nanotubes [77], where a fine line of conductance locked at zero bias is visible within Coulomb diamonds (Coulomb diamonds colour plots, Chap 2) where a local magnetic moment is confined (odd occupancy of the quantum dot).
The experiment we perform in the following is a gate voltage scan (V_{gd}+V_{gD}) that follows the orbital degeneracy ridge, where the bias voltage is swept at each gate voltage point (see Fig. 4.16) as one would do in a usual Coulomb diamond experiment in single quantum dots (see Chap. 2, sec. 2.3.5).

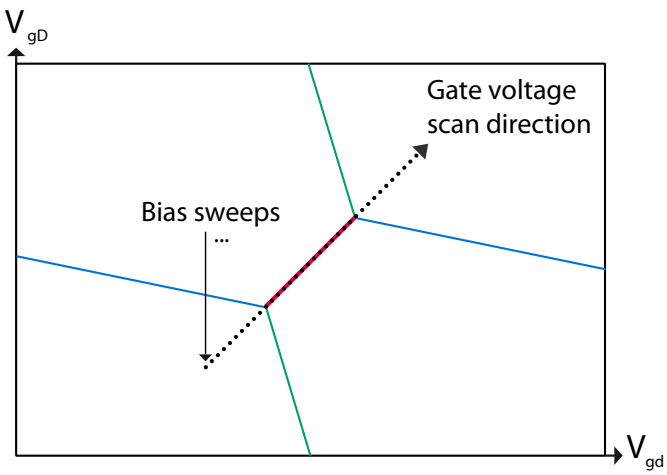

Figure 4.16: Voltage scan direction follows the degeneracy line (dotted black arrow). At each voltage point in the (V_{gd}, V_{gD}) space the voltage bias across the dot is swept.

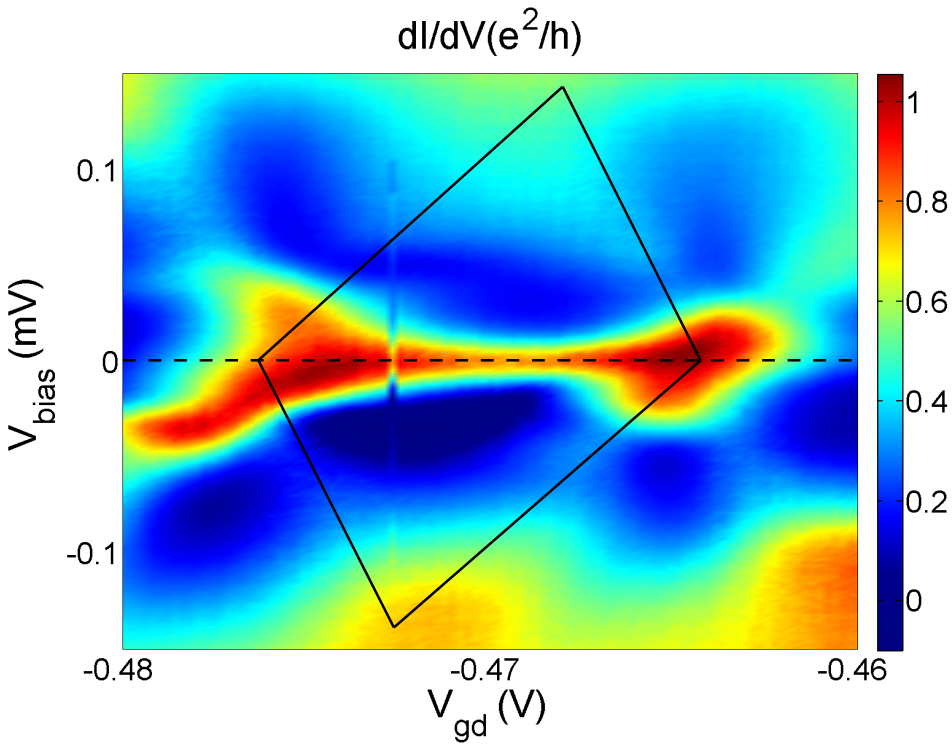

Figure 4.17: Non linear transport experiments performed along the orbital degeneracy line. The black lines are guide to the eyes showing the underlying diamond shape expected. The abscissa corresponds to a scan involving V_{gd} and V_{gD}. For clarity only V_{gd} is expressed. A clear zero bias anomaly is present at the center of the diamond.

The resulting diagram is shown in figure 4.17:

- Even though the structures present in the spectroscopy are subject to important Γ broadening, it seems that a diamond shape can be guessed (indicated for clarity in Fig. 4.17). As in the case of Coulomb diamond experiments performed in single quantum dots, we are testing the variation of the addition energy of an electron in the system as a function of the position along the orbital ridge. In other words, we are analysing the energy position of the electrochemical potential of the double dot molecule for the addition of an electron with respect to the Fermi energy of the leads. It appears from the diamond shape that analogy with single quantum dots spectroscopy experiments can be made (Chap. 2, sec. 2.3.5). Due to the important coupling to the leads, the degeneracy lines forming the diamond are broadened and a guide to the eye indicates the diamond for clarity. Note that the degeneracy points of the diamond on the zero bias axis correspond to the positions of the triple points where we see large structures with

high conductance.

- Concerning the hight of the diamond, one can relate it to the addition energy. In the constant interaction model one can express it as the sum of an electrostatic contribution describing the Coulomb interaction and an orbital contribution (Chap 2., sec 2.3.3). We find here $E_{add} \sim 130\mu eV$. At the center of the orbital ridge, we expect from the underlying honeycomb pattern that the relevant Coulomb energy is the mutual charging energy U_{dD}. Concerning the orbital contribution, we know from our two level system that the tunnel coupling reduces the energy of the molecular ground state by an amount t_{dD}. By analogy with the constant interaction model we would tend to say that $E_{add} = U_{dD} + t_{dD} \sim 130\mu eV$. However precautions should be taken before making such assumptions. Indeed, when the bias voltage is raised, and due to capacitive coupling between the lead and the device, an arm lever will raise the energy levels of the device. From the T shape geometry, it is legitimate to believe that the energy levels of the small dot will be more affected by the arm level than the levels of the large dot. Therefore at high bias one should also account for detuning between the dot energy levels, which inevitably changes the nature and the position of the energy levels of the molecular states. This will affect the expression of the addition energy.
  Our aim here is to get a qualitative description using a simple model. NRG calculations should help us later to get a more quantitative understanding.

- The most striking feature in this diagram is the presence of a line locked at zero bias, joining the triple points and presenting strong conductance, $\sim \frac{e^2}{h}$. From this line we conclude that the conductance on the orbital degeneracy ridge is locked at zero bias, in other words is a zero bias anomaly (ZBA) in agreement with a Kondo mechanism probed in transport. Applying a finite bias destroys the Kondo resonance, which shows up as a drastic decrease of the differential conductance away from the zero bias line in the diagram.

From the FWHM of the ZBA at the center of the diamond, we can get an estimation of the Kondo temperature as mentioned earlier. At the position V_{gd}=-0.47 V, we perform a cut in the diagram and fit the peak locked at zero bias with a Lorentzian function of the form:

$$G(V_{bias}) = G_0 \frac{{T_K}^2}{\left(\frac{T_K}{2}\right)^2 + (V_{bias})^2} \tag{4.5}$$

where T_K is the Kondo temperature and represents the Full Width Half Maximum (FWHM) of the Lorentzian. Note that T_K and V_{bias} are assumed to be expressed already in energy units (μeV in our case), therefore the

proportional factors (k_B and e) have been dropped in the equation. G_0 enables to adjust the amplitude of the peak. Figure 4.18 shows the fitted peak, leading to FWHM of $\sim 20\mu eV \leftrightarrow 200mK$, where T_K and G_0 are used as free parameters. From the temperature behaviour of the conductance in the middle of the ridge shown in figure 4.15 we know that even at the lowest experimental temperature, the system is not yet in the unitary limit. Therefore one cannot associate the FWHM found, to the Kondo temperature of the system at the center of the ridge (V_{gd}=-0.47 V). Earlier experiments performed in semiconductor quantum dots have shown that the ZBA anomaly in the Kondo regime is thermally broadened (with a linear dependence) when the system exits the unitary regime [65]. We conclude that the FWHM extracted from the fit is an upper limit of the Kondo temperature of the system. We estimate T_K to be of the order of 100 mK.

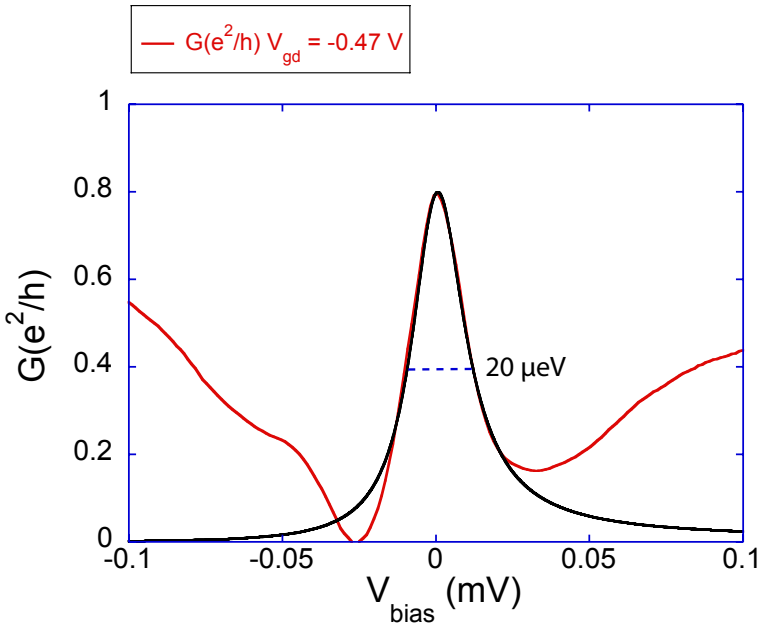

Figure 4.18: Zero bias anomaly extracted from the non linear transport diagram at V_{gd}=-0.47 V. A fit using a lorentzian function gives a FWHM of 10 μeV which gives us an estimate of the Kondo temperature at the center of the diamond.

4.2.3 Two level system approach

In order to understand the Kondo mechanism leading to transport at low temperature on the orbital degeneracy ridge, we start with a simple two level system approach, where each dot is assigned with a single level. Our

aim is to identify the degree of freedom involved in the Kondo process by use of a simple model[11].
We already used a two level system description earlier (Chap.4, sec 4.1.2), where we only consider the topmost occupied level in each dot. In order to take into account electron-electron interactions, we make use of the constant interaction model which absorbs lower occupied energy states in a mean field Coulomb repulsion term. This approach enabled us to account for the honeycomb diagrams in capacitively coupled dots (Chap 2, sec. 2.4.2). Moreover we assume that at low temperature, only the ground state of the system is probed in linear transport and therefore excited states will not play a role. In the following we are going to discuss the effect of inter-dot tunnelling and hybridisation of the system with the leads.

Inter-dot tunnel coupling

inter-dot tunnel coupling was already addressed in a two level system holding a single electron (Chap 2, Chap 4) and led to the formation of a set of two molecular states, the bonding and anti bonding state. We follow this description and take into account the Coulomb repulsion term
On the orbital degeneracy ridge, the energetic configuration of the double dot is the following : the levels of each dot are degenerated and lie below the Fermi energy of the leads. Figure 4.19 shows the energy landscape of the double dot system and leads, at the center of the degeneracy ridge according to this simplified model.
The independent levels, d and D (for small dot and large dot), are situated at an energy $\epsilon = -\frac{U_{dD}}{2}$ (E_F is taken as the reference). The tunnel coupling creates an anti-crossing of the levels, with the formation of molecular states, B and A (for bonding and anti bonding), separated in energy by $2t_{dD}$. The electron in the system then occupies the bonding state, that is to say the ground state. The addition of the second electron is blocked by the inter-dot Coulomb repulsion term U_{dD}.
It is straightforward to see that the system acts here as a spin $\frac{1}{2}$ magnetic impurity. By analogy with a single quantum dot, it is legitimate to believe that the system can undergo a spin Kondo effect.

Coupling with the leads

So far we treated the double dot as isolated and considered the molecular eigenstates formed between the dots in order to show that the system can act as a magnetic impurity. In order to undergo the Kondo effect, the impurity has to couple to electronic reservoirs to be able to form a delocalized singlet "impurity-leads" at low temperature. Strictly speaking, for non negligible coupling with the leads we should not consider to the eigenstates of the

[11] Strictly speaking the Kondo effect does not restrict to the spin degree of freedom

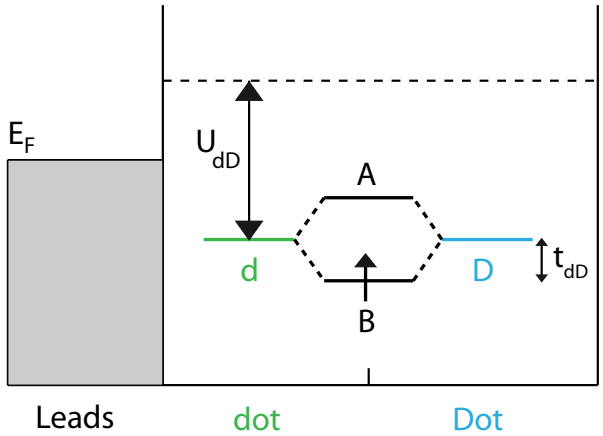

Figure 4.19: Energetic configuration of the double dot at the center of the orbital degeneracy ridge. The independent levels d and D, that is to say without tunnel coupling are represented in green and blue respectively. To first order transport is blocked via the mutual charging energy U_{dD}. For finite inter-dot coupling, molecular states B and A are formed in the double dot system. The degeneracy is lifted via the tunnelling element, leading to a gap $2t_{dD}$ between the molecular states. In the ground state, the single electron occupies the bonding state (B).

system to be those given by the isolated double dot. For simplicity we stay in the framework of the molecular basis considered above in order to apprehend the Kondo mechanism in our device. For strong coupling with the leads we can expect the system to undergo the Kondo effect as depicted in figure 4.20, with a Kondo temperature given by:

$$T_K \simeq \frac{\sqrt{\Gamma U_{dD}}}{2} \exp\left(\frac{\pi\epsilon(\epsilon + U_{dD})}{\Gamma U_{dD}}\right) \tag{4.6}$$

where U_{dD} is the mutual charging energy of the double dot, $\epsilon = E_F - \epsilon_d - \epsilon_D$ is the detuning parameter. Γ is the coupling of the small dot to the leads (T shape geometry). Interestingly, due to the mixing of the wave functions in the molecular eigenstates (Eq 4.7, d is small dot, D large dot), they will always be a finite proportion of the small dot in the total wave function of the ground state of the system.

$$\begin{aligned} | A > &= cos\frac{\vartheta}{2} | \varphi_d > + sin\frac{\vartheta}{2} | \varphi_D > \\ | B > &= -sin\frac{\vartheta}{2} | \varphi_d > + cos\frac{\vartheta}{2} | \varphi_D > \end{aligned} \tag{4.7}$$

In other words, in the molecular basis we are considering that the system can always undergo the Kondo effect with a effective coupling Γ that will

vary as a function of the proportion of the small dot wave function in the molecular basis. The more weight in the small dot the molecular state will have and the better coupling to the leads the total wave function will have. We will refer now to Γ as Γ_d (d for small dot).

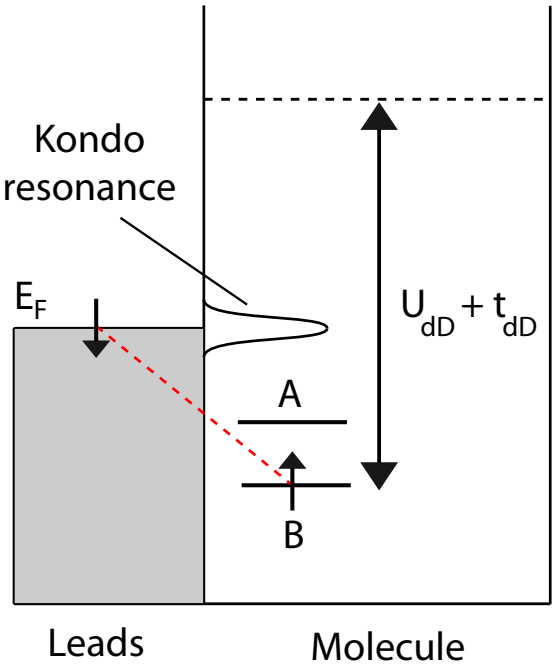

Figure 4.20: Kondo resonance formed in the double dot system at low temperature. Due to the mutual charging energy of the system, transport is blocked to first order and a magnetic impurity is stabilized at high temperature. For low enough temperature ($< T_K$), the electron in the ground state (bonding state) entangles with conduction electrons in the leads via a Kondo mechanism to form a singlet. A Kondo resonance locked at the Fermi energy is seen in transport, illustrating the excitations of the Kondo state.

This simple model is in qualitative agreement with the low temperature behaviour of conductance on the orbital ridge (yet not the scaling law within temperature), and the zero bias anomaly observed in non linear transport along the ridge. However we need to understand why evidences of Kondo physics is found only on this particular ridge. One could argue that an orbital degeneracy could lead to an orbital Kondo effect and therefore display orbital Kondo physics only on the ridge we are studying. Indeed the Kondo mechanism does not only apply to spin degree of freedom [78] [7]. Generally speaking the Kondo process requires a degenerated ground state, and conservation of the quantum number related to the degeneracy during the tunnel process to (from) the leads. For lateral quantum dots, the orbital de-

gree of freedom is not conserved during the tunnelling process since it does not exist in the leads. We can therefore rule out the orbital Kondo effect in our device. A spin Kondo effect appears to be a more reliable scenario. The point is that if we take a look at the diagram depicted in figure 4.12, on both sides of the orbital ridge there is a magnetic configuration since we have a single electron in the device. Then why do we only detect Kondo physics on the ridge and not in the surrounding blockade valleys. Our argument stands on the variation of the Kondo temperature around the orbital degeneracy.

4.2.4 Boosting the Kondo temperature

Variation of the charging energy

If we take a look back to figure 2.9 where schematic stability diagrams of a double dot are represented, we notice that the charging energy of the system is not constant in a honeycomb cell (the different ΔV_g depend on different charging energies). In the middle of a honeycomb cell, the blockade is dominated by the renormalized charging energies of each dot, U_d and U_D, whereas in the vicinity of the orbital degeneracy ridge the blockade is fixed by the mutual charging energy U_{dD}. In our system, since $U_d > U_D > U_{dD}$, the global charging energy of the system will be reduced by moving towards the orbital degeneracy ridge. This simple remark is of importance in the regime we are focusing on.
We recall the Haldane formula of the Kondo temperature (Eq. 4.8). Note that now the charging energy depends on the voltages applied on the gates.

$$T_K \simeq \frac{\sqrt{\Gamma_d U(V_{gd}, V_{gD})}}{2} \exp\left(\frac{\pi\epsilon(\epsilon + U(V_{gd}, V_{gD}))}{\Gamma_d U(V_{gd}, V_{gD})}\right) \tag{4.8}$$

Where Γ_d is the coupling to the leads, ϵ the detuning parameter or the relative position of the molecular level with respect to the Fermi energy and $U(V_{gd}, V_{gD})$ the charging energy of the system depending on the position in the honeycomb diagram we are considering. At the center of a Coulomb blockade valley, that is to say $\epsilon = -\frac{U(V_{gd},V_{gD})}{2}$ we find:

$$T_K = 0.28\sqrt{\Gamma_d U(V_{gd}, V_{gD})} \exp\left(\frac{-\pi U(V_{gd}, V_{gD})}{8\Gamma_d}\right) \tag{4.9}$$

We can see from the exponential dependence of T_K versus the charging energy, that a reduction of the charging energy can boost the Kondo temperature.

Variation of the coupling to the leads

It should be noted that while the charging energy of the system varies by moving away from the ridge, the effective Γ (Γ_d) varies too. Whereas the

variation of the charging energy can be understood in a purely classical framework, the variation of the coupling to the leads is the combination of inter-dot tunnel coupling and sample geometry.
When we move away from the orbital degeneracy ridge towards the surrounding honeycomb cells, the energy levels of the dots are continuously detuned. From quantum mechanics we know that the detuning of these energy levels influences the resulting molecular states. In particular, our concern is the different proportion of small dot/large dot wave function they hold, and that varies with the detuning of the dots levels.
We consider the surrounding domains (1,0) and (0,1) depicted in figure 4.21. In the center of the (1,0) domain, the molecular ground state is close to a pure small dot state and holds an important proportion of the small dot wave function. In the T shape geometry we use, this means the molecular state connects strongly to the leads, therefore large Γ_d. On the contrary, in the center of the (0,1) domain, the molecular ground state is close to the pure large dot state and holds a small proportion of the small dot wave function. This leads to a small coupling to the leads. On the orbital degeneracy ridge, the proportion of the small dot/large dot wave functions in the molecular ground state is equal. An average coupling to the leads is expected.
To sum up, it appears that moving away from the orbital ridge towards the (0,1) domain, involves an increase of the charging energy and a decrease of the coupling to the leads. These two effects tend to decrease sharply the Kondo temperature of the system (Eq. 4.8). Moving towards the (1,0) domain involves this time an increase of the charging energy and an increase of the coupling to the leads too. These two effects compete against each other in the expression of the Kondo temperature. In conclusion, the experiment shows that the balance obtained in the expression of the Kondo temperature around the orbital ridge is such that the Kondo temperature has a measurable value only on the ridge in question. It is interesting to notice that the T shape geometry we use, implies that in the present Kondo regime we always probe a Kondo effect resulting from a local magnetic moment defined in the small dot.
The expected hierarchy of the Kondo temperatures at different points of the stability diagram is:

$$T_{K(1,0)/(0,1)} > T_{K(1,0)} > T_{K(0,1)} \tag{4.10}$$

Where $T_{K(1,0)/(0,1)}$ is the Kondo temperature on the ridge, $T_{K(1,0)}$ the Kondo temperature in the (1,0) domain and $T_{K(0,1)}$ in the (0,1) domain. At zero temperature, a continuous plateau reaching $\frac{2e^2}{h}$ in the symmetric case would be expected from one domain (1,0) to the other (0,1). It is then due to the fact that our device is operated at finite temperature that the orbital degeneracy ridge appears clearly in the stability diagram.
Concerning the two other domains present in figure 4.21, the (0,0) does not

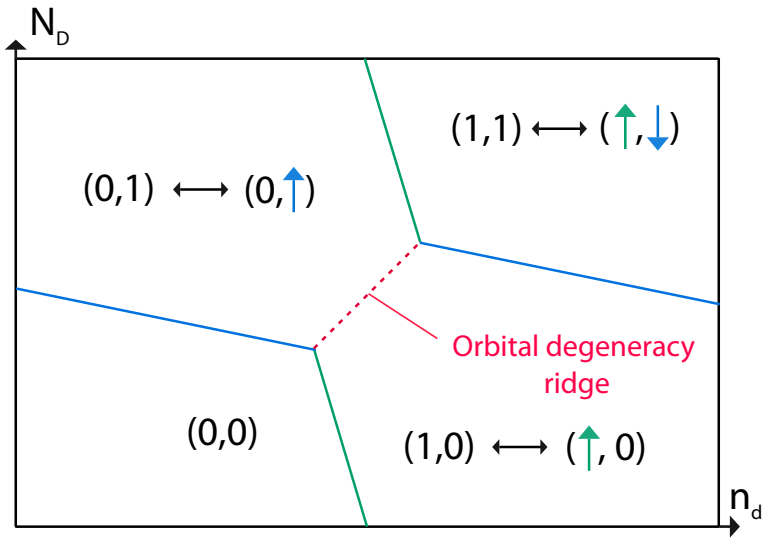

Figure 4.21: schematic honeycomb diagram. The magnetic configurations around the degeneracy ridge have been represented by green and blue arrow for a spin confined in the small dot and large dot respectively. The question of the (1,1) domain concerning the magnetic ground state arises.

present any interest since it corresponds to an empty system. Interestingly, the (1,1) domain where an inter-dot singlet is expected, raises the question of a possible Kondo mechanism. Considerations of the Kondo effect involving this type of electronic configuration will be given later.

4.2.5 Evolution of the Kondo resonance

In order to test our scenario, that is to say a spin Kondo effect on the small dot with a Kondo temperature boosted near the orbital degeneracy ridge, we perform non linear transport measurements locally around the ridge. The idea is to study the evolution of the ZBA associated to the Kondo resonance (therefore to T_K), when we move away from the ridge towards the (1,0) or (0,1) domain. Given the hierarchy we have set in equation 4.10, the ZBA should survive longer in the (1,0) domain than in the (0,1) domain at finite temperature.

Parallel spectroscopy

We perform gate voltage scans above and below the orbital degeneracy ridge along parallel lines as depicted in figure 4.22 (center panel, white arrows). At each voltage gate point, the voltage bias is swept. The point of scanning in parallel to the ridge is to keep a constant detuning between the dots levels and a fixed effective charging energy of the system (as it was the case along

the ridge) (fig. 4.17).

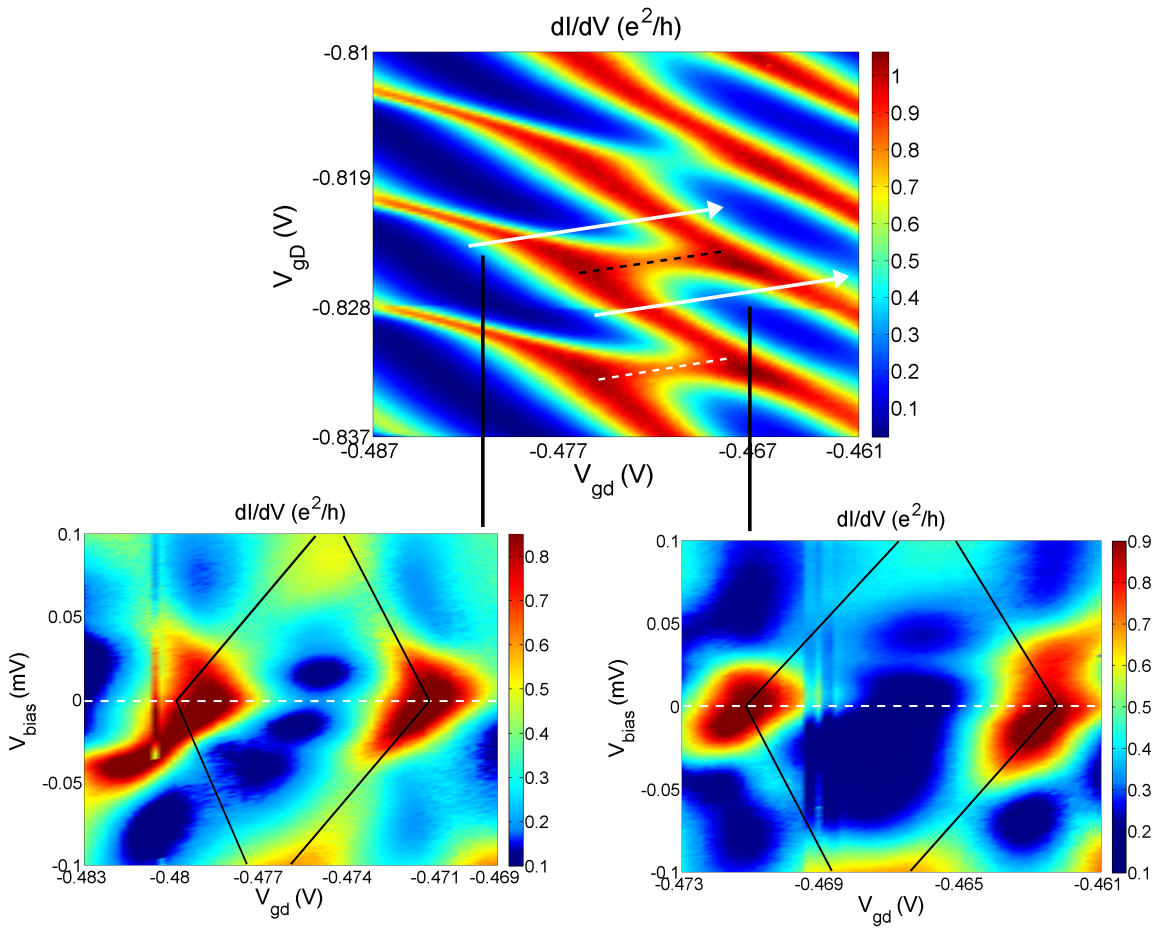

Figure 4.22: non linear measurements around the orbital degeneracy ridge. *Top panel.* The direction of the gate voltage scans are indicated by white arrows in the low temperature stability diagram and which are parallel to the orbital degeneracy ridge. At each point of gate voltage (set $[V_{gd}, V_{gD}]$), the bias voltage is swept. *Bottom panel, left side.* Spectroscopy diagram for the scan performed above the ridge. In the broad diamond obtained, a zero bias anomaly associated to low conductance is present, showing the Kondo processes survive at our base temperature when entering in the corresponding honeycomb cell. *Bottom panel, right side.* Spectroscopy diagram for the scan performed below the ridge. No zero bias anomaly is observed, therefore the Kondo processes are suppressed. Instead a excited state within the diamond can be seen around $V_{bias} = 0.3$ meV.

The diagrams obtained are shown in figure 4.22 (bottom panel).

- *Bottom panel, left side.* This non linear transport measurements cor-

responds to a voltage gate scan performed along a parallel line to the ridge, running above it. As in the case of the spectroscopy following the orbital ridge (Fig. 4.17), a diamond shape can be identified in the dI/dV color plot. The main observation is the presence of a line within the diamond presenting low conductance and locked at zero bias. This line is consistent with a Kondo resonance (Sec. 4.2.2, non linear transport measurements). Due to the low conductance associated to the ZBA, it is straightforward that the Kondo temperature of the system is reduced within respect to the Kondo temperature found on the ridge. We can also see that despite the small amplitude of the ZBA, it presents a rather large width. We conclude that the ZBA identified in this diagram can be associated to a thermal broadened Kondo resonance ($T_{el} > T_K$). In other words, here the system is in the high temperature limit of the Kondo regime because of the reduced T_K.

- *Bottom panel, right side.* In the case of this diagram, the voltage scan is now performed below the orbital ridge. We can immediately see that there is no ZBA within the diamond obtained. It is legitimate to believe that the Kondo temperature in this diagram is so small, $T_K << T$, that even at the lowest temperature we can achieve, the system has no yet entered the Kondo regime. Therefore no trace of Kondo resonance is detected.

If we make a parallel between the different spectroscopy diagrams analysed and our model, we can associate the honeycomb cell above the ridge to a domain of type (1,0) and the honeycomb cell below the ridge, to a domain of type (0,1) in order to conciliate the experimental data and our two level system description.

One can note at this point that the domain where the ZBA survives longer (at finite temperature) should be located below the orbital degeneracy ridge according to figure 4.21. By taking into account the fact that our device holds multiple electrons in each dot, we can meet a situation where the whole diagram is inverted in terms of effective configurations. For example we start from a (3,3) configuration instead of a (0,0) configurations. The (3,3) configurations can be mapped onto a (1,1) configuration by eliminating the low energy singlets of each dot which are not magnetic, so that we consider they do not enter the Kondo process. From the (3,3) configurations we can build the diagram depicted in figure 4.23 which we can now conciliate with the experimental data, more precisely the behaviour of the Kondo resonance around the orbital degeneracy ridge.

Before concluding, we want to emphasize that precautions should be taken. The previous spectroscopy experiments do not give the complete evolution

of the Kondo resonance away from the ridge. An unfortunate choice of the gate voltage scan can actually lead to the wrong conclusion. Indeed if the gate voltage scan is performed too close to the orbital degeneracy ridge, then on both sides of the ridge we can expect to detect a ZBA. In the case of a gate voltage scan too far from the ridge we can then expect on both sides of the ridge that no ZBA is detected. Therefore, if the diagram shown in figure 4.22 (bottom panel, left side) corresponds to a gate voltage scan too close to the ridge and that the diagram shown in figure 4.22 (bottom panel, right side) corresponds to a gate voltage scan too far from the ridge we would expect to see the observed behaviour around zero bias in any case. To get a better insight of the evolution of the Kondo resonance, spectroscopy experiments following transversal gate voltage scans to the orbital ridge will be presented in next section. Before showing these non linear measurements we discuss briefly about the excited states seen in the diagrams of figure 4.22.

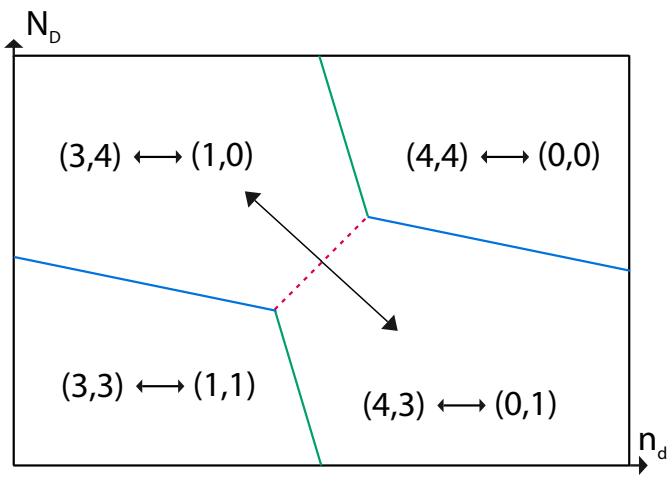

Figure 4.23: Effective configurations around an orbital degeneracy ridge for higher fillings. The non magnetic singlets are assumed not to play a role in the Kondo process and therefore eliminated.

Excited states

Beyond the behaviour of the system near zero bias, we can see the presence of extra lines within the diamonds of figure 4.22 (bottom panel),. As discussed in the chapter 2, section 2.5, these lines can be attributed to inelastic cotunneling lines. The idea is that near zero bias, transport only involves the ground state of the system. When the voltage bias $\mid V_{bias} \mid$ is increased, it can provide the energy necessary for an incoming electron to visit an excited state, more precisely when $\mid eV_{bias} \mid \geq E_{excited\,state} - E_{ground\ \ state}$.

The result is an increase of the current through the device since more paths are now available for an electron to flow through the device. As mentioned in Chapter 2, this holds for cotunnelling processes that dominate transport when the system is blocked. In a Coulomb diamond an increase of the current due to inelastic cotunneling (cotunneling involving an excited state) shows up as a line in terms of differential conductance (dI/dV).

- *Figure 4.22, bottom panel, left side.* Two inelastic cotunneling lines (at positive and negative bias) are seen, and show a dispersive behaviour from one side of the diamond to the other. Usually, since the quantity $E_{excited\ \ state} - E_{ground\ \ state}$ is expected to be constant, a non dispersive inelastic cotunneling is expected (parallel to the gate voltage axis). However such dispersive behaviours of inelastic cotunneling lines have already been reported in nanotubes [79] and are attributed to an asymmetry between the ground state and the excited state from the point of view of the coupling to the leads, $\Gamma_{Ground\ \ state} \neq \Gamma_{excited\ \ state}$. The main remark we can give about these excited states is that since they are seen near the orbital degeneracy ridge and within the diamond we can relate them to excitations where the electron hopes from one dot to the other (fixed charge in the total system). More precisely in the (1,0) domain the (0,1) state is an excited state and vice versa. Or in terms of molecular states, we can relate the excitations of the system with the anti bonding state.

- *Figure 4.22, bottom panel, right side.* A single cotunneling line is observed at positive bias. This kind of asymmetry is usually attributed to an asymmetry $\Gamma_L \neq \Gamma_R$. However it is not yet clear if this is indeed the case. Concerning the nature of the excited state, again we can relate them to the anti bonding state of the molecular system.

As we will see better understanding of these inelastic cotunnelling lines can be achieved via non linear measurements following transverse cuts to the orbital (degeneracy) ridge.

Transversal spectroscopy

Another type of spectroscopy experiment we can perform is a non linear transport measurement following a transverse scan to the ridge crossing its center as shown in figure 4.23 (black arrows). During such a scan, the levels of the dots are detuned continuously to go towards the pure small dot and large dot states, recovered for large detuning compared to the tunnel coupling. Moreover by going towards the center of the honeycomb cells the effective charging energy of the system increases, thereby decreasing the Kondo temperature according to our argumentation. This type of spectroscopy should enable us to monitor the continuous evolution of the Kondo

resonance.
The obtained diagram are shown in figure 4.24 where the bottom diagram corresponds to a transverse cut towards the domain above the ridge (effective (1,0)) and the top diagram to a transverse cut towards the domain below the ridge (effective (0,1)) (see fig. 4.23).
At a voltage $V_{gd} = -0.468V$ on the voltage axis of each graphic, large conductance around zero bias is found. This corresponds to the conductance associated to the orbital ridge, in other words the ZBA resulting from Kondo processes on the ridge as indicated in the figure.
The main observations we can make from these diagrams are:

- We can immediately observe that the conductance around zero bias, which is associated to the Kondo resonance decreases more rapidly in the bottom diagram (Towards ridge above) than in the top diagram (Towards ridge below). This remark points in the direction of a Kondo temperature decreasing more rapidly in the bottom diagram than in the top diagram. Interestingly, the diagram where the Kondo temperature decreases the less corresponds to a domain that we associated to an effective (0,1) from the parallel spectroscopy measurements (Fig 4.22) since we performed it below the orbital degeneracy ridge. This is inconsistent with the hierarchy shown in equation 4.10. Since the transverse spectroscopy experiments give a continuous evolution of the ZBA we rely on these more than on the parallel ones. As mentioned, the parallel spectroscopy can induce in error, and this is what figure 4.24 points out. Therefore we now associate the domain below the orbital ridge with an effective (1,0) configuration and the domain above with an effective (0,1) configuration as depicted in the diagrams. We will confirm this point by analysing the profile of the orbital ridge in the stability diagram.

- Interestingly, if we look carefully at the evolution of the ZBA in the top diagram, it seems to disperse to higher bias when we move away from the position of the orbital degeneracy ridge. A priori, this is not consistent with a Kondo resonance that should be locked at zero bias. We believe this is due to the asymmetry of the diagram with respect to the bias. This can be attributed to the asymmetry of the coupling to the leads, $\Gamma_{left} \neq \Gamma_{right}$. The diagram presents three lines (2 excitations, 1 ZBA) Γ broadened. Since the line present at negative bias has little spectral weight, we believe that the recovery of the ZBA and the excitation line at positive bias gives the impression that the ZBA disperses. Simple simulations where performed to confirm this statement as shown figure 4.25.

- The mentioned excitation lines correspond to inelastic cotunneling lines. We attribute these lines to the anti bonding state that is visit

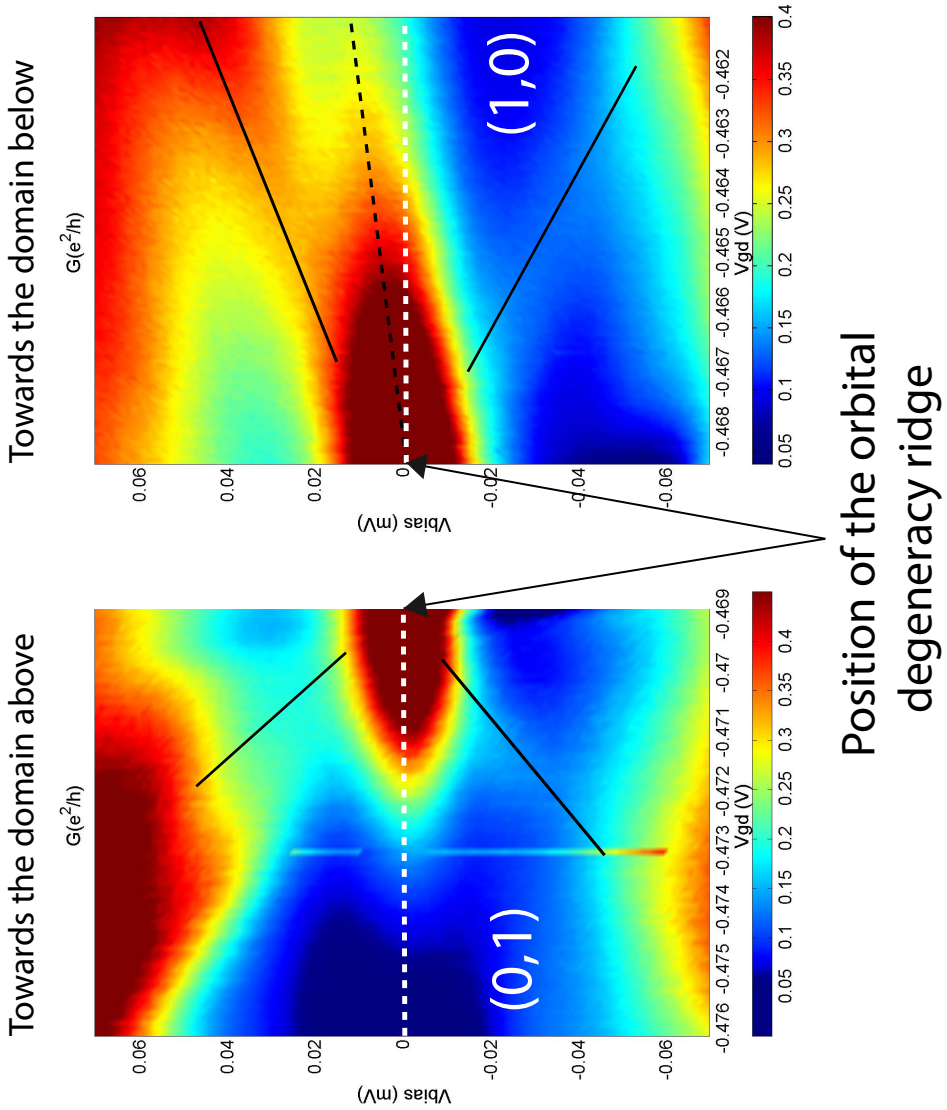

Figure 4.24: Non linear measurements performed following gate voltage scans transverse the orbital ridge and crossing its center. *Bottom diagram.* Measurements following a gate scan going towards the domain above the orbital ridge. The position $V_{gd} = -0.469V$ corresponds to the location of the orbital ridge. *Top diagram.* Measurements following a gate scan going towards the domain below the orbital ridge. The position $V_{gd} = -0.469V$ corresponds to the location of the orbital ridge.

at finite voltage bias. The dispersion when the gate voltage is moved comes from the detuning of the dots levels. On the orbital ridge, the detuning is zero and one should find the anti bonding state at

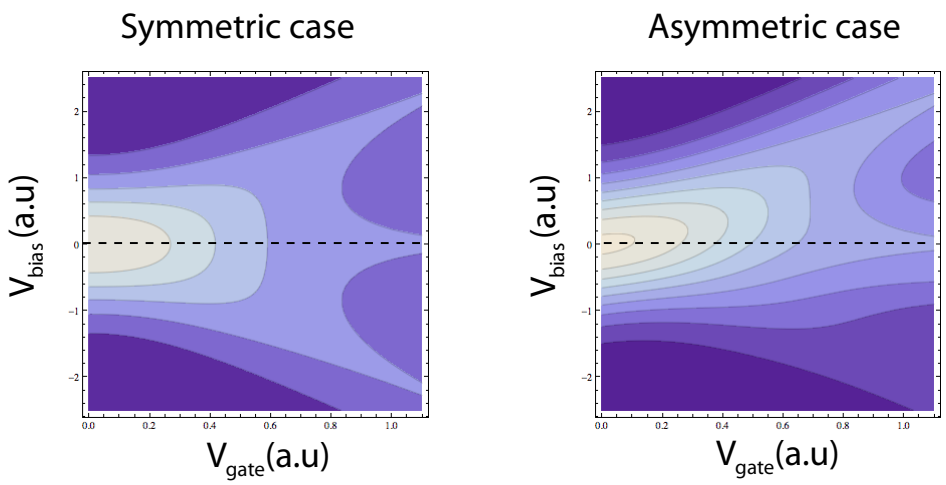

Figure 4.25: Simulations using three Gaussian functions, where one is locked at zero bias (Kondo resonance) and the other two disperse (inelastic cotunneling lines). For the symmetric case, each Gaussian has the same amplitude (spectral weight) fixed to 1 (in arbitrary units). In the asymmetric case the Gaussian function dispersing towards negative values of V_{bias} has been attributed a lower spectral weight, fixed to 0.4. In this situation the maximum of amplitude near zero bias seems to disperse towards positive bias.

$V_{bias} = \pm t_{dD}$. By moving away from the orbital ridge the energy of the anti bonding state is raised which is consistent with the dispersion observed in both diagrams. Notice that the splitting that one should see on the orbital ridge cannot be identified in the diagrams due the strong conductance structure associated to the ZBA. This would suggest $t_{dD} \lesssim 20\mu eV$. As we will see later we have evidence that the inter-dot tunnel coupling is actually larger. The question of a large t_{dD} will be considered later, in the framework of a more general description of the system involving more than two levels in order to understand the experimental data.

To summarize, the transverse spectroscopy experiments confirm a spin Kondo effect with a Kondo temperature boosted on the orbital ridge and that follows a asymmetric profile around the ridge in agreement with the arguments given in section 4.2.4.

4.2.6 Profile of the orbital degeneracy ridge

The asymmetric behaviour of the Kondo temperature as seen in the previous diagrams 4.24 will be contained in the stability diagram where the conductance should fall more rapidly on one side of the ridge (towards domain below) than on the other (towards domain above). It is not obvious from

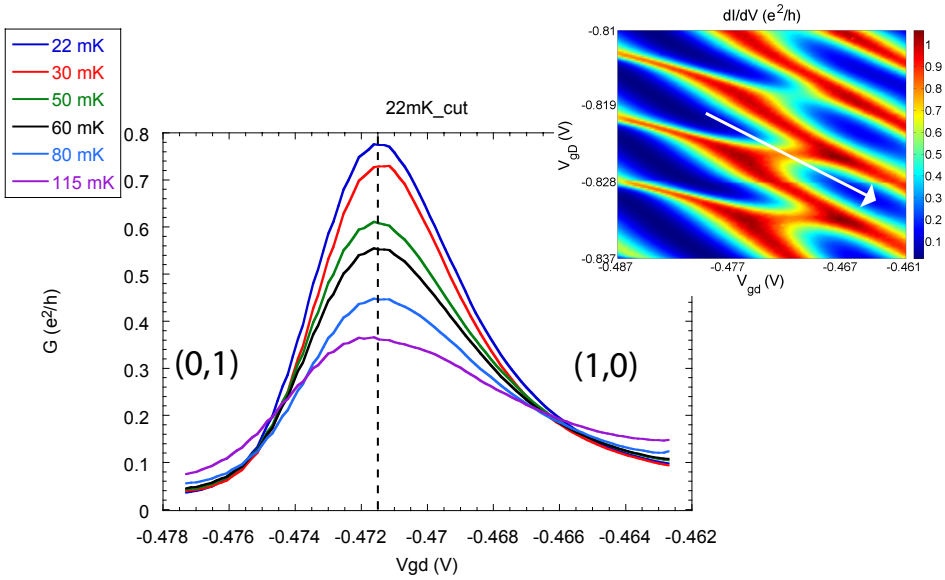

Figure 4.26: Cuts across the orbital ridge performed in the stability diagram for different temperatures. The diagram attached in the top right corner shows the direction of the cuts via a white arrow.

the color code in figure 4.13 that this is the case. To confirm, we perform a direct cut across the orbital ridge in the stability diagram and do it for different temperatures. The profiles obtained are shown in figure 4.26.
The asymmetric profile obtained confirms the observations made from the transverse spectroscopy diagrams. We see that:

- *Fixed temperature.* The conductance drops faster when we enter the domain above the orbital ridge (left side of the peak).

- *Fixed gate voltage.* For fixed distance around the ridge $V_{gd} = -0.4715 \pm V_{gd0}$, the conductance drops faster within temperature when we enter the domain above the ridge.

4.2.7 Addition of the second electron

As one can observe in figures 4.13 and 4.22, all the orbital degeneracy ridges present in the low temperature stability diagrams present relatively high conductance. So far, we gave an explanation near the degeneracy of the (1,0) and (0,1) states (or effective states). As depicted in figure 4.27, we need to consider the addition of the second electron in the system in order to account for the physics around the next orbital degeneracy ridge.
This naturally leads us to consider the orbital ridge corresponding to the degeneracy of the (1,1) state and (0,2) state (Fig. 4.27, dashed black box).

Notice that by using effective electronic configuration, we have a continuous succession of orbital degeneracy ridges of type (1,0)↔(0,1) and (1,1) ↔(0,2) in the two level representation we are using. It is worth noticing that if we derive a Kondo mechanism around the (1,1)↔(0,2) degeneracy ridge, then all orbital ridges can in principle be understood from the effective electronic configurations (1,0), (0,1), (1,1) and (0,2) since we can always map a two level system onto these effective configurations by eliminating the low energy singlets.

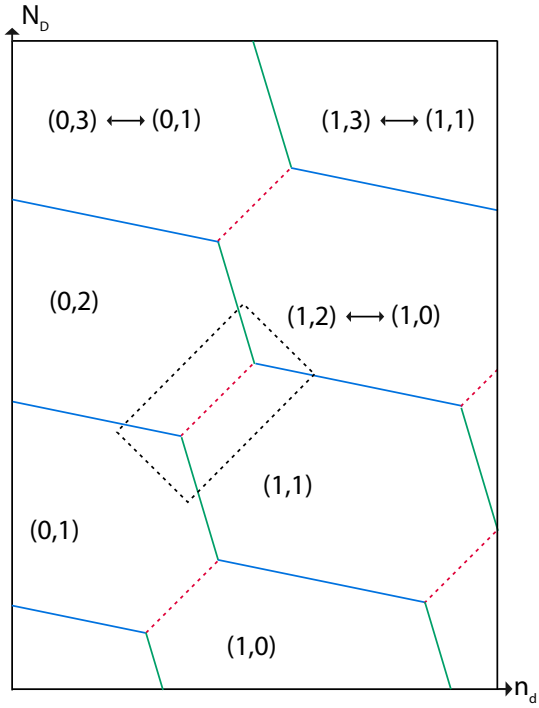

Figure 4.27: Schematic honeycomb diagram depicting several orbital degeneracy ridges and the associated effective electronic configurations according to a two level representation.

First we show the spectroscopy experiments performed around the orbital ridge below the first one we studied, as indicated by the white dashed line in figure 4.22. non linear measurements following gate voltages scans along and across the ridge are shown in figure 4.28, following the same protocol as presented earlier around the (1,0)↔(0,1) degeneracy line (sec. 4.2.5). Interestingly, the spectroscopy obtained display the same patterns as in the studies performed around the previous orbital degeneracy ridge:

- *Panel a.* The spectroscopy performed along the ridge displays a ZBA extending from one triple point to the other. The large conductance of

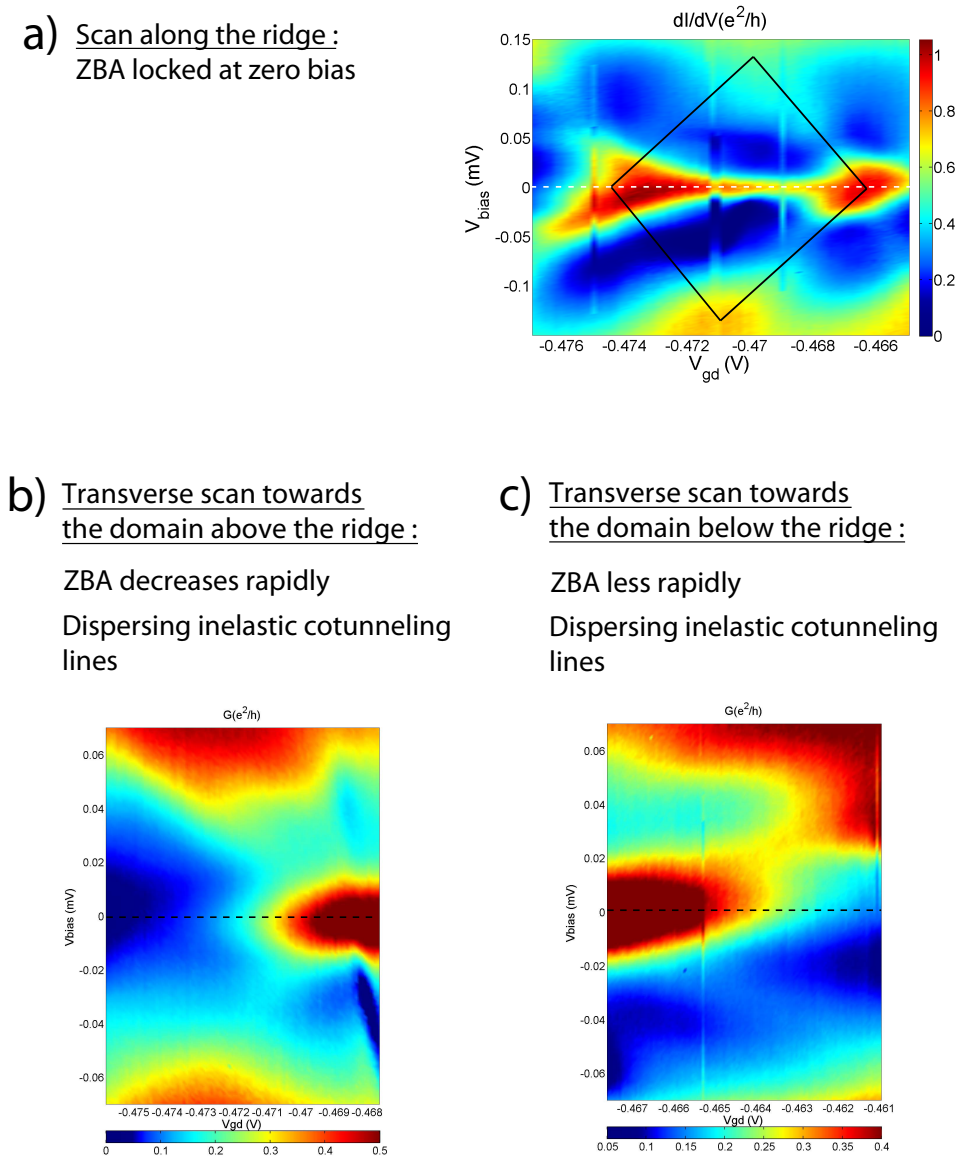

Figure 4.28: *Panel a.* non linear measurements following a gate voltage scan along the orbital degeneracy ridge. The conductance on the ridge is locked at zero bias. Panel b non linear measurements following a transverse gate voltage scan parallel to the ridge going towards the domain above it. *Panel c.* non linear measurements following a transverse gate voltage scan parallel to the ridge going towards the domain below it.

the ZBA, $\sim \frac{e^2}{h}$, indicates a well formed Kondo resonance. The FWHM is found to be of the order of 200 mK as on the previous ridge.

- *Panel b.* The transverse spectroscopy going towards the domain above (Fig. 4.27, (0,2)) shows that the ZBA found on the orbital ridge decreases rapidly.

- *Panel c.* The transverse spectroscopy going towards the domain below (Fig. 4.27, (1,1)) shows that the ZBA decreases less rapidly.

The similarities found from one orbital ridge to the following are actually not straightforward to apprehend. The point is that the ground state of the system for one electron and for two is extremely different from the point of view of magnetism. In the case of a single electron, the system is always magnetic. On the contrary for two electrons we expect the system to be non magnetic [45]:

- *(1,1) domain* In presence of inter-dot tunnel coupling and at zero magnetic field, the (1,1) state should correspond to a singlet state delocalized between both dots that is stabilized by the inter-dot exchange interaction. We expect that by stabilizing a singlet in the double dot device, the Kondo effect is suppressed. This is in disagreement with the ZBA found within figure 4.28 (c) that extends far in the (1,1) domain.

- *(0,2) domain* This domain corresponds to the absence of magnetism in each dot since the occupation number of both of them is even. Due to the fact that we work at zero magnetic field, we expect singlet states in each dot (no triplet S=1) and therefore we expect that the system cannot undergo the Kondo effect in this domain. We cannot explain with this assumption and the previous one, the presence of a ZBA in figure 4.28 (b).

To summarize we do not expect the system to undergo the Kondo in the domains surrounding the orbital ridge (1,1)$\leftrightarrow$(0,2) if as assumed singlets are stabilized within the double dot. By extension, it is straightforward that the orbital degeneracy should not display a ZBA and lead to high conductance through the device.In this case, one orbital ridge over two in the V_{gD} direction, should be "switched off" if we follow the effective electronic configurations depicted in figure 4.27 (In the dashed box, no conductance should be found on the orbital ridge). This parity effect does no appear in the experimental data (Fig. 4.22, top panel). We need to understand which kind of mechanism explains the absence of parity effect, that is to say how the Kondo process is found on each orbital ridge of figure 4.22. Two scenarios based on the interplay of the Kondo mechanism and the inter-dot exchange interaction will be discussed:

- A two stage Kondo effect in the (1,1) domain.
- A multi level effect in the double dot device.

4.2.8 Interplay between Kondo and exchange

Two stage Kondo effect

We mentioned in the previous section, that in presence of inter-dot tunnel coupling, the (1,1) state is a singlet state. This is accurate for an isolated double dot or in the case of weak coupling to the leads. Generally speaking, in presence of tunnel coupling to leads, that is to say to Fermi seas, the ground state is not necessary an inter-dot singlet. In a T shape geometry, where the spin of the small dot connects to leads and to the large dot, a competition will establish between the inter-dot exchange interaction favouring an inter-dot singlet and the Kondo temperature favouring a singlet delocalized between the small dot and the leads. From theoretical literature [9] [80], the ratio J_{dD}/T_{Kd} will define the ground state of the system. As schemed

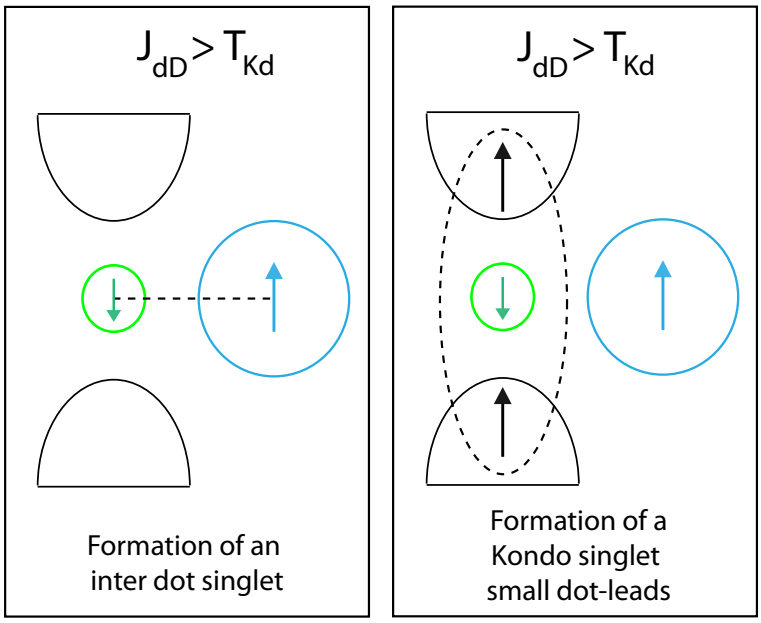

Figure 4.29: T shape double quantum dot. *Left panel* In the limit of $J_{dD} > T_{Kd}$ an inter-dot singlet is stabilized. The system does not undergo the Kondo effect. *Right panel.* In the limit $J_{dD} < T_{Kd}$ a singlet is formed between the small dot and the leads. At $T \sim T_{Kd}$, the system undergoes the Kondo effect. During this first stage the spin in the large dot decouples. It will be screened during a second stage at $T \sim T_{KD} \ll T_{Kd}$.

in figure 4.29 (left panel), when the inter-dot exchange J_{dD} is larger than

T_{Kd}, an inter-dot singlet is stabilized and the system does not undergo the Kondo effect at any temperature. In the other limit where J_{dD} is smaller than T_{Kd}, a Kondo type singlet between the moment of the small and the leads is formed and the system can undergo the Kondo effect at $T \sim T_{Kd}$. Theoretical studies dealing with side coupled double dots, have shown that in that limit the system undergoes the so called two stage Kondo effect. In the first stage, the magnetic moment of dot d is quenched by the electrons of the leads below some temperature T_{Kd} as depicted previously. The conductance through the device shows the usual enhancement of the conductance following a temperature law well established in the standard Kondo effect. During the first stage the local moment on the large dot, effectively decouples. In the second stage, which occurs at a much lower temperature (Eq 4.11), the magnetic moment of dot D is in turn quenched by electrons that lie within the narrow Kondo resonance around the Fermi level formed during the first stage.

$$T_{KD} \sim T_{Kd} \exp\left(\frac{J_{dD}}{T_{Kd}}\right) \tag{4.11}$$

The screening of the second local moment side coupled, results in a suppression of the conductance through the device. At low temperature, $T \ll T_{KD}$, the magnetic moments of the dots form a tightly bound singlet.
Since $T_{KD} \ll T_{Kd}$, and given the estimation of the Kondo temperature extracted earlier from non linear measurements, i.e. $T_{KD} \sim 100mK$, we would not be able to resolve the second stage of the Kondo effect in the (1,1) configuration and we would only be sensitive to the first stage, that is to say an enhanced conductance at $T_{KD} < T < T_{Kd}$ through the device due to a spin 1/2 Kondo effect.
This can explain a spin Kondo effect detected at finite temperature in the (1,1) domain. However an estimation of the tunnel coupling that one can relate to the inter-dot exchange would be helpful. By studying the deviation of the low temperature stability diagram (Fig. 4.13) from a pure honeycomb diagram as we did in section 4.1, we find $t_{dD} \sim 60\mu eV$. In the (1,1) domain, far from the orbital degeneracy line, one can show that $J \sim 4\frac{t_{dD}^2}{U_d}$, from which we get an estimation $J \sim 20\mu eV$. This estimation is already above the estimation of the Kondo temperature extracted on the ridge where it is maximal[12]. Moreover, we know from the literature that the binding energy of the inter-dot singlet will grow as we approach the degeneracy point with the (2,0) state. This immediately translates in an increase of the inter-dot exchange interaction as going towards the orbital degeneracy line.
In conclusion, the two stage Kondo effect would explain why a spin Kondo

[12]Temperature law and estimation of the Kondo temperature on the (1,1)↔(0,2) ridge give the same results as in the case of the (1,0)↔(0,1) ridge

effect can be expected in the (1,1) domain at finite temperature and by continuity a Kondo resonance can be expected at the interface (1,1)-(2,0), with a boost of T_{Kd} via the reduced charging energy of the system. However by putting numbers this scenario seems to be difficult to conciliate with the experimental data. Work on better ways to extract a more reliable estimation of t_{dD} is still undergoing.

Multi level quantum dots

Due to the weak level spacing measured in the large quantum dot, we know from our previous experiment (sec. 4.1) that for large inter-dot tunnel coupling, $t_{dD} > \Delta E_D$, it is important to consider the hybridisation of the dots in a multi level approach. The estimation of t_{dD} given previously indicates that the inter-dot tunnel coupling is greater than the level spacing of the large dot.
In the following we are going to discuss the implications of a multi level large quantum dot from the point of view of the binding energy of the inter dot singlet possibly formed in the (1,1) configuration. We will address two extreme limits in the (1,1) configuration: the case of a single energy level in the small dot that hybridises with a continuum of energy levels or a single energy level, in the large quantum dot. The evolution from one limit to the other will enable us to define the ground state of the system in the (1,1) configuration.

From the Continuum limit to the single level limit

In the (1,1) configuration, the question of the interaction of a single localized level (small dot) and a continuum of states (large dot) can be mapped on the Kondo problem[13]. Indeed this situation corresponds to the hybridisation of a local moment and a continuum or reservoir. As we know from theory, at low energy a N body singlet will be formed between the dots with a binding energy defined by the Kondo temperature (Appendix B):

$$T_{KdD} \simeq D \exp\left(-\frac{1}{\rho J}\right) \tag{4.12}$$

Where ρ is the density of states in the large dot that corresponds to a continuum, D is an energy cut off (bandwidth $=2D$) and J the Schrieffer-Wolff exchange interaction (Eq. 2.37).
In the opposite limit where two single localized levels (one level per dot) are tunnel coupled, the ground state of the system in the (1,1) configuration is a molecular singlet state stabilized by the exchange interaction,

$$J_{dD} = E_{singlet} - E_{triplet} \sim 4\frac{{t_{dD}}^2}{U} \tag{4.13}$$

[13]For odd occupancy of the localized level

Actually, if one performs an analogous perturbation calculation used to obtain equation 4.12 [81] when the large dot contains a single level, $\rho = \frac{1}{2D}$, the expression of the Kondo temperature reduces to the exchange interaction (Appendix B).

Reduction of the inter-dot singlet binding energy

The crucial point of our discussion holds in the fact that the bare exchange interaction 4.13[14] is larger than the Kondo temperature. That is to say the binding energy of the inter-dot singlet is larger in the case of a two level system than in the continuum limit.
To illustrate our point we make the following calculation. We start from the expression of the Kondo temperature given in 4.12 where ρ is replaced by $1/D$ as commonly done in literature.

$$\begin{aligned} T_{KdD} &\sim \frac{1}{\rho}\exp\left(-\frac{1}{\rho J_{dD}}\right) \\ \frac{T_K}{J_{dD}} &\sim \frac{\exp\left(-\frac{1}{\rho J_{dD}}\right)}{\rho J_{dD}} \end{aligned} \tag{4.14}$$

Since the quantity $\rho J_{dD} < 1$ ($\Leftrightarrow J_{dD} > D$)[15] in the Kondo regime, we conclude that $T_{KdD} < J_{dD}$.
As a result, the increase of the number of energy levels entering the large quantum dot tend to reduce the binding energy of the singlet formed between the dots. We refer now to the binding energy of the inter-dot singlet as $T_{KdD}(N)$ or $T_{KdD}(1/\Delta E_D)$ since its is a function of the number of energy levels entering the hybridisation process. From the limiting cases addressed above, we assume that for fixed tunnel coupling there must be a continuous reduction of $T_{KdD}(1/\Delta E_D)$ when the level spacing in the large dot decreases.
To emphasize this reduction, Pablo Cornaglia performed calculations of the Singlet-Triplet splitting (singlet binding energy) E_{ST} and the effective hopping (t_{eff}) for a single level in the small dot d coupled to a multi level quantum dot D (large dot). The study is done in the center of the (1,1) domain, deep in the Coulomb blockade valley. In order to simplify the numerics, the parameters chosen for system were $U_d = U_D$. A fixed energy span W for the levels of the large dot that couple to the small dot was considered, so that for N levels, its level spacing stands as $\Delta = W/(N-1)$.

[14] Defined in a two level system

[15] $J_{dD} > D$ would imply that at an energy D, the highest excitation energy, J_{dD} dominates already the physics of the system. A singlet state is stabilized at high energy (temperature) and the system does not undergo the Kondo effect.

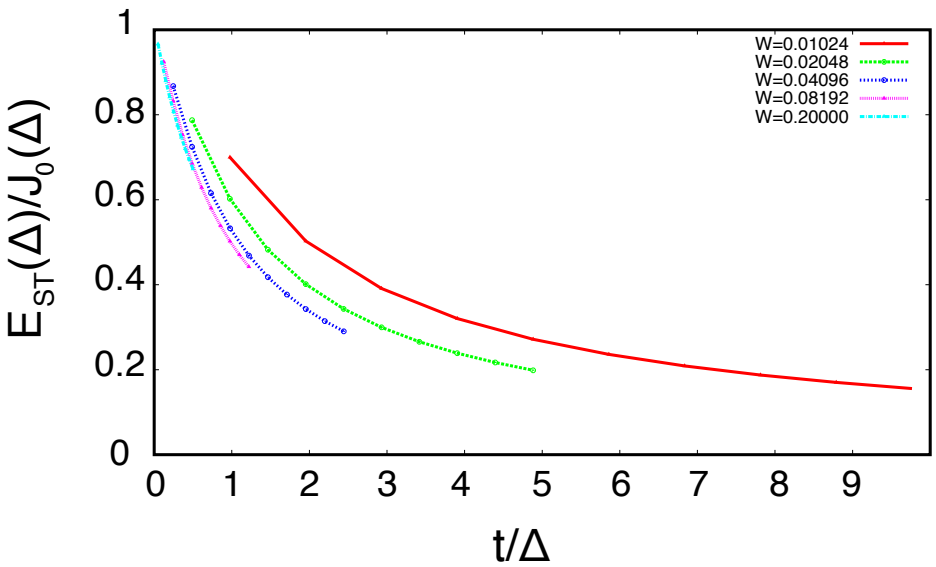

Figure 4.30: Evolution of the inter-dot singlet binding energy as a function of the number of energy levels in the large involved in the hybridisation processes with the small dot.

The hopping to each level is given by $t_{dD}/\sqrt{N}$. The effective hopping is calculated for a single electron in the double quantum dot as the energy gain due to the presence of the hopping. Then, the E_{ST} is obtained as the singlet triplet splitting for two electrons in the system (no Kondo renormalisation here).
We show in figure 4.30 a plot of $E_{ST}/(4t_{eff}^2/U)$ as a function of t/Δ for different W (N from 2 to 11). As one can see in all cases the singlet triplet splitting energy decreases when more energy levels of the large dot are involved in the inter-dot hybridisation process, i.e when t/Δ increases.
We believe that from our estimation of t_{dD} that at least three energy levels in the large dot or more are involved in the hybridisation with the small dot. Therefore, we expect our system to be in the intermediate regime between the single level limit and the continuum limit.

Screening of the local moments in the (1,1) domain

In order to define the ground state of the system we need to compare the energy scale $T_{KdD}(1/\Delta E_D)$ defining the binding energy of the inter-dot singlet and T_{Kd} defining the binding energy of the small dot-leads singlet. On the one hand if $T_{KdD}(1/\Delta E_D) > T_{Kd}$, an inter-dot singlet is formed at temperatures of the order of $T_{KdD}(1/\Delta E_D)$ and the system does not undergo the Kondo effect with the leads at any temperature. A parity effect

would be seen in the low temperature stability diagram as mentioned earlier (sec. 4.2.7). On the other hand if the condition $T_{Kd} > T_K(1/\Delta E_D)$ is satisfied as represented by the red dashed lines in figure 4.30, the system gains more energy by stabilizing a "small dot-leads" singlet rather than a "small dot-large dot" singlet. As in the case presented in section 4.2.8 the system will undergo a two stage Kondo effect resulting in a none magnetic ground state at zero temperature. At temperatures of the order of T_{Kd} the system undergoes a spin Kondo effect with the leads that screens the spin on the small quantum dot. During this first stage the large dot spin decouples. The screening of the remaining spin is pushed to much lower temperature via the same process mentioned in section 4.2.8 (Two stage Kondo effect), that is to say the spin in the large dot will be screened by the quasi-particles that lie within the Kondo resonance around the Fermi energy formed during the first stage. As a result the Kondo temperature of the second stage T_{KD} will be a renormalized quantity depending on T_{Kd} and will take a form analogous to 4.11. The energy scale $T_K(1/\Delta E_D)$ is no more a relevant quantity. To conciliate experiments with this qualitative analysis, we require that $T_{KD} < T < T_{Kd}$, in other words that at the lowest temperatures we can achieve we cannot resolve the second stage, which given our estimation of the Kondo temperature in the system makes sense. Then, by continuity from the center of the (1,1) domain, we can expect a Kondo plateau extending up to the orbital degeneracy ridge (1,1)$\leftrightarrow$(0,2) which at finite temperature could reveal a marked Kondo ridge at the interface (1,1)-(0,2) because of the boosting of the Kondo temperature already discussed. NRG calculations using a reduced form of the Hamiltonian of the system shown in appendix A, are currently being performed in order to confirm this scenario. Moreover an estimation of the number of energy levels required to satisfy $T_K^{leads} > T_K(1/\Delta E_D)$ in our system is needed. Calculation in that directions are under consideration.

All the theoretical support concerning this experiment was given by Serge Florens [72], Denis Feinberg [72], Carlos Balseiro [74] and Pablo Cornaglia [74].

Conclusion and perspectives

During this project, a double quantum dot device was used to study an important problem of highly correlated electron systems, the Kondo effect. Motivated by recent theoretical publications, we chose a design consisting of small quantum dot connected to metallic leads and side coupled to a large quantum dot. This specific design, already used to study the two channel Kondo effect [8], is expected from literature to offer the opportunity to study various exotic Kondo effects [19] [20] including the Kondo box problem [11] [10]. This particular problem arises when a magnetic impurity (small dot) is screened by a finite reservoir (large dot). Strong finite size effects such as the loss of universality are expected when the level spacing in the finite reservoir becomes of the order of the Kondo temperature.
Even though we did not find evidences of an inter dot Kondo effect, the strong coupling regimes that we studied raised intriguing questions concerning the hybridisation mechanisms between the dots and with the leads. Important experimental and theoretical efforts were put into the influence of hybridisation ("dot-Dot" and "dot-leads") on the transport properties of the double dots system.

The first problematic we raised was the effect of strong inter-dot tunnelling when the coupling to the leads can be considered as weak. At low temperature, strong irregularities associated to irregular fillings of both dots were observed in the stability diagram whereas regular fillings were recovered at higher temperature. It was emphasized that a crucial parameter to understand transport through the system was the ratio $\frac{t_{dD}}{\Delta E_D}$. The result of a large ratio, is a complex molecular addition spectrum that accounts for the unusual transport properties at low temperature. In order to capture the physics of the system a formalism based on exact diagonalization of a reduced Hamiltonian of the system, that is to say of multi-level interacting dots, was presented. Thanks to the Meir-Wingreen formula, conductance maps were simulated. A qualitative agreement between experiments and theory was obtained by taking into account the cross talk effect influencing the inter dot tunnelling matrix element. Interestingly the effect of temperature was naturally taken into account by the model via the number of molecular states participating to transport. Above a certain temperature,

$T > t_{dD}$, an effective averaging over several molecular states leads to regular transport properties as observed.

By increasing the coupling with the leads, we could tune our device in the Kondo regime on a particular region of the stability diagram: the orbital degeneracy ridge where the dot energy levels are degenerated. On this ridge, the effect of inter dot tunnel coupling is maximal and the molecular eigenstates of the system are far from the pure small dot/large dot states. We attribute this Kondo ridge to a spin Kondo effect where the Kondo temperature is boosted near the ridge via the reduction of the charging energy of the system. Spectroscopy experiments performed around the orbital degeneracy ridge showed an odd/even effect as a function of the parity of the small dot. Interestingly, no parity effect was found as far as the large dot occupation number. To account for this invariance, we were pushed to consider the interplay between the Kondo temperature and the exchange interaction between the dots to explain that a delocalized singlet "small dot/leads" was formed at low temperature rather than a delocalized singlet "small dot/ large dot". A multi level scenario describing hybridisation between the dots enabled us to point out the reduction of inter-dot singlet binding energy when the level spacing of the large dot decreases. Theoretical investigations based on NRG calculations are currently outgoing to confirm that in our system the reduction is sufficient to satisfy $J < T_K$, in other words that a Kondo singlet "dot-lead" is stabilized.

To summarize, both experiments show the importance of the strength of the tunnel coupling compared to the intrinsic energy scales of the dots, and in particular the level spacing. It appears from literature that a lot of work has still to be done in these strong coupling regimes from the point of view of theory and experiments to get better insight on this physics.

In perspective we would like to point out that:

- Our first experiment showed that rich transport properties are obtained in multi level (or strongly coupled) interacting dots, however we still suffer from a lack of physical pictures and analogies to understand in simpler terms transport in this strong inter-dot coupling regime. An important question that we did not study in detail is the influence of the coupling with the leads on the transport properties of the system. It appears that, so far, no formalism is able to treat the complete Hamiltonian shown in appendix A in order to calculate the transport parameters of the system. From this point of view it is crucial to carry more experimental investigations in strongly coupled dots. Simple question such as the influence of Kondo mechanisms on the modulation of the molecular degeneracy lines, their position in the

diagram, the evolution of the system within temperature appear to be difficult questions to answer to at this stage.

- The question of the Kondo box problem still remains open to our knowledge. Even though the problems of the exchange interaction in the case of two energy levels and the case of a single energy level and a continuum have found answers, the evolution from one scenario to the other is still a complicated problem. Indeed the case of a finite interacting reservoir screening a local moment is a difficult problem to treat theoretically and very few literature can be found on this topic. NRG methods used in the continuum limit appear to be difficult to adapt to a problem where the reservoir is subject to on-site repulsion and we suffer from a lack of knowledge of the physics in this intermediate regime where finite size effects are expected. Therefore theoretical and experimental efforts are required to apprehend the Kondo regime in a finite system.

Appendix A

Multi level interacting quantum dots

The Hamiltonian describing our double quantum dot is derived from a two impurity Anderson Hamiltonian [82]. The expression of the complete Hamiltonian representing our double dot stands as:

$$H_d = \sum_{i \in d,\sigma} (\varepsilon_d + i \times \Delta\varepsilon_d) n_{i\sigma} + U_d n_d (n_d - 1)/2 \tag{A.1}$$

Representing the Hamiltonian of the small dot isolated from the environment. ε_d corresponds to the energy of the first orbital in the dot and serves as an energy reference. $\Delta\varepsilon_d$ and $n_{i\sigma}$ stand for the level spacing and the number of electrons in orbital i with spin σ respectively. ε_d is a free parameter that will enable to vary the energy of dot d, in other words it will simulate the effect of the plunger gate in our experiments. However the transposition from ε_d to V_{gd} is not direct as one can notice in section 4.1, chapter 2. The first term, where the sum is performed over index i represents the orbital contribution. The second term corresponds to the on site Coulomb repulsion where U_d is the charging energy of the small dot d.

$$H_D = \sum_{i \in D,\sigma} (\varepsilon_D + i \times \Delta\varepsilon_D) n_{i\sigma} + U_D n_D (n_D - 1)/2 \tag{A.2}$$

Representing the Hamiltonian of the large isolated from the environment.

$$H_{dD} = U_{dD} n_d n_D + t_{dD} \sum_{\sigma i \in d, j \in D} \left[d^{\dagger}_{i\sigma} d_{j\sigma} + H.c. \right] \tag{A.3}$$

Representing the interaction term between the dots. The first contribution comes from the mutual Coulomb repulsion proportional to U_{dD}. The second term describes the hybridisation of the wave function of each dot. t_{dD} is the intra dot tunnel coupling. The operators $d^{\dagger}_{i\sigma}$ and $d_{j\sigma}$ are the creation and

annihilation operators that create a particle in orbital i of dot d with spin σ and destroys one in orbital j of dot D with the same spin σ, and vice versa (Hermitian conjugate). Transitions at all energies are obtained by summing over different orbitals i and j of dot d and D respectively and over the spin degree of freedom σ.

$$H_V = \sum_{\alpha=L,R} V_\alpha \sum_{(i\in d),k,\sigma} \left[c^\dagger_{\alpha k\sigma} d_{i,\sigma} + H.c. \right] \tag{A.4}$$

Representing the hybridisation of the small dot d and the leads (T shape geometry). V_α is the tunnel coupling leads-dot where alpha identifies left or right lead. Note that an asymmetry left right can be taken into account. Here a given orbital i is assumed to connect identically to the leads. $c^\dagger_{\alpha k\sigma}$ and $d_{i,\sigma}$ create a particle in the lead α with wave vector k and spin σ and destroys a particle in orbital i of dot d with the same spin σ and vice versa (Hermitian conjugate). Transitions at all energies are obtained by summing over α, k, σ and i.

$$H_{\text{band}} = \sum_{\alpha,k,\sigma} \epsilon_k n_{\alpha k\sigma} \tag{A.5}$$

Represents the kinetic energy of the quasi particles in the metallic leads labelled by the index α. ϵ_k is the energy of a state with wave vector k. $n_{\alpha k\sigma}$ is the number of particles in state k with spin σ. The total energy is given by summing over α, k and σ.

Appendix B

Singlet binding energy

We consider a continuum of energy states (large dot) interacting with a single energy level with on-site Coulomb repulsion (small dot). Following [81] we can show that the expression of the exchange interaction with correction to second order stands as:

$$\begin{aligned} J + \delta J &= J + J^2 \rho \ log \frac{D}{T} \\ J &= J \left(1 + J\rho \ log \frac{D}{T} \right) \end{aligned} \tag{B.1}$$

where J is the exchange interaction (Schrieffer-Wolff), δJ is the correction term, ρ is the density of states of the continuum, D is the relevant energy bandwidth of the problem and T is the temperature.
The definition of the Kondo temperature is given when the correction δJ in B.1 is no more a perturbation, that is to say when:

$$J\rho \ log \frac{D}{T} \simeq 1 \tag{B.2}$$

which leads to,

$$T_K \simeq D\sqrt{\rho J} \exp \left(- \frac{1}{\rho J} \right) \tag{B.3}$$

However when the density of states ρ of the continuum reduces to a single energy state, $\rho = \frac{1}{2D}$, then the correction δJ takes the form:

$$\delta J = \rho J^2 D \frac{1}{T} \tag{B.4}$$

which leads to,

$$\begin{aligned} \delta J &= \frac{J^2}{2T} \\ J &= \delta J(T_K) \\ T_K &= \frac{J}{2} \end{aligned} \tag{B.5}$$

The complete calculation giving the binding energy of the singlet from the case of a single energy level to a continuum of energy levels in the reservoir (large dot) is currently under progress.

Bibliography

[1] J. Bardeen and W. H. Brattain. The transistor, a semi-conductor triode. *Phys. Rev.*, 74(2):230–231, Jul 1948. doi:10.1103/PhysRev.74.230.

[2] W. Shockley and G. L. Pearson. Modulation of conductance of thin films of semi-conductors by surface charges. *Phys. Rev.*, 74(2):232–233, Jul 1948. doi:10.1103/PhysRev.74.232.

[3] M. M. Atalla, E. Tannenbaum, and E. J. Scheibner. Stabilization of silicon surfaces by thermally grown oxides. *Bell System Tech. J.*, 38(749), 1959.

[4] D. Kahng. Electric field controlled semiconductor device. (3102230), Aug 1963. `http://www.freepatentsonline.com/3102230.html`.

[5] R. Hanson, L. P. Kouwenhoven, J. R. Petta, S. Tarucha, and L. M. K. Vandersypen. Spins in few-electron quantum dots. *Rev. Mod. Phys.*, 79(4):1217–1265, Oct 2007.

[6] D. Goldhaber-Gordon, Hadas Shtrikman, D. Mahalu, David Abusch-Magder, U. Meirav, and M. A. Kastner. Kondo effect in a single-electron transistor. *Nature*.

[7] A. Hübel, K. Held, J. Weis, and K. v. Klitzing. Correlated electron tunneling through two separate quantum dot systems with strong capacitive interdot coupling. *Phys. Rev. Lett.*, 101(18):186804, Oct 2008.

[8] Potok R.M., I.G. Rau, H. Shtrikman, Y. Oreg, and D. D. Goldhaber-Gordon. Observation of the two-channel kondo effect.

[9] P. S. Cornaglia and D. R. Grempel. Strongly correlated regimes in a double quantum dot device. *Phys. Rev. B*, 71(7):075305, Feb 2005.

[10] Pascal Simon, Julien Salomez, and Denis Feinberg. Transport spectroscopy of a kondo quantum dot coupled to a finite size grain. *Phys. Rev. B*, 73(20):205325, May 2006.

[11] Ribhu K. Kaul, Gergely Zaránd, Shailesh Chandrasekharan, Denis Ullmo, and Harold U. Baranger. Spectroscopy of the kondo problem in a box. *Phys. Rev. Lett.*, 96(17):176802, May 2006.

[12] Lehrstuhlfür Angewandte Festkörperphysik, Ruhr-Universität, Universitätsstraβe 150, 44780 Bochum, Germany. `http://www.ruhr-uni-bochum.de/afp/index.php?main=mitarbeiter&lang=de`.

[13] M. Pioro-Ladrière, John H. Davies, A. R. Long, A. S. Sachrajda, Louis Gaudreau, P. Zawadzki, J. Lapointe, J. Gupta, Z. Wasilewski, and S. Studenikin. Origin of switching noise in GaAs/$\mathrm{Al}_x\mathrm{Ga}_{1-x}\mathrm{As}$ lateral gated devices. *Phys. Rev. B*, 72(11):115331, Sep 2005. doi:10.1103/PhysRevB.72.115331.

[14] Christo Buizert, Frank H. L. Koppens, Michel Pioro-Ladrière, Hans-Peter Tranitz, Ivo T. Vink, Seigo Tarucha, Werner Wegscheider, and Lieven M. K. Vandersypen. *insitu* reduction of charge noise in GaAs/$\mathrm{A}l_x\mathrm{Ga}_{1-x}\mathrm{As}$ schottky-gated devices. *Phys. Rev. Lett.*, 101(22):226603, Nov 2008. doi:10.1103/PhysRevLett.101.226603.

[15] Laboratoire de Photonique et Nanostructures, CNRS, route de Nozay, 91460 Marcoussis, France. `http://www.lpn.cnrs.fr/fr/Commun/`.

[16] P. Rai-Choudhury, editor. *Microlithography, Micromachining and Microfabrication.* SPIE Press, Bellingham - Washington, 1997, 1997.

[17] A. G. Baca, F. Ren, J. C. Zolper, R. D. Briggs, and S. J. Pearton. A survey of ohmic contacts to III-V compound semiconductors. *Thin Solid Films*, 308-309, 1997.

[18] J. M. Elzerman, R. Hanson, J. S. Greidanus, L. H. Willems van Beveren, S. De Franceschi, L. M. K. Vandersypen, S. Tarucha, and L. P. Kouwenhoven. Few-electron quantum dot circuit with integrated charge read out. *Phys. Rev. B*, 67(16):161308, Apr 2003. doi:10.1103/PhysRevB.67.161308.

[19] Eran Lebanon, Avraham Schiller, and Frithjof B. Anders. Enhancement of the two-channel kondo effect in single-electron boxes. *Phys. Rev. B*, 68(15):155301, Oct 2003.

[20] K. Le Hur, P. Simon, and D. Loss. Transport through a quantum dot with su(4) kondo entanglement. *Phys. Rev. B*, 75(3):035332, Jan 2007.

[21] Y. Niimi, Y. Baines, T. Capron, D. Mailly, F.-Y. Lo, A. D. Wieck, T. Meunier, L. Saminadayar, and C. Bäuerle. Effect of disorder on the quantum coherence in mesoscopic wires. *Phys. Rev. Lett.*, 102(22):226801, Jun 2009. doi:10.1103/PhysRevLett.102.226801.

[22] R. Landauer. Electrical resistance of disordered one-dimensional lattices. *Philosophical Magazine*, 21(172):863–867, Apr. 1970.

[23] M. Büttiker. Four-terminal phase-coherent conductance. *Phys. Rev. Lett.*, 57(14):1761–1764, Oct 1986. doi:10.1103/PhysRevLett.57.1761.

[24] B. J. van Wees, H. van Houten, C. W. J. Beenakker, J. G. Williamson, L. P. Kouwenhoven, D. van der Marel, and C. T. Foxon. Quantized conductance of point contacts in a two-dimensional electron gas. *Phys. Rev. Lett.*, 60(9):848–850, Feb 1988. doi:10.1103/PhysRevLett.60.848.

[25] D A Wharam, T J Thornton, R Newbury, M Pepper, H Ahmed, J E F Frost, D G Hasko, D C Peacock, D A Ritchie, and G A C Jones. One-dimensional transport and the quantisation of the ballistic resistance. *Journal of Physics C: Solid State Physics*, 21(8):L209, 1988.

[26] L.I. Glazman, G.B. Lesovik, D.E. Khmelnitskii, and R.I. Shekhter. Reflectionless quantum transport and fundamental ballistic-resistance steps in microscopic constrictions. *JETP Letters*, 48:238, 1988.

[27] A. Yacoby and Y. Imry. Quantization of the conductance of ballistic point contacts beyond the adiabatic approximation. *Phys. Rev. B*, 41(8):5341–5350, Mar 1990.

[28] Yoshiro Hirayama, Tadashi Saku, and Yoshiji Horikoshi. Effect of structure on transport characteristics of ballistic one-dimensional channel. *Japanese Journal of Applied Physics*, 28(Part 2, No. 4):L701–L703, 1989.

[29] L. Landau and E. M. Lifshitz, editors. *Quantum Mechanics: Nonrelativistic Theory*. Pergamon Press., 1977.

[30] L.P. Kouwenhoven. Few-electron quantum dots.

[31] K. K. Likharev. Correlated discrete transfer of single electrons in ultrasmall tunnel junctions. *IBM Journal of Research and Development*, 32:144–158, Jan. 1988. doi:10.1147/rd.321.0144.

[32] C. W. J. Beenakker. Theory of coulomb-blockade oscillations in the conductance of a quantum dot. *Phys. Rev. B*, 44(4):1646–1656, Jul 1991. doi:10.1103/PhysRevB.44.1646.

[33] G. J. Iafrate, K. Hess, J. B. Krieger, and M. Macucci. Capacitive nature of atomic-sized structures. *Phys. Rev. B*, 52(15):10737–10739, Oct 1995. doi:10.1103/PhysRevB.52.10737.

[34] L. S. Kuzmin, P. Delsing, T. Claeson, and K. K. Likharev. Single-electron charging effects in one-dimensional arrays of ultrasmall

tunnel junctions. *Phys. Rev. Lett.*, 62(21):2539–2542, May 1989. doi:10.1103/PhysRevLett.62.2539.

[35] B. L. Altshuler, P. A. Lee, and R. A. Webb, editors. *Mesoscopic phenomena in Solids*. North Holland, 1991.

[36] U. Meirav, M. A. Kastner, and S. J. Wind. Single-electron charging and periodic conductance resonances in gaas nanostructures. *Phys. Rev. Lett.*, 65(6):771–774, Aug 1990. doi:10.1103/PhysRevLett.65.771.

[37] H. Grabert and M.H. Devoret, editors. *Single Charge Tunneling*. Plenum Press, New York, 1991.

[38] I. H. Chan, R. M. Clarke, C. M. Marcus, K. Campman, and A. C. Gossard. Ballistic conductance fluctuations in shape space. *Phys. Rev. Lett.*, 74(19):3876–3879, May 1995.

[39] A.K. Ghosh, editor. *Introduction to Measurements and Instrumentation*. Prentice-Hall of India Pvt.Ltd, 2007.

[40] E. B. Foxman, P. L. McEuen, U. Meirav, Ned S. Wingreen, Yigal Meir, Paul A. Belk, N. R. Belk, M. A. Kastner, and S. J. Wind. Effects of quantum levels on transport through a coulomb island. *Phys. Rev. B*, 47(15):10020–10023, Apr 1993. doi:10.1103/PhysRevB.47.10020.

[41] H. Pothier, P. Lafarge, C. Urbina, D. Esteve, and M. Devoret. Single-electron pump based on charging effects. *Europhys. Lett.*, 17(3):249, Jan 1992. doi:10.1209/0295-5075/17/3/011.

[42] C. Livermore, D.S. Duncan, R.M. Westervelt, K.D. Maranowski, and A.C. Gossard. Measuring interactions between coupled quantum dots in the quantum hall regime. *J. Appl. Phys.*, 86:4043, 1999.

[43] W. G. van der Wiel, S. De Franceschi, J. M. Elzerman, T. Fujisawa, S. Tarucha, and L. P. Kouwenhoven. Electron transport through double quantum dots. *Rev. Mod. Phys.*, 75(1):1–22, Dec 2002. doi:10.1103/RevModPhys.75.1.

[44] I.H. Chan, R.M. Westervelt, K.D. Maranowski, and A.C. Gossard. Strongly capacitively coupled quantum dots. *Applied Physics Letters*, 80:1818, March 2002.

[45] C. Cohen-Tannoudji, editor. *Mécanique Quantique*. Hermann, 1997.

[46] L.I. Glazman and K.A. Matveev. Residual quantum conductivity under coulomb-blockade conditions. *JETP Letters*, 51:484, 1990.

[47] D. V. Averin and Yu. V. Nazarov. Virtual electron diffusion during quantum tunneling of the electric charge. *Phys. Rev. Lett.*, 65(19):2446–2449, Nov 1990. doi:10.1103/PhysRevLett.65.2446.

[48] Y. Funabashi, K Ohtsubo, M Eto, and K. Kawamura. Phase relaxation and non-equilibrium transport properties through multilevel quantum dot. *Jpn. J. Appl. Phys.*, 38:388, Sept. 1998. doi:10.1143/JJAP.38.388.

[49] S. De Franceschi, S. Sasaki, J. M. Elzerman, W. G. van der Wiel, S. Tarucha, and L. P. Kouwenhoven. Electron cotunneling in a semiconductor quantum dot. *Phys. Rev. Lett.*, 86(5):878–881, Jan 2001. doi:10.1103/PhysRevLett.86.878.

[50] R. Schleser, T. Ihn, E. Ruh, K. Ensslin, M. Tews, D. Pfannkuche, D. C. Driscoll, and A. C. Gossard. Cotunneling-mediated transport through excited states in the coulomb-blockade regime. *Phys. Rev. Lett.*, 94(20):206805, May 2005. doi:10.1103/PhysRevLett.94.206805.

[51] J. Kondo. Resistance minimum in dilute magnetic alloys. *Prog. Theor. Phys.*, 32:37 – 49, 1964.

[52] Kenneth G. Wilson. The renormalization group: Critical phenomena and the kondo problem. *Rev. Mod. Phys.*, 47(4):773–840, Oct 1975. doi:10.1103/RevModPhys.47.773.

[53] H. R. Krishna-murthy, K. G. Wilson, and J. W. Wilkins. Temperature-dependent susceptibility of the symmetric anderson model: Connection to the kondo model. *Phys. Rev. Lett.*, 35(16):1101–1104, Oct 1975. doi:10.1103/PhysRevLett.35.1101.

[54] P. W. Anderson. Localized magnetic states in metals. *Phys. Rev.*, 124(1):41–53, Oct 1961. doi:10.1103/PhysRev.124.41.

[55] L.I. Glazman and M.E. Raikh. Resonant kondo transparency of a barrier with quasilocal impurity states. *JETP Lett.*, 47:452, 1988.

[56] Tai Kai Ng and Patrick A. Lee. On-site coulomb repulsion and resonant tunneling. *Phys. Rev. Lett.*, 61(15):1768–1771, Oct 1988. doi:10.1103/PhysRevLett.61.1768.

[57] J. R. Schrieffer and P. A. Wolff. Relation between the anderson and kondo hamiltonians. *Phys. Rev.*, 149(2):491–492, Sep 1966. doi:10.1103/PhysRev.149.491.

[58] P.W. Anderson. A poor man's derivation of scaling laws for the kondo problem. *J. Phys. C: Solid State Phys.*, 3(12):2436, 1970.

[59] A.C. Hewson, editor. *The Kondo Problem to Heavy Fermions.* Cambridge University Press, 1997.

[60] F. D. M. Haldane. Scaling theory of the asymmetric anderson model. *Phys. Rev. Lett.*, 40(6):416–419, Feb 1978. doi:10.1103/PhysRevLett.40.416.

[61] P. Nozières. Magnetic impurities in metals: Kondo effect. *J. Low Temp. Phys.*, 17:31, 1974.

[62] L.I. Glazman and M. Pustilnik. Low-temperature transport through a quantum dot. *arxiv: cond-mat*, Oct. 2005. `http://arxiv.org/abs/cond-mat/0501007v2`.

[63] F. Mallet, J. Ericsson, D. Mailly, S. Ünlübayir, D. Reuter, A. Melnikov, A. D. Wieck, T. Micklitz, A. Rosch, T. A. Costi, L. Saminadayar, and C. Bäuerle. Scaling of the low-temperature dephasing rate in kondo systems. *Phys. Rev. Lett.*, 97(22):226804, Nov 2006. doi:10.1103/PhysRevLett.97.226804.

[64] T.A. Costi, A.C. Hewson, and V. Zlatic. Transport coefficients of the anderson model via the numerical renormalization group. *J. Phys. Condens. Matter*, 6:2519, 1994.

[65] W. G. van der Wiel, S. 1 De Franceschi, T. Fujisawa, J. M. Elzerman, S. Tarucha, and L. P. Kouwenhoven. The kondo effect in the unitary limit. *Science*, 289(5487):2105 – 2108, Sept. 2000. doi:10.1126/science.289.5487.2105.

[66] H. London, G. R. Clarke, and Eric Mendoza. Osmotic pressure of he^3 in liquid he^4, with proposals for a refrigerator to work below 1°k. *Phys. Rev.*, 128(5):1992–2005, Dec 1962. doi:10.1103/PhysRev.128.1992.

[67] O.V. Lounasmaa, editor. *Experimental Principles and Methods Below 1K*. Academic Press Inc, 1974.

[68] A.B. Zorin. The thermocoax cable as the microwave frequency filter for single electron circuits. *Rev. Sci. Instrum.*, 66:4296, 1995. doi:10.1063/1.1145385.

[69] P. Horowitz, editor. *The art of electronics*. Cambridge, 1989.

[70] B.L. Altshuler, A.G. Aronov, and D.E. Khmelnitsky. Effects of electron-electron collisions with small energy transfers on quantum localisation. *J. Phys. C: Solid State Phys.*, 15(36):7367, Dec. 1982.

[71] B. Huard, H. Pothier, D. Esteve, and K. E. Nagaev. Electron heating in metallic resistors at sub-kelvin temperature. *Phys. Rev. B*, 76(16):165426, Oct 2007.

[72] Institut Néel, CNRS, 25 rue des Martyrs, Grenoble, France. `http://neel.cnrs.fr/`.

[73] Yigal Meir and Ned S. Wingreen. Landauer formula for the current through an interacting electron region. *Phys. Rev. Lett.*, 68(16):2512–2515, Apr 1992.

[74] Centro Atómico Bariloche, Av. Bustillo 9.500, 8400 S. C. de Bariloche, Río Negro, Argentina. `http://www.cab.cnea.gov.ar/`.

[75] H. Bruus, editor. *Many-body Quantum Theory In Condensed Matter Physics: An Introduction*. Oxford University Press, 2004.

[76] D. Goldhaber-Gordon, J. Göres, M. A. Kastner, Hadas Shtrikman, D. Mahalu, and U. Meirav. From the kondo regime to the mixed-valence regime in a single-electron transistor. *Phys. Rev. Lett.*, 81(23):5225–5228, Dec 1998.

[77] J. Nygård, D.H. Cobden, and P.E. Lindelof. Kondo physics in carbon nanotubes. *Nature*, 408:342–346, Nov. 2000.

[78] J. Jarillo-Herrero, P. Kong, Herre S.J. van der Zant, C. Dekker, L.P. Kouwenhoven, and S. De Franceschi. Orbital kondo effect in carbon nanotubes. *Nature*, 434:484–488, March 2005.

[79] J. V. Holm, H. I. Jørgensen, K. Grove-Rasmussen, J. Paaske, K. Flensberg, and P. E. Lindelof. Gate-dependent tunneling-induced level shifts observed in carbon nanotube quantum dots. *Phys. Rev. B*, 77(16):161406, Apr 2008.

[80] A. Ramšak, J. Mravlje, R. Žitko, and J. Bonča. Spin qubits in double quantum dots: Entanglement versus the kondo effect. *Phys. Rev. B*, 74(24):241305, Dec 2006.

[81] F. Mancini, editor. *Lectures on the Physics of Highly Correlated Electron Systems VI*. American Institute of Physics, 2002.

[82] B. Coqblin and J. R. Schrieffer. Exchange interaction in alloys with cerium impurities. *Phys. Rev.*, 185(2):847–853, Sep 1969.